Modeling, Characterizing and Reconstructing Mesoscale Microstructural Evolution in Particulate Processing and Solid-State Sintering

by

Shaohua Chen

A Dissertation Presented in Partial Fulfillment
of the Requirements for the Degree
Doctor of Philosophy

Approved April 2018 by the
Graduate Supervisory Committee:

Yang Jiao, Chair
Qinghua Wang
Heather Emady
Aytekin Gel

ARIZONA STATE UNIVERSITY

May 2018

©2018 Shaohua Chen

All Rights Reserved

ABSTRACT

In material science, microstructure plays a key role in determining properties, which further determine utility of the material. However, effectively measuring microstructure evolution in real time remains an challenge. To date, a wide range of advanced experimental techniques have been developed and applied to characterize material microstructure and structural evolution on different length and time scales. Most of these methods can only resolve 2D structural features within a narrow range of length scale and for a single or a series of snapshots. The currently available 3D microstructure characterization techniques are usually destructive and require slicing and polishing the samples each time a picture is taken. Simulation methods, on the other hand, are cheap, sample-free and versatile without the special necessity of taking care of the physical limitations, such as extreme temperature or pressure, which are prominent issues for experimental methods. Yet the majority of simulation methods are limited to specific circumstances, for example, first principle computation can only handle several thousands of atoms, molecular dynamics can only efficiently simulate a few seconds of evolution of a system with several millions particles, and finite element method can only be used in continuous medium, etc. Such limitations make these individual methods far from satisfaction to simulate macroscopic processes that a material sample undergoes up to experimental level accuracy. Therefore, it is highly desirable to develop a framework that integrate different simulation schemes from various scales to model complicated microstructure evolution and corresponding properties. Guided by such an objective, we have made our efforts towards incorporating a collection of simulation methods, including finite element method (FEM), cellular automata (CA), kinetic Monte Carlo (kMC), stochastic reconstruction method, Discrete Element Method (DEM), etc, to generate an integrated computational material engineering

platform (ICMEP), which could enable us to effectively model microstructure evolution and use the simulated microstructure to do subsequent performance analysis. In this thesis, we will introduce some cases of building coupled modeling schemes and present the preliminary results in solid-state sintering. For example, we use coupled DEM and kinetic Monte Carlo method to simulate solid state sintering, and use coupled FEM and cellular automata method to model microstrucutre evolution during selective laser sintering of titanium alloy. Current results indicate that joining models from different length and time scales is fruitful in terms of understanding and describing microstructure evolution of a macroscopic physical process from various perspectives.

DEDICATION

To Past Ages

ACKNOWLEDGMENTS

I would like to thank my committee chair, Dr Yang Jiao, for his inspiring guidance and constant support throughout my five year PhD program, without whom, this work won't be possible. I would also like to express my gratitude to my committe co-chair Dr Aytekin Gel, for his support and encouragement from my research to personal development, and to all my committee members, Dr Heather Emady and Dr Qinghua Wang, for their willingness to be on my committee.

Last but not least, I am grateful for the help from my group mates, and for the joyful time we have spent together in the past five years.

TABLE OF CONTENTS

CHAPTER Page

LIST OF TABLES

LIST OF FIGURES

Figure Page

Chapter 1

INTRODUCTION

Nowadays, materials researchers are largely focused on studying physical processing, microstructure characterization, property prediction, and performance evaluation, as well as their mutual relations, as demonstrated in Fig.1. Among them, microstructure characterization is a key component in terms of understanding why different materials have distinctive properties. Both in research and manufacturing, it has been realized that obtaining non-destructive microstructure and dynamical microstructure evolution via experimental techniques up to satisfactory accuracy is still a challenging subject, which is the primary reason for the efforts towards inventing other possible approaches. Computational methods, especially in modern era of increasingly powerful computing platforms, are very promising alternatives to assist scientists and engineers to achieve better understandings of the relation among processing, microstructure evolution and various material properties. Although it has been extensively explored, current progress of individual computational modeling technique is still way below the expectation of industrial utilization. The limitation of individual modeling scheme is obvious: the more accuracy it achieves, the more difficult it is to deal with large system; on the other hand, the larger the system it can handle, the less accurate the result will be. The accuracy and computational efficiency seem to be a contradictory pair for single simulation method.

One of the promising solutions lies in creating coupled multi-scale combinative model which incorporates various modeling methods originally meant for specialized purpose at unique time and length scales. For instance, to study the effect of phase

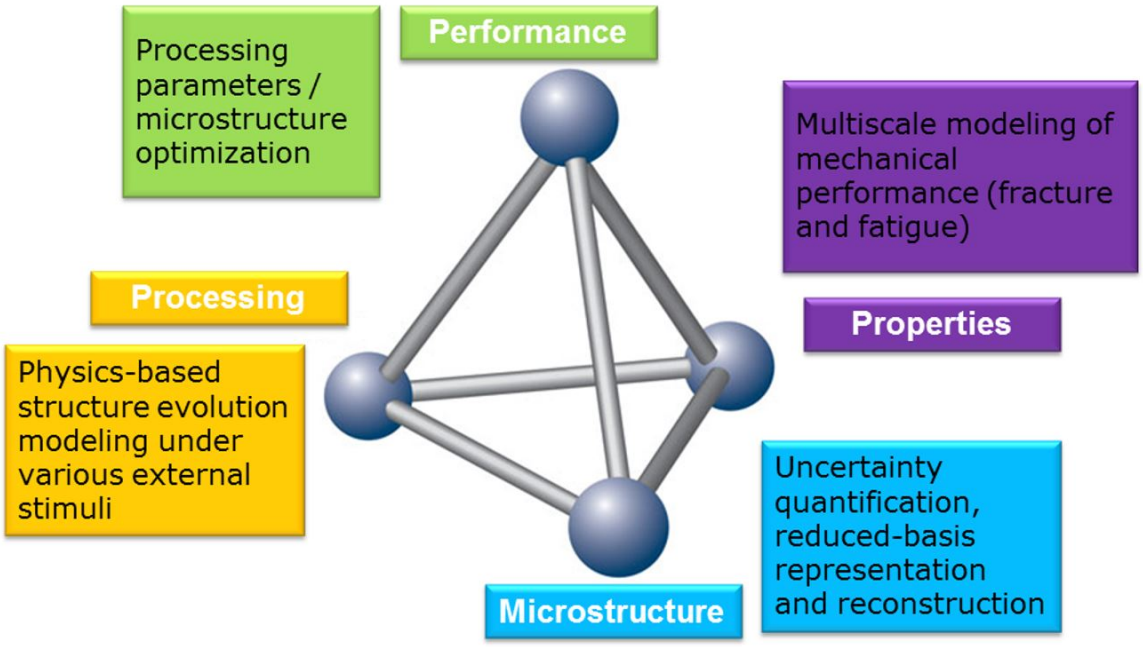

Figure 1: Relation among processing, microstructure, property and performance in materials research

transition on mechanical properties, *ab inito* computation can be used to calculate the electronic structure and basic physical properties; molecular dynamics can be used to simulate the collective and emergent behavior of a group of molecules and related thermodynamic properties; phase field and cellular automata are generally used to simulate the nucleation and growth of grains; finite element analysis or discrete element method can be applied to determine the macro properties, such as fatigue life and cracking resistance. Understandably, the time and length scale as well as modeling assumptions that each simulation method is invented upon might be significantly different, which requires elaborate interfacing algorithms and the quantification of modeling uncertainty propagation to combine multiple simulation methods and make them function as a whole. This thesis presents our effort towards establishing such type of combinative simulation schemes for some widely applied manufacturing processes,

and some preliminary results are also demonstrated. An illustration of "powder processing - solid state sintering - 3D microstructure reconstruction" combinative simulation procedure is demonstrated in Fig.2.

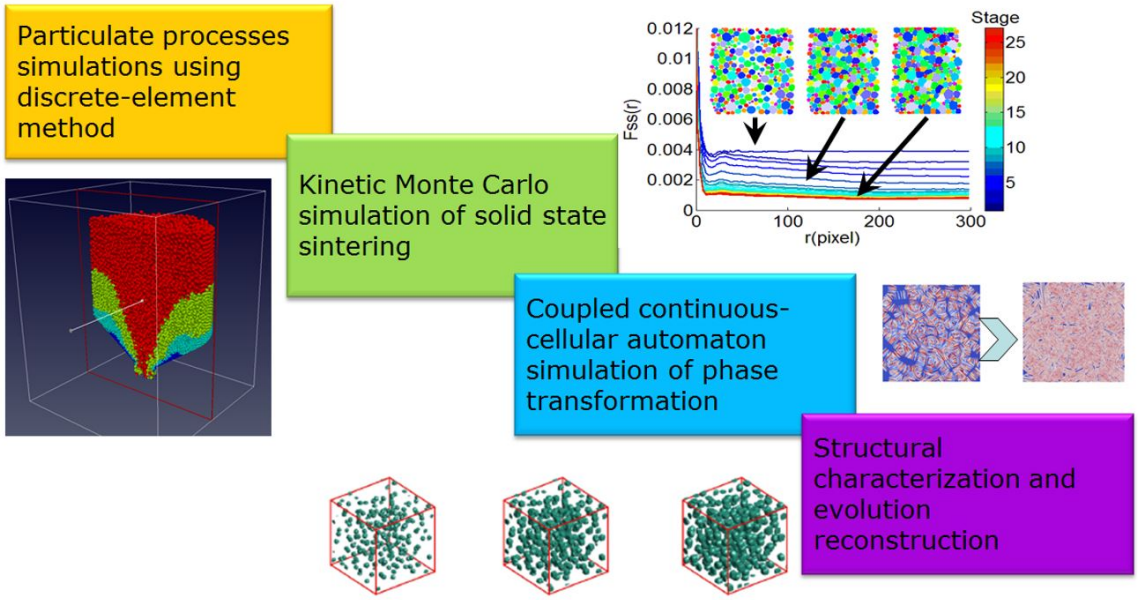

Figure 2: An example of combinative modeling process. It starts with DEM simulation of powder packing; then, randomly cut a 2D slice of the initial 3D packing configuration and do a kinetic Monte Carlo or cellular automata simulation to model microstructure evolution on the slice; finally, a 3D microstructure can be obtained though stochastic reconstruction algorithm.

A range of modern industrial processes start from powder preparation, such as solid state sintering, 3D printing, production of porous filters, etc. Currently, two major modeling methods are popular in the application of powder simulation: continuum method, such as two fluid model (TFM), and discrete element method (DEM). With increasingly booming power of modern computing devices and the extensive exploration of parallel computing, DEM simulation has gained more and more attention due to the intrinsic similarity between discrete element and granular nature of powders, and increasingly accurate characterization of particulate matter with DEM. A discharging

hopper, which is a common chemical engineering technique, will be provided as a demonstration of DEM modeling.

With the packing structure of a powder system, we are able to simulate the powder-based manufacturing processes. However, directly simulating a 3D system is usually time-consuming and computationally demanding. Therefore, the majority of microstructure simulations are performed in 2D. Even though there are cases where a 2D simulation can be representative enough to understand a specific type of microstructure, especially when the system is isotropic and homogeneous, it's still necessary to obtain 3D microstructure representation for other analysis, such as mechanical property calculations, performance evaluations, etc. Past research has shown that, with a 2D image of microstructure and some necessary assumptions, the 3D microstructure can be statistically reconstructed with high efficiency based on the extracted statistical descriptors from the image, such as n-point correlation functions. We will present an instance of stochastic microstructure reconstruction procedure for metallic composite employing two point correlation function and radial distribution function.

With the ability of DEM simulation for powder preparation and 3D microstructure reconstruction from 2D slice, next, we are trying to establish a combinative model to simulate solid-state powder sintering. First, we generate an statistically uniform initial powder configuration as an input for sintering; then we randomly cut a slice from this configuration and use kinetic Monte Carlo method to simulate the microstructure evolution on this 2D structure; finally, we reconstruct the 3D microstructure based on the 2D sinterng structure via aforementioned stochastic reconstruction algorithm. Through the combination of DEM, kinetic Monte Carlo and stochastic reconstruction, it provides a promising approach to numerically investigate the effect of geometry and

size distribution of particle packing on sintered microstructure in an highly efficient way.

In another case of model coupling, we use finite element method (FEM) to simulate the temperature field of the selective laser sintering process of Ti_6Al_4V, which is further treated as external input directing the microstructure evolution of $\beta \rightarrow \alpha$ phase transition at 990 °C, simulated via cellular automata method. This coupled model allows us to investigate the effect of different processing parameters, such as laser power, radius of laser spot and scanning path, etc., on titanium alloy microstructure evolution during laser sintering. The potential application of this model might be the computer-aided alloy product design.

The thesis goes as follows: in chapter 2, the DEM modeling and its application on a discharging hopper containing powders with different size distribution and geometry is introduced using open source software, MFIX, a suite of multi-phase flow simulation models; in chapter 3, the examples of static 3D microstructure reconstruction and dynamic microstructure evolution reconstruction are discussed, utilizing stochastic quantifiers, such as two point correlation function, radial distribution function and surface-surface correlation, etc, which are also briefly overviewed; in chapter 4, a coupled model of DEM and kinetic Monte Carlo method is introduced and applied on a typical solid-state sintering process; in chapter 5, an integrated model of finite element method and cellular automata for selective laser sintering of Ti_6Al_4V is discussed in details; in chapter 6, we present our effort towards inverse reconstruction of elastic modulus field from displacement response of extra cellular matrix featured by interconnected collagen fibers; in chapter 7, we summarize this thesis and make some outlook.

Chapter 2

DEM SIMULATION FOR POWDER PACKING USING MFIX-DEM

2.1 Background

Traditionally, it's a common practice to treat granular media as continuum media and use finite element method to obtain the mechanics. However, as the modern computing system gets more and more sophisticated and efficient, discrete element method (DEM) gains its popularity in handling moderate-size system with particle number of several millions [1]. Compared to continuum method, DEM is superior in capturing complicated nonlinearity and local behavior using nonspherical and polydispersed packings, referring to Fig.3 as an instance. By extending conventional DEM simulation to polydispersed packing and nonspherical particles, it enables us to deal with problems through accurate description of the physics and provides solutions with high fidelity.

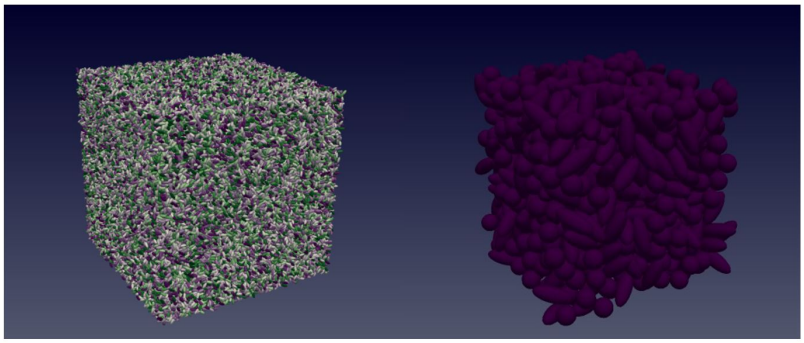

Figure 3: left: packing configuration of mono-sized ellipsoidal granular particle, the colors denote spatial orientations; right: packing configuration of ellipsoid and sphere mixture.

Among those tools that have been developed for DEM simulation, MFIX (*https://mfix.netl.doe.gov*), a suite of multi-phase flow models, provides a unified framework under a single user interface and code base to simulate a diverse range of multiphase flow problems [2]. Hence, MFIX eliminates the need to externally couple separate modeling softwares. Since its initial release, MFIX has been constantly updated and successfully employed to model a variety of multiphase flow problems relevant to industrial and energy-related applications [3, 4, 5, 6, 7].

In spite of its versatility, the lack of computationally efficient methods to simulate polydispersed systems has posed some problems when modeling industrial applications. Accurately capturing the particle size distribution is crucial to processes involving denser granular flows and jammed granular packings[8, 9]. More importantly, the capability to handle polydispersed systems easily is often available in other open-source and commercial DEM software (e.g., LIGGGHTS [10] and EDEM [11]). Therefore, we make our contribution to enhance MFIX-DEM's physical modeling capability for handling particle-size polydispersity for the pure DEM model. Specifically, we have modified the data structure and created new subroutines to separately handle geometrical and physical parameters of the solid phase particles. This approach enables MFIX-DEM to handle an arbitrary number of solid phases, each possessing a distinct arbitrary particle-size distribution. New input keywords have been introduced to allow convenient specification of an arbitrary particle-size distribution function, such as normal, log-normal, uniform, and even user defined distributions, which are realized through initial condition or mass-in-flow boundary condition. Our new implementation is systematically validated using hopper bin discharge experiments, a commonly used set-up with many industrially relevant applications. In particular, we use two types of glass beads with distinct size distributions to fill the hopper

in two possible packing arrangements, i.e., well-mixed and layered configurations, with varying mass (particle number) ratios. The experimentally obtained discharge dynamics (e.g., normalized discharge mass fraction for one of the phases vs. the overall discharge mass fraction) for different systems is found to be in excellent agreement with the corresponding simulation results, which clearly validates the newly implemented polydispersity features.

2.2 Implementation of polydispersity

The basic idea of our new implementation is to separately save the particle geometrical parameters (i.e., diameters) which are particle-specific and the physical parameters which are phase-specific. In particular, we modified the array **D_P0** such that it saves the diameter of each particle in the system, thus possessing a size of the total particle number N. For example, **D_P0(i)** now gives the diameter of particle i, instead of the diameter of particles for phase i. Accordingly, the phase index of each particle is not assigned according to its diameter, but assigned based on its physical properties, e.g., material density. Although the new implementation offers just three types of built-in size distribution functions, addition of new distributions can be easily done through the *RANDOMNO_MOD.F* subroutine. For a user-specified distribution, the particle diameter information is provided in a standalone input file and is read in during the initialization stage.

2.3 Verification of polydispersity implementation on MFIX-DEM

We verify the new implementation by simulating particle discharge from a 3D hopper with equal-sized spherical beads. The *2016-1* release version of MFIX is also used to simulate the same system for comparison. The hopper contains a cylinder part of height $5cm$ and diameter $6cm$, connected to a cone part with height $5cm$ and angle of $30°$. The bottom of the hopper cone is further connected to a short cylinder tube of height $0.2cm$ and diameter $0.5cm$. The beads possess a diameter of $0.068cm$, spring constant of $2.5 \times 10^5 g/s^2$, friction coefficient of 0.01 and coefficient of restitution of 0.5.

The initial configuration for the discharge simulation is first obtained by settling the hopper with 15540 beads from the top (through the mass-in-flow boundary condition), while the bottom is kept closed (through the non-slip-wall boundary condition). The resulting packing is allowed to settle to completely dissipate the kinetic energy, and then the resulting stable packing is used as the initial configuration for the discharge simulation until the hopper is fully discharged.

Table 1 summarizes the verification simulation details, including the number of particles, domain decomposition configuration and total CPU hours required for full discharge. Fig.4 shows the discharge dynamics for the monodisperse system, i.e., discharged mass vs. discharge time, obtained using both the original *2016-1* release of MFIX-DEM and our new polydispersed implementation derived from the *2016-1* release. It can be seen that in both cases, the initial discharge rates are relatively small and become stable after 2 seconds after the discharge starts. The discharged mass fractions for the two cases slightly deviate from one another due to uncertainty in the initial settled packing configurations. The overall discharge dynamics agree

very well with one another. In addition, the total CPU hours for the simulations are also comparable for the two cases. These results verify the correctness of our new implementation.

Table 1: Summary of the computing layout used in the verification case.

	Domain Decomposition Configuration	Total Number of Particles	CPU Hours
MFIX-DEM *2016-1*	$2 \times 2 \times 2$	15544	5.45
Polydispersity Implemented	$2 \times 2 \times 2$	15540	5.44

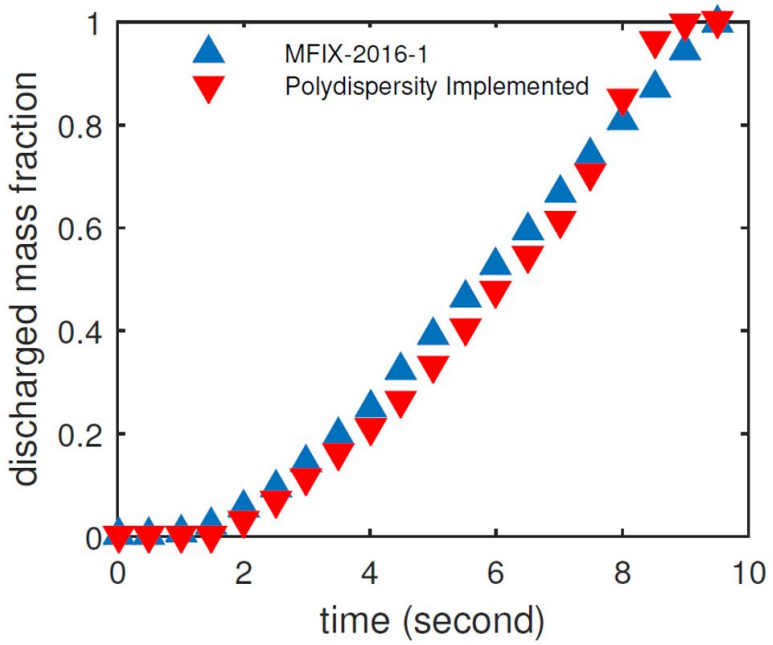

Figure 4: Comparison of discharge dynamics between MFIX *2016-1* release version of polydispersity implemented version.

2.4 Validation of polydispersity implementation

To validate our polydispersity implementation, we carry out hopper discharge experiments. The hopper used in experiments (shown in Fig.5) is 3D printed using a Stratasys Dimension 1200es SST (Stratasys Ltd. MN, USA), with ABSplus thermoplastic. It contains a cylinder part of $12.5cm$ in height and $12.5cm$ in diameter, connected to a cone part with a height of $3.5cm$ and $55°$ cone angle. The bottom of the hopper cone is further connected to a short cylinder tube of height $1.3cm$ and diameter $2.5cm$. The hopper is leveled and clamped to a support stand. A glass slide gate is used to close and open the hopper outlet, to fill and discharge, respectively.

Figure 5: 3D printed hopper used to conduct the experiment for polydispersity implementation validation.

The granular materials used in the experiments are silica beads (soda-lime silica glass). The silica beads are purchased from Potters Industries, PA, USA; with particle density $2.5g/cm^3$ in different sizes. The particles are further sieved to narrow the particle size distribution (PSD). The sieved particles are analyzed using Malvern Morphologi G3SE (Malvern Instruments Ltd, UK), and two distinct sized polydispersed silica beads with a bi-modal size distribution (shown in Fig.6) are used for the experiments. Specifically, the system can be considered to contain two phases of solid particles, each possessing a distinct normal size distribution, with same physical and chemical properties. The fine particles possess a normal distribution with a mean of $1.5mm$ and standard deviation of $0.3mm$, and the coarse particles also possess a normal distribution with a mean of $2.9mm$ and standard deviation of $0.1mm$.

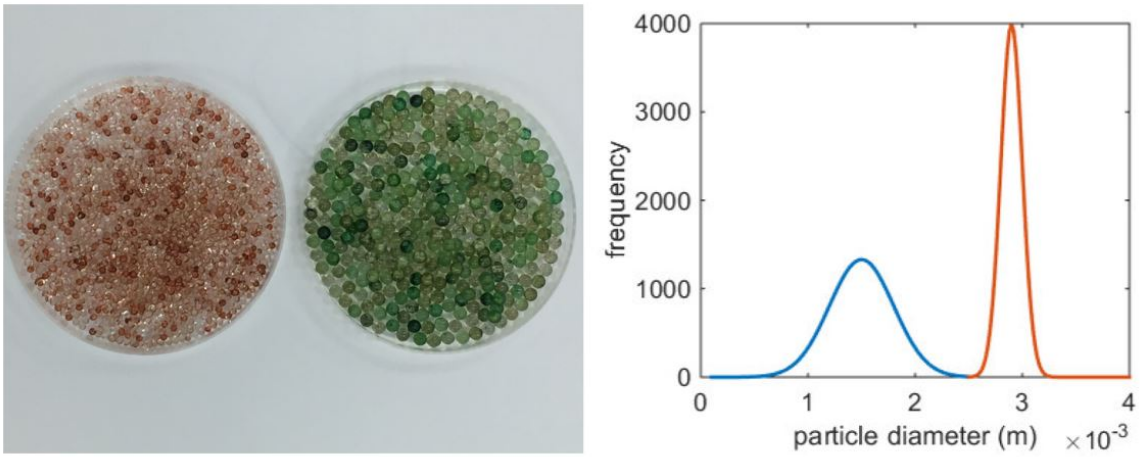

Figure 6: Left: fine (brown) and coarse (green) particles used in experiment; Right: diameter distribution of fine (blue) and coarse (red) particles.

While particles discharge through the hopper, the materials become tribocharged and tend to stick to the walls of the hopper. To remove any charging of the particles during discharge, the particles are rinsed with an anti-static solution. The anti-static solution is prepared by dissolving $1ml$ of ASA antistatic agent (Electrolube, UK) into

$100ml$ of ethanol. The particles are subsequently dried overnight producing particles with a coating of the anti-static solution. No change in the discharge dynamics and segregation is observed before and after the particles are coated with the anti-static solution.

The mass of the fine and coarse particles used in the experiments are $580g$ and $420g$ respectively. Two initial packing configurations are prepared using the fine and coarse particles. In the first configuration, the fine and coarse particles are well mixed. For this, both the fine and coarse particles are divided into 10 equal portions. One portion of fine particles is mixed with one portion of coarse particles using Turbula T2F Shaker-Mixer (Glen Mills Inc., NJ, USA). The same procedure is repeated with remaining 9 portions to produce 10 equal portions of well mixed fine and coarse particles. The hopper outlet is closed, and each portion is loaded into the hopper slowly, to minimize segregation due to free fall. The particle bed is leveled after each portion is loaded. In the second configuration, the coarse particles are first packed at the bottom of the hopper (with the outlet closed) and then the fine particles are loaded on top of the coarse particles to form a layered packing. Each layer is leveled after loading into the hopper. The top view of initial and intermediate stage configurations of both setups are shown in Fig.7. We note that these configurations were also used by Ketterhagen et al., (2007) [12].

The discharge experiment is then carried out using a discontinuous sampling method[13]. The outlet of the hopper is opened, and samples of equal mass are collected using the discontinuous sampling method. The collected samples are sieved and weighed to determine the mass of fine and coarse particles. Then the discharged mass fraction of both the fine and the coarse particles are determined, and the segregation data is plotted as the normalized mass fraction of fines and the fractional mass

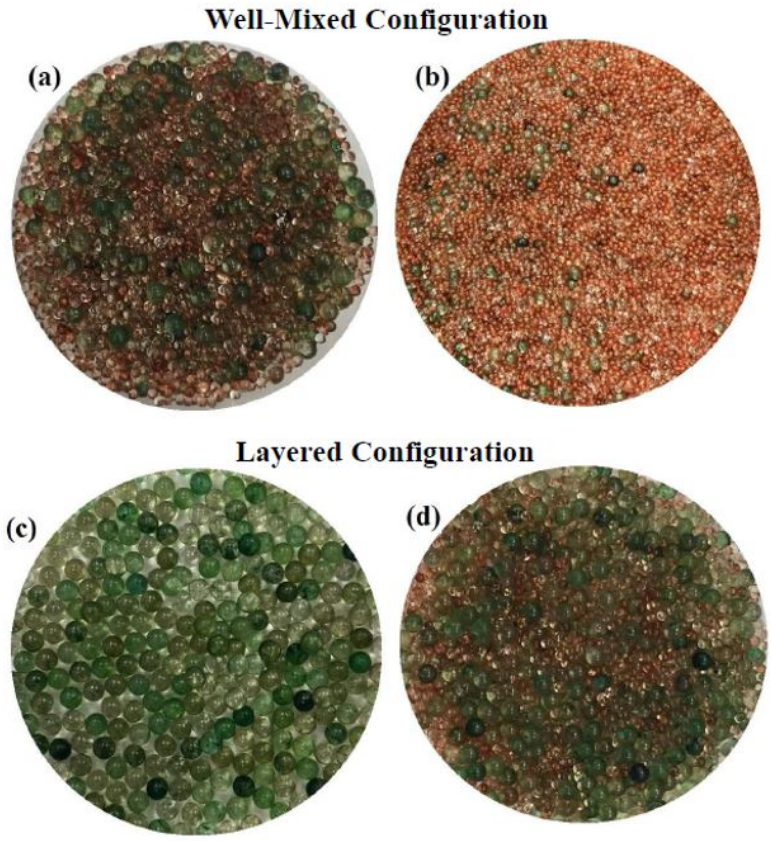

Figure 7: Top views of both experimental setups at the beginning and intermediate time. (a)(b)Initial and intermediate images for well-mixed case. (c)(d)Initial and intermediate images for fine-over-coarse layered case.

discharged. During the experiments with the well-mixed configuration, segregation occurs during loading the hopper with particles. So, each experiment is replicated 5 times to minimize the effects of any non-homogeneous regions on the discharge segregation results, for both the well mixed and the layered configuration. The experimental results are compared with MFIX simulations to validate our polydispersity implementation.

On the MFIX simulation side, we also prepare powder packings in both well-mixed and layered initial configurations, which are identical to the experimental setups described above (i.e., with the same hopper geometry, particle size distributions and

fine to coarse particle ratios). For the simulations, we consider that the glass beads possess a spring constant of $2.5 \times 10^5 g/s^2$, friction coefficient of 0.5 and coefficient of restitution of 0.9, which are consistent with the previous studies [12]. As discussed before, to more efficiently handle size distribution in the simulation, a maximum and minimum value are specified for each size distribution. The fine-to-coarse particle mass ratio is 0.58: 0.42, which corresponds to a fine-to-coarse number ratio of 8: 1. The parameters for the particle phases used in our simulations are summarized in table 2. We note that in our subsequent simulations, the initial packings are generated using the mass-in-flow boundary condition (i.e., the particles are filled into the hopper from the top). In current implementation, the mass-inflow boundary condition does not allow one to precisely control the number of particles for each solid phase to be filled in the hopper. Therefore, the mass ratio is first determined in the hopper discharge simulation and then reproduced in the experiments, in which the mass for each phase can be precisely controlled.

Table 2: Summary of size distribution parameters and quantities of fine and coarse particles.

Sample	Mean Diameter	Max. Diameter	Min. Diameter	Total Mass
Fine	$0.15cm$	$0.17cm$	$0.13cm$	$580g$
Coarse	$0.29cm$	$0.31cm$	$0.27cm$	$420g$

For well-mixed configuration, the initial configuration for the discharge simulation is obtained by filling the hopper with both fine and coarse beads together from the top through the mass-in-flow boundary condition, while keeping the bottom closed with a non-slip-wall boundary. The flow rates of the fine and coarse beads through the top are $16cm/s$, with volume fraction of 0.0145 for coarse beads and 0.0165 for fine beads at the injection boundary. The resulting packing is allowed to settle to

completely dissipate the kinetic energy, and the resulting well-mixed stable packing is used as the initial configuration for the discharge simulation until the hopper is fully discharged.

Fig.8 shows the snapshots of the discharge simulations at several different times. The discharge dynamics are quantified using the normalized fine mass fraction, γ_f^N, of the discharged particles vs. the overall discharged mass fraction, $\bar{\gamma}$. Specifically, $\gamma_f^N = \gamma_f^{discharge}/\gamma_f^0$, where $\gamma_f^{discharge}$ is the fine mass fraction of the discharged particles and $gamma_f^0$ is the fine mass fraction in the initial packing configuration. Also, $\bar{\gamma} = m^{discharge}/m_0$, where $m^{discharge}$ is the total discharged mass and m_0 is the mass of the initial particle packing.

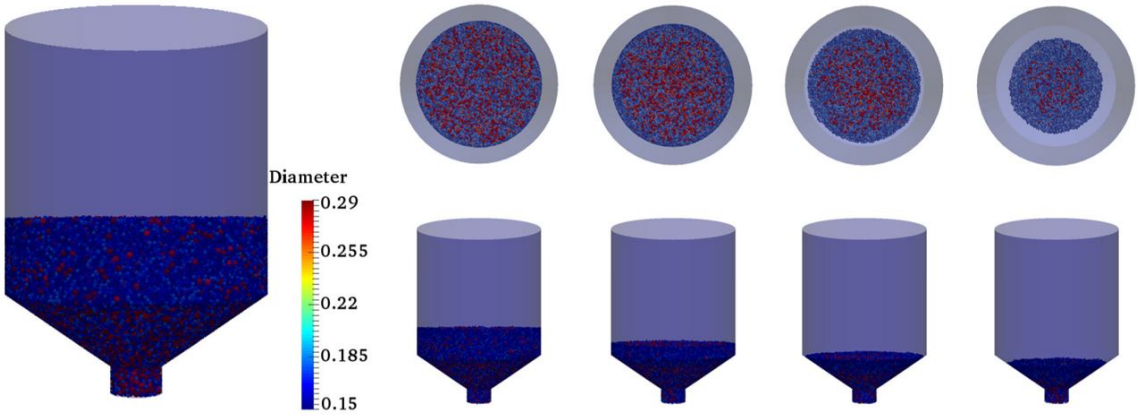

Figure 8: Left: the side view of initial configuration for well-mixed case; Right: the top views (top) captured at time equal $2s$, $6s$, $9s$, $11s$ and the corresponding side views (bottom).

In the ideal case that during the entire discharge process, the packing configuration stays well mixed, the resulting γ_f^N-$\bar{\gamma}$ curve would be a simple step function. However, due to segregation effects, the fine particles cluster at the hopper bottom towards the end of the discharge, leading to an increase of γ_f^N towards the end of discharge (see

Fig.9). The simulated γ_f^N curve agrees very well quantitatively with our experimental data.

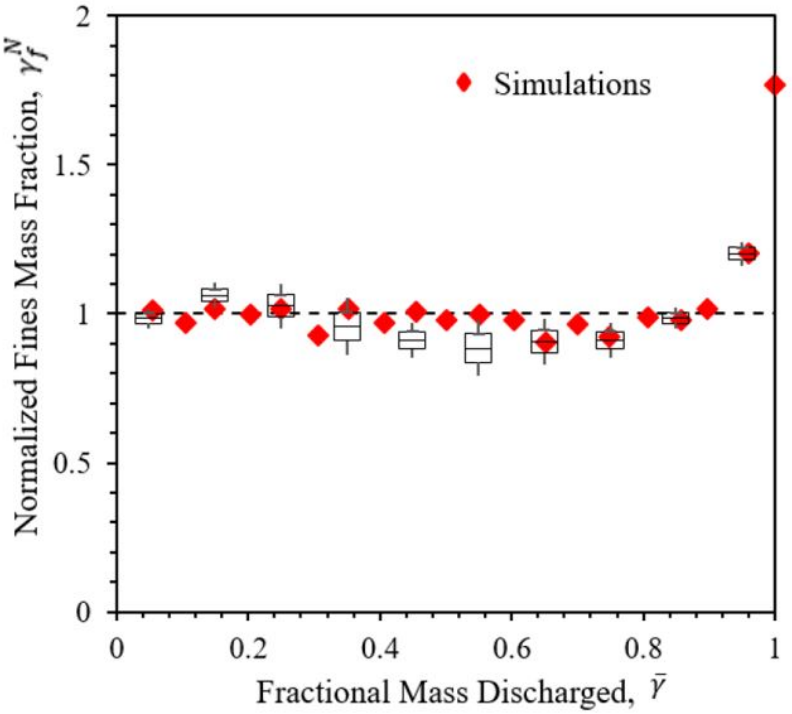

Figure 9: The segregation plot for well-mixed configuration, which is the normalized fine mass fraction at each time step against total fraction mass discharged.

For the layered configuration, the initial configuration for discharge simulation is obtained by first filling the hopper with coarse beads from the top through the mass-in-flow boundary condition, while the bottom is kept closed through the non-slip-wall boundary condition, and then continuing to fill the hopper with fine beads, which settle on top of the coarse beads. The flow rates of the fine and coarse beads through the top are $16cm/s$, with a volume fraction of 0.02 for each layer respectively. The resulting packing is allowed to settle to completely dissipate the kinetic energy, and the resulting layered stable packing is used as the initial start for the discharge simulation until the hopper is fully discharged.

Fig.10 shows the snapshots of the discharge simulations. The discharge segregation as quantified via γ_f^N-$\bar{\gamma}$ is shown in fig. 11. As demonstrated in fig. 10, in this case, the coarse particles packed at the hopper bottom discharge first, which opens up a channel for the fine particles on the top. Therefore, the resulting γ_f^N remains zero for a while (before a channel is opened up), and is monotonically increasing as the discharge proceeds after the channel is open. Towards the end of discharge, since most of the fine particles in the hopper are gone, γ_f^N begins to decrease and finally starts to fluctuate due to very small number of fine particles remaining in the hopper. Again, our simulated γ_f^N-$\bar{\gamma}$ curve agrees very well quantitatively with the experimental data.

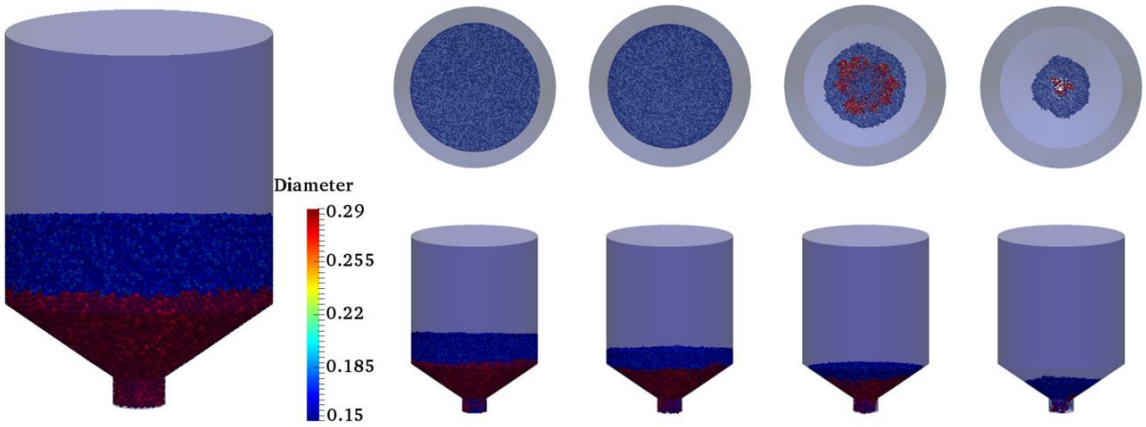

Figure 10: Left: the side view of initial configuration for layered case; Right: the top views (top) captured at time equal $2s$, $6s$, $9s$, $11s$ and the corresponding side views (bottom).

2.5 Conclusion

In summary, we enhanced the capability of MFIX to handle particle-size polydispersity for granular flow simulation via pure DEM mode . We have modified the

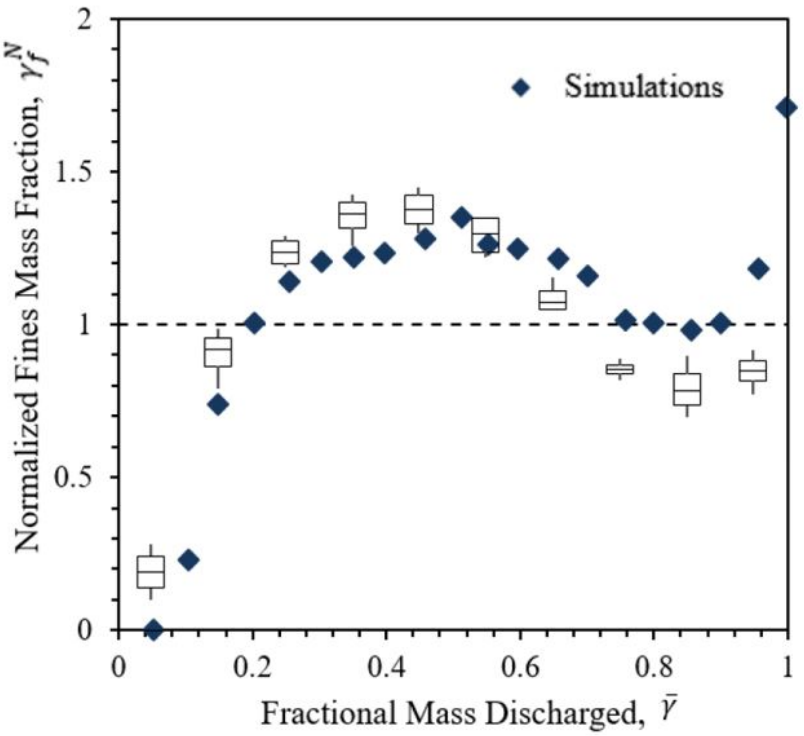

Figure 11: The segregation plot for layered configuration, which is the normalized fine mass fraction at each time step against total fraction mass discharged.

data structure and created new subroutines to separately handle geometrical and physical parameters of the solid phase particles. This allows MFIX-DEM to easily handle an arbitrary number of solid phases, each possessing an arbitrary particle-size distribution. New key words have been introduced to allow easy specification of a variety of built-in and user-defined distributions, for both the initial condition and mass-in-flow boundary condition modules. The new implementation is systematically validated using discharge hopper experiments, a commonly encountered set-up with many industrial applications, with polydispersed particles. The simulated discharge dynamics, including the normalized fine mass fraction vs. the overall discharged mass fraction, are found to be in excellent agreement with the corresponding experimental data, which clearly validate our new implementations.

The current implementation can easily handle particle size dispersity as large as 10:1. To efficiently handle larger dispersity (e.g., $>20:1$), additional modifications of the codes (e.g., by implementing adaptive near-neighbor list [14]) are required to make simulations in an acceptable time frame. Nonetheless, the new polydispersity feature added to MFIX-DEM enables users to better capture the actual particle geometry of the solid phases, and thus, would lead to more accurate simulations of multiphase flows involving particle phases especially in the dense flow regime.

With the ability of efficiently simulating polydispersed particle packing, a powder precursor can be easily obtained for later application of simulating powder based manufacturing processes, such as solid-state sintering. The current implementation will also pave the way for further development, such as feature of the non-spherical particle shape, as the data structures for handling individual particle sizes can be readily generalized to handle other particle geometry parameters. If finished, we will be able to create more realistic powder packing configurations with both polydispersity and nonspherical particles.

The results demonstrated in this chapter are published in Powder Technology 317, 117 (2017).

Chapter 3

STOCHASTIC RECONSTRUCTION OF MICROSTRUCTURE FROM 2D TO 3D

3.1 Background

In previous chapter, we introduced DEM simulation to generate large packing configuration of solid powder. Unfortunately, based on currently available computational techniques, directly performing microstructure evolution for 3D system is quite time-consuming. Nevertheless, an accurate knowledge of the 3D polycrystalline microstructure of a material is crucial to its property prediction, performance optimization and design. If we are able to simulate microstructure evolution in 2D, and then restore to the 3D microstrucutre, it might be a more efficient way to deal with a large system.

Here, we present a computational scheme that allows one to stochastically reconstruct the 3D microstructure of a highly heterogeneous polycrystalline material with large variation in grain size, morphology and spatial distribution, as well as the distribution of second phase particles, from single 2D electron-back-scattered-diffraction (EBSD) micrograph. Specifically, the two-point correlation functions S_2 are employed to statistically characterize grain morphology, orientation and spatial distribution and are incorporated into the simulated annealing procedure for microstructure reconstruction. During the reconstruction, the original polycrystalline microstructure is coarsened such that the large grains are reconstructed first and the smaller ones are generated later. The second phase particles are then inserted into the reconstructed polycrystalline material based on the pair-correlation function g_2 sampled from the

2D backscattered electron (BSE) micrograph. The utility of our multi-scale scheme is demonstrated by successfully reconstructing a highly heterogeneous polycrystalline Sn-rich solder joint with Cu_6Sn_5 intermetallic particles. The accuracy of our reconstruction is ascertained by comparing the virtual microstructure with the actual 3D structure of the joint obtained via serial sectioning techniques.

Advanced experimental techniques such as the electron-back-scattered-diffraction (EBSD) imaging are routinely used to characterize the microstructure of polycrystalline materials. Due to the nature of this technique, only the polished flat surface of the material can be probed, which results in a 2D micrograph showing a "slice" of the grain morphology, orientation, and spatial distribution. Serial sectioning technique[15] has been used in combination with EBSD to obtain 3D polycrystalline structures. Specifically, after the EBSD micrograph of the top surface is obtained, the specimen is polished such that the top layer is removed and a new surface is imaged. This process is continued until a sufficient number of 2D slices of the material are obtained, which are then stacked to generate a 3D reconstruction. Although widely used, this technique is tedious and very time-consuming. Moreover, it destroys the specimen and is thus, not suitable to study time-dependent structure evolution under external stimuli.

Recently, a number of stochastic reconstruction techniques have been developed that allow one to generate "virtual" polycrystalline microstructures from three orthogonal 2D EBSD micrographs associated with the three surfaces of the specimen[16, 17]. Specifically, each 3D grain is modeled as an ellipsoid, whose three principal axes are estimated from the 2D micrographs. A packing of ellipsoids is generated using a Monte Carlo simulation, whose semi-axis statistics satisfy those obtained from the 2D images. The ellipsoids are allowed to grow to fill the entire simulation domain, which

leads to 3D grain structure. Then the grain orientations are assigned based on the corresponding statistics obtained from the 2D micrographs and a 3D polycrystalline microstructure is reconstructed. More recently, a generalized method [18, 19] has been devised that incorporates additional statistics such as orientation correlations directly obtained from 3D EBSD reconstructions. In addition, a new tessellation scheme has been used to better represent grain morphology. These stochastic reconstruction techniques have been proven to be very successful in generated virtual microstructure for large homogeneous polycrystalline materials for subsequent quantitative analysis.

An important assumption for the aforementioned stochastic reconstruction techniques is that the 2D micrographs contain a sufficiently large number of grains in order to lead to robust statistics. In addition, the spatial correlations between the grains with different shapes and sizes as well as the distribution of different grains were not explicitly considered in the reconstruction, assuming small variations in these characteristics. Although these assumptions are true in many engineering materials, it is also useful to devise techniques that reconstruct highly heterogeneous polycrystalline structures containing a small number of grains with large variation in grain size and morphology from 2D micrographs.

Let's take an example of a highly complex, multiscale microstructure of pure Sn alloy melted over copper, as shown in Fig.12. Fig.12(a) shows the EBSD image and a backscattered electron (BSE) image obtained via scanning electron microscopy (SEM) is shown in Fig.12(b). Fig.12(c) is the segmented BSE image showing the intermetallic particles. The microstructure of a pure Sn solder alloy consists of Sn-rich grains surrounded by a mixture of finely dispersed Cu_6Sn_5 intermetallic particles which form due to solid state diffusion of copper atoms, and their quantity depends chiefly on reflow temperature, reflow time, cooling rate [20, 21] and thermal aging [22]. Other

important microstructural features are the intermetallic layers of Cu_6Sn_5 and Cu_3Sn that form at the interface between the Sn solder and the copper substrate, and these are an essential component for good metallurgical bond. Solder alloys serve as the primary interconnection material in a microelectronic package and have been studied by researchers for several decades [23, 24]. There are several reported techniques for microstructural characterization and failure analysis in 2D and 3D and by both destructive and non-destructive methods [25, 26, 27, 28]. In this work, we use serial sectioning technique to experimentally obtain 3D crystallographic information in a solder volume. This technique is performed using conventional polishing coupled with SEM or EBSD mapping.

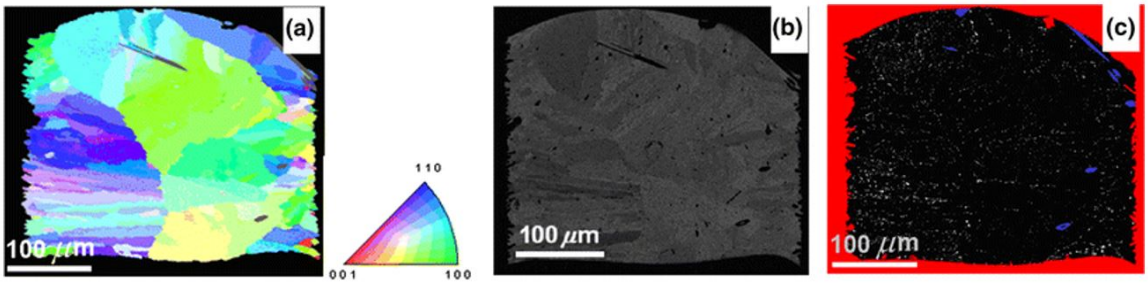

Figure 12: (a) Electron back-scatter diffraction (EBSD) image (i.e., orientation image map) of a Sn-based Pb-free solder joint. (b) Back-scatter electron (BSE) image of the joint. (c) Segmented BSE showing the distribution of fine intermetallic particles (white phase) in the joint. The dimension of the material is $350 \times 300 \times 45 \mu m$.

Synthetic reconstructions of a thin section of the polycrystalline microstructure as well as the distribution of intermetallic particles using serial sectioning techniques are shown in Fig.13. It can be clearly seen that the second phase precipitates possess a much lower volume fraction than the Sn-rich phase (i.e., the grains). In addition, the Sn-rich grains possess a large variation in their shape and size and a highly heterogeneous spatial distribution. Specifically, several large equiaxial grains are found in the middle of the system and a number of significantly elongated grains are clustered

close to the boundary of the system. This is due to the fact that during the growth process, the middle of the joint is under a more homogeneous temperature field and a small number of nuclei, while in the boundary region, the large temperature gradient and large number of nucleation sites lead to rapid directional growth. Furthermore, we find that a significant number of second phase intermetallic particles are distributed on the grain boundaries.

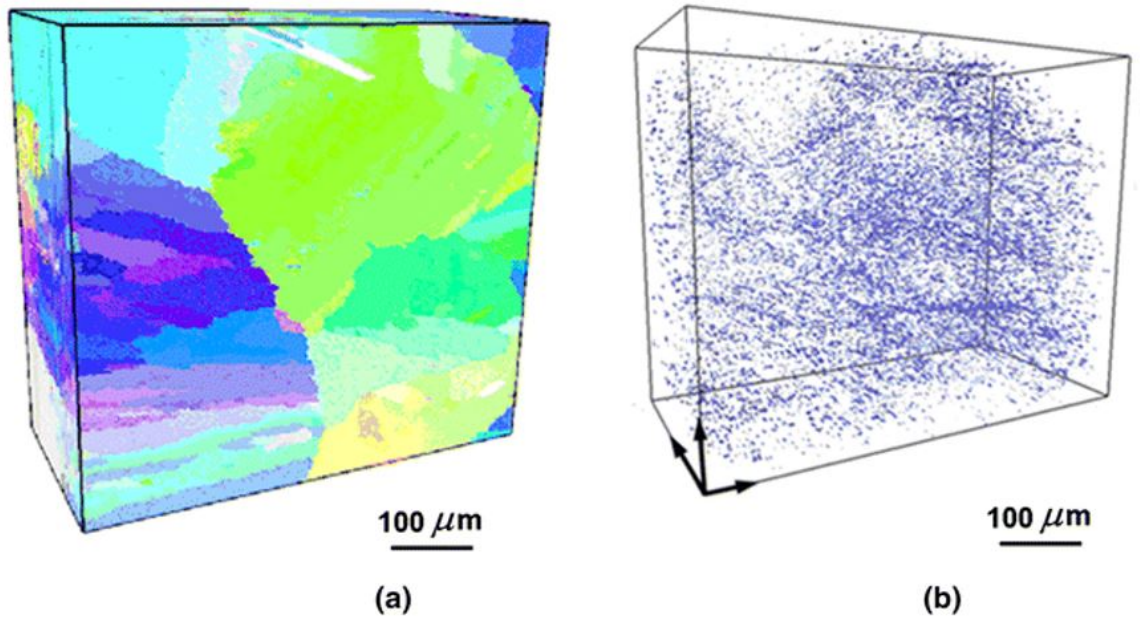

Figure 13: (a) Experimental reconstruction of a thin section of the polycrystalline microstructure using serial sectioning technique from the associated 2D EBSD dataset. (b) Experimental reconstruction of the 3D distribution of the intermetallic particles using serial sectioning technique from the associated 2D BSE dataset.

Statistically reproducing the aforementioned highly heterogeneous microstructural features in 3D virtual microstructure from a single 2D micrograph is very challenging and requires a novel stochastic reconstruction technique. Here, we propose a stochastic multi-scale computational procedure to reconstruct the 3D polycrystalline structure as well as the second phase particles. In particular, we employ the two-point correlation

function S_2 to statistically characterize the grain morphology, orientation correlation, and spatial distributions. The value of S_2 at r gives the probability of finding two randomly selected points separated by a distance r simultaneously falling into the same grain of interest in the system [29]. The original colored EBSD image is smoothed at a reasonable threshold to generate a grayscale image. The smooth step is very important, since the original quality of EBSD image is not very suitable for computer processing due to the fact that it is difficult to detect grains while filter out experimental noise. Moreover, it may be unfruitful to take efforts reconstructing grains of really small percentages because of their small influences on the overall spatial correlations. The S_2 of each grain in smoothed grayscale image will be computed and incorporated into the simulated annealing procedure devised by Yeong and Torquato[30, 31].

In addition, due to highly heterogeneous nature of the system, we decompose the microstructure into five different length scales (the algorithm works fine for more scales, but it will be more time-consuming), and reconstruct the structural features on each length scale separately. The large grains are generated first and smaller grains are then reconstructed. All the intermetallic particles are placed in the polycrystalline structure at last by matching the associated pair-correlation function sampled from the SEM micrograph. To ascertain the accuracy of the reconstruction, we quantitatively compare the grain size and orientation distribution of the virtually reconstructed microstructure with the experimentally obtained microstructure.

We note that a variety of other statistical descriptors have been developed to characterize different structural features a polycrystalline microstructure[32, 33, 34, 35]. In addition, other computational schemes such as the "branching" method [36] and the phase recovery method [37] have also been devised to represent polycrystalline microstructure from two-point statistics. Our approach distinguishes itself from the

aforementioned polycrystalline reconstruction methods in the following aspects: (i) it uses general correlation functions (extracted from 2D micrographs) instead of predefined shapes (e.g., ellipsoids) to characterize and model individual grains; (ii) it can effectively handle highly heterogeneous morphology with a wide distribution of grain shape and size via a multi-scale reconstruction framework; (iii) it integrates structural information in 2D EBSD and BSE micrographs to generate realistic 3D virtual microstructure with both polycrystalline grains and second phase intermetallic particles.

3.2 Statistical Microstructure Descriptors

3.2.1 n-point correlation function

In general, the microstructure of a heterogeneous material can be uniquely determined by specifying the indicator functions associated with all of the individual phases of the material[29, 38]. Without loss of generality, we focus on two-phase materials (binary medium) in this work. We note that the generalization of the subsequent discussion to a multiple-phase system is straightforward. Consider a statistically homogeneous material M occupying the region V in the d-dimensional Euclidean space ($d = 1, 2, 3$), which is partitioned into two disjoint phases: phase 1, regions V_1 of volume fraction ϕ_1 and phase 2, regions V_2 of volume fraction ϕ_2. It is obvious that $V_1 \cup V_2 = V$ and $V_1 \cap V_2$=0. The indicator function $I^{(i)}(\boldsymbol{x})$ of phase i is given by

$$I^{(i)}(\boldsymbol{x}) = \begin{cases} 1 & \boldsymbol{x} \in V_i \\ 0 & \boldsymbol{x} \in \bar{V_i} \end{cases} \tag{3.1}$$

for $i = 1, 2$ with $V_i \cup \bar{V}_i = V$ and$I^{(1)}(\boldsymbol{x}) + I^{(2)}(\boldsymbol{x}) = 1$. The n-point correlation function S_n^i for phase i is defined as follows:

$$S_n^{(i)}(\boldsymbol{x}_1, \boldsymbol{x}_2, \cdots, \boldsymbol{x}_n) = \langle I^{(i)}(\boldsymbol{x}_1) I^{(i)}(\boldsymbol{x}_2) \cdots I^{(i)}(\boldsymbol{x}_n) \rangle \tag{3.2}$$

where the angular brackets $\langle \cdots \rangle$ denotes the ensemble averaging over independent realizations of the medium. The two-point correlation function $S_2^{(i)}$ for phase i is defined by

$$S_2^{(i)}(\boldsymbol{x}_1, \boldsymbol{x}_2) = \langle I^{(i)}(\boldsymbol{x}_1) I_(^{(i)} \boldsymbol{x}_2) \rangle \tag{3.3}$$

For a statistically homogeneous medium, $S_2^{(i)}$ is a function of the relative displacements of point pairs, i.e.,

$$S_2^{(i)}(\boldsymbol{x}_1, \boldsymbol{x}_2) = S_2^{(i)}(\boldsymbol{x}_2 - \boldsymbol{x}_1) = S_2^{(i)}(\boldsymbol{r}) \tag{3.4}$$

where $\boldsymbol{r} = \boldsymbol{x}_2 - \boldsymbol{x}_1$. If the medium is statistically isotropic, $S_2^{(i)}$ is a radial function, depending on the separation distances of point pairs only, i.e.,

$$S_2^{(i)}(\boldsymbol{x}_1, \boldsymbol{x}_2) = S_2^{(i)}(|\boldsymbol{x}_2 - \boldsymbol{x}_1|) = S_2^{(i)}(r) \tag{3.5}$$

Interested readers are referred to Ref.[29] for a detailed discussion of $S_2^{(i)}$ and other higher-order $S_n^{(i)}$. Henceforth, we will drop the superscript i in $S_2^{(i)}$ for simplicity. Without further elaboration, S_2 will always be the two-point correlation function.

If the material of interest is anisotropic, a vector-argument $S_2(r)$ is generally required to characterize the system. For systems with a preferred direction (e.g., microstructure containing elongated grains along one direction), one can employ the directional two-point correlation functions to characterize the material, i.e., those computed along three orthogonal directions. Although the directional correlation functions do not contain the full set of structural information in $S_2(r)$, they have been shown sufficient to model anisotropic heterogeneous materials with elongated

inclusions[39, 40]. Therefore, we will employ the directional functions to characterize the grain morphology, orientation correlation and spatial distribution. However, in general, S_2 alone is not sufficient to uniquely determine the microstructure[41, 42].

3.2.2 Surface correlation function

The surface correlation functions contain information about the random interface in a heterogeneous system[43]. Since such statistics arise in and are of basic importance in the trapping and flow problems, it is conventional in that context to let phase 1 denote the fluid or void phase, and phase 2 denote the solid phase. The simplest surface correlation function is the specific surface $s(\boldsymbol{x})$ at point $\mathbf{x}$, which gives the interface per unit volume, i.e.,

$$s(\boldsymbol{x}) = \langle M(\boldsymbol{x}) \rangle \tag{3.6}$$

where $M(\mathbf{x})$ is the interface indicator function defined as the absolute gradient of the phase indicator function, i.e.,

$$M(\boldsymbol{x}) = |\nabla L(\boldsymbol{x})| \tag{3.7}$$

We note that for statistically homogeneous material, the specific surface is a constant everywhere and thus, is simply denoted by s.

The two-point surface correlation functions for a general heterogeneous material are defined by

$$F_{ss}(\boldsymbol{x}_1, \boldsymbol{x}_2) = \langle M(\boldsymbol{x}_1) M(\boldsymbol{x}_2) \rangle \tag{3.8}$$

and

$$F_{sv}(\boldsymbol{x}_1, \boldsymbol{x}_2) = \langle M(\boldsymbol{x}_1) L(\boldsymbol{x}_2) \rangle \tag{3.9}$$

which are respectively called the surface-surface and surface-void correlation functions[29, 43]. For statistically homogeneous and isotropic materials, the functions F_{ss} and F_{sv} only depend on the scalar distance $r = |\boldsymbol{x}_1 - \boldsymbol{x}_2|$. We note that, unlike S_n, the surface correlation functions do not have a direct probability interpretation, since the probability of finding a point exactly falling on the the interface is always zero. Instead, they can be associated with the probability of finding points in the dilated interface region with thickness δ in the limit $\delta \to 0$ [44].

3.2.3 Two point cluster function

The two-point cluster correlation function $C_2(\boldsymbol{x}_1, \boldsymbol{x}_2)$ gives the probability that two randomly selected points $\boldsymbol{x}_1$ and $\boldsymbol{x}_2$ fall into the same cluster of the phase of interest[45, 46]. For statistically homogeneous and isotropic materials, C_2 depends only on the relative distance r between the two points. It contains complete clustering information of the phases, which has been shown to have dramatic effects on the material's physical properties[29, 47]. However, unlike S_2 and the surface correlation functions, the cluster function generally cannot be obtained from lower-dimensional cuts (e.g., 2D slices) of a 3D microstructure, which may not contain correct connectedness information of the actual 3D system.

It has been shown that C_2 is related to S_2 via the following equation

$$S_2(r) = C_2(r) + D_2(r) \tag{3.10}$$

where $D_2(r)$ measures the probability that two points separated by r fall into different clusters of the phase of interest. In other words, C_2 is the connectedness contribution to the standard two-point correlation function S_2. For microstructures with well-defined inclusion, $C_2(r)$ of the inclusions is a short-ranged function that rapidly decays to zero

as r approaches the largest linear size of the inclusions. We note that although C_2 is a two-point quantity, it has been shown to encode higher-order structural information, which makes it a highly sensitive statistical descriptor over and above S_2. Fig.14 illustrates some of these statistical descriptors in a binary system.

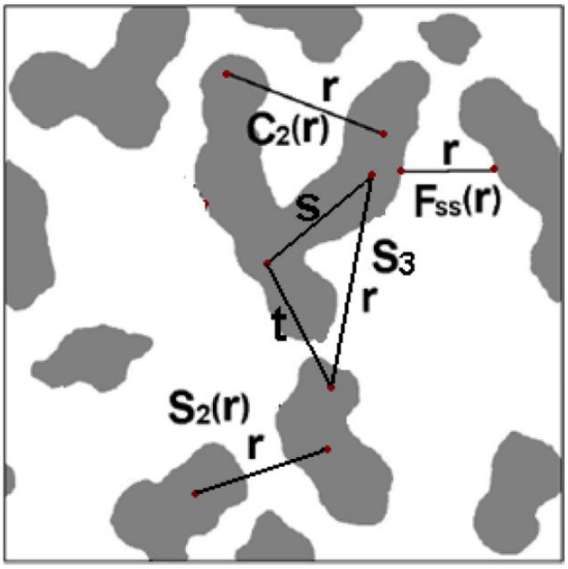

Figure 14: Schematic illustration of different correlation functions in a binary microstructure.

3.2.4 Pair correlation function

The pair correlation function g_2 of a particle system describes how average local number density varies as a function of the distance from a reference particle[48]. It is formally defined as below:

$$g_2(r) = \frac{1}{4\pi N r^2 \rho_0} \sum_{j=1}^{N} \sum_{\substack{i=1, \\ i \neq j}}^{N} \delta(r - r_{ij}) \tag{3.11}$$

where N is the total number of particles in the system, ρ_0 is the average number density, i and j represent different particles. In particular, the quantity $4g_2\pi r^2 dr$ is proportional to the probability of finding a particle which is away from the reference location with a distance of r. We will employ g_2 to characterize the distribution of intermetallic particles in the Sn matrix.

3.2.5 Effective grain size

Generally, a grain can possess an irregular shape and it is desirable to devise a parameter to characterize its linear size. Here, we only focus on 2D slices of a grain since the original statistics are obtained from 2D EBSD micrographs. Given a 3D reconstruction, the average grain size can be computed by considering separate 2D slices and averaging the result.

As shown in Fig.15(a), given a general grain shape, its effective linear size is defined as the average of radii of the inscribe circle R_i and the circumscribe circle R_c, i.e.,

$$R_{grain} = \frac{1}{2}(R_i + R_c) \tag{3.12}$$

We note that there are many different ways for defining an effective grain size. For example, the "number volume" (or area) based metrics have been suggested. Here, the reason we use the as-defined effective size is that in our system there are both equiaxed and elongated grains, which is difficult to characterize their sizes accurately in conventional way. In this a volume (area) based metric is less informative than this linear metric to characterize the anisotropy feature of the grains.

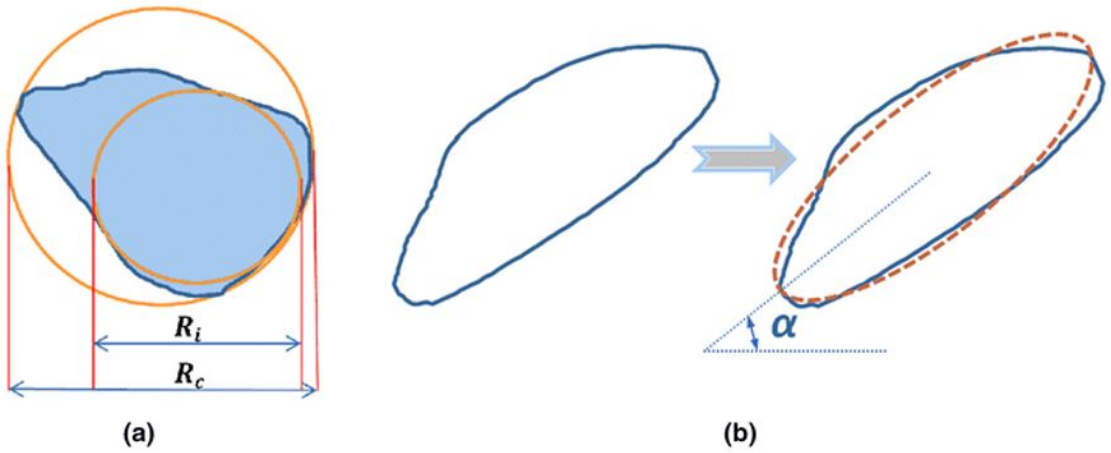

Figure 15: (a) The radii of inscribe circle and circumscribe circle associated with an irregular grain. (b) Illustration of the equivalent ellipse associated with a general anisotropic grain shape and its director defined as the rotation angle of the long semi-axis of the equivalent ellipse.

3.2.6 Director of anisotropic grains

In our system, a significant number of grains possess an elongated shape. How such anisotropic shapes are orientated in the microstructure is also an important characteristic of the microstructure and can be used to validate our reconstruction. We note the orientation of an anisotropic grain shape is a geometrical characterization of the polycrystalline microstructure and is to be distinguished from grain orientation, which refers to the orientation of the atomic lattice structure within the grain. In the subsequent discussion, we first introduce the concept of geometric moment and how it can be calculated, which is crucial to the characterization of the anisotropic grain shape.

In image processing, a geometric moment is defined as a weighted average (moment) of the intensity values associated with the pixels in the image[49]. Given a general shape, an associated equivalent ellipse can be defined as one possessing the same

geometric properties as the original shape, such as geometric moments. We then define the director of a general grain, which specifies the orientation of the anisotropic grain shape in the microstructure, as the rotation angle associated with the long semi-axis of the equivalent ellipse of the shape, see Fig.15(b).

For a 2D continuous function $f(x, y)$, which specifies a continuous intensity field, the geometric moment with an order of $(p + q)$ is defined as

$$m_{pq} = \iint_{\xi} x^p y^q f(x, y) dx dy \tag{3.13}$$

where ξ denotes integration over the entire field. For a scalar image with pixel intensity $I(x, y)$, its moment of $(i + j)$ can be calculated as :

$$m_{ij} = \sum_{x} \sum_{y} x^i y^j I(x, y) \tag{3.14}$$

The geometric center of the discrete intensity field $I(x, y)$ can be calculated as:

$$\bar{x} = \frac{m_{10}}{m_{00}}, \bar{x} = \frac{m_{10}}{m_{00}} \tag{3.15}$$

The central moment with an order of $(p + q)$ then is defined as:

$$u_{pq} = \sum_{x} \sum_{y} (x - \bar{x})^p (y - \bar{y})^q I(x, y) \tag{3.16}$$

Finally, the director of the grain shape as specified by the intensity field I(x,y) (or the rotation angle of the equivalent ellipse) can be computed as follows:

$$\alpha = \frac{1}{2} \tan^{-1}(\frac{2\mu_{11}}{\mu_{20} - \mu_{02}}) \tag{3.17}$$

3.3 Stochastic Multi-Scale Reconstruction Procedure

The basic idea of stochastic reconstruction procedure devised by Yeong and Torquato[41] is as follows: It's assumed that the microstructure of interest can be

statistically characterized by a set of correlation functions. If the microstructure is statistically homogeneous along a particular direction, the correlation functions computed from 2D slices normal to that direction can present the 3D structural features. Then one can incorporate such correlation functions into the simulated annealing procedure to reconstruct the 3D microstructure. Starting from an initial guess of the 3D microstructure, an "energy" function is defined as the sum of squared difference between correlation functions sampled from the initial guess and the corresponding target functions. The initial microstructure is evolved by exchanging a pair of pixels associated with different grains such that the energy is decreased on average. This amounts to a random walk in the "microstructural space". Energy-increasing exchange is allowed during the initial stage of the reconstruction as determined by the Metropolis rule (see definition below). The simulation is terminated if the energy is smaller than a prescribed threshold value (specified below for the current reconstruction).

In this work, we use S_2 to characterize the microstructure, which has been employed to model a variety of complex material systems[50, 51, 52, 53]. The energy function, defined as the sum of the squared difference between the two point-correlation functions associated with the target 2D micrograph and the 3D reconstruction, is gives as follows:

$$E = \sum_{\alpha=0}^{N} \sum_{r=0}^{L} [S_2^{\alpha,reconstr}(r) - S_2^{\alpha,target}(r)]^2 \tag{3.18}$$

where α indicates different grains and there are totally N grains in the system, r represents the separation vector between two points, and L is half of the linear size of target micrograph (i.e., periodic boundary condition is applied). As discussed below, we use directional correlation function to characterize the system, and thus r is chosen along three orthogonal directions.

A Monte Carlo method is used to evolve the system by exchanging the values of two randomly selected voxels belonging to different grains. The energy change due to

the exchange of these two voxels is then computed. The acceptance probability of a trial exchange is determined by the Metropolis method, i.e.,

$$p_{acc(old\rightarrow new)} = \begin{cases} e^{\frac{-E_{new}-E_{old}}{T}} & \text{if} \quad E_{new} \geq E_{old} \\ 1 & \text{if} \quad E_{new} < E_{old} \end{cases} \tag{3.19}$$

where E_{new} and E_{old} are the energy of the new and the previous (old) microstructures, respectively, T is an effective temperature which is chosen to be high initially (such that the initial acceptance rate of trial microstructures is roughly 0.5) and decreases as the simulation proceeds according to the cooling schedule $T(t) = 0.99^t T_0$, where t is time and T_0 is initial temperature. This process is continued until the energy is smaller than a prescribed threshold value, i.e., $E^* = 10^{-4}$, then the 3D reconstruction is considered complete.

In principle, this reconstruction procedure can be applied to any system with a finite number of grains. However, as the number of grains in the system increases, the associated computation cost will increase dramatically due to large number of correlation functions involved. From the definition of energy, it can be seen that adding one grain will lead to three additional terms in the summation, making the numerical minimization more difficult to achieve. Moreover, in our system the grain size and shape distributions are far from uniform. The grains with low volume fractions (minor grains) have less contribution to overall energy change in each evolution step compared to grains with high volume fractions (major grains). If all of the grains are considered together, the minor ones would suffer from a lower accuracy in the reconstruction. Generally, large grains have large value of S_2 and they will dominate during energy minimization, while the small ones have so small values of S_2 that their magnitudes may be very close to the minimization errors arising from the reconstruction of large grains, which significantly impairs the accuracy of reconstruction of small grains.

To solve this problem, we develop a multi-scale reconstruction procedure, in which we reconstruct the grains on different length scales (i.e., with different volume fractions) separately. It works as follows: We first define an index called "importance factor" for each grain, which is simply chosen to be the volume fraction of that grain. In other words, the larger the volume fraction, the more important the role this grain plays in the reconstruction. In this way, we "quantify" the importance of each grain and first explicitly reconstruct the major grains with volume fractions while coarsening the minor grains. In this work, we use a threshold value $\phi_c = 0.1$ to determine the major grains. Thus, the minor grains, that possess a relative volume fraction smaller than ϕ_c, are merged temporarily into single grains and reconstructed together with the original major grains in the system. When the major grains are successfully reconstructed, the reconstruction domain is restricted to the merged grain regions within which the minor grains are reconstructed. We repeat this process until it is not necessary to further merge minor grains. In fact, the reconstruction works best if the smaller grains are spatially clustered, so they can naturally be treated as a large cluster. However, the general stochastic reconstruction method can also generate reasonable reconstructions if the small grains are randomly dispersed in the structure. This is because the spatial statistics, i.e., the two-point correlation functions used to characterize the grains, contain information on both grain morphology (i.e., in the short-range behavior of S_2) and spatial correlation between the grains (i.e., in the long-range behavior of S_2). We note that two orientations that are spatially separated (not the same grain) would show up as a single grain cluster, which may introduce physical inconsistencies to grain orientation distribution in the reconstructed result. Therefore, our reconstruction method is restricted to grain morphology reproduction in 3D from 2D microstructural information. This procedure allows us to reconstruct

the morphology of minor grains with the same level of accuracy as the major grains. Given sufficient computational resources, this approach can handle a material system with a large number of grains with a wide range of shapes and sizes.

3.4 Reconstruction of 3D Grain Morphology and Orientations

3.4.1 Image analysis

The original EBSD micrograph is a colored grain orientation map, with each color indicating a specific orientation of the grain. To obtain the EBSD image, the sample, which is a pure Sn solder joint with butt joint geometry, was polished to a final finish of $0.05\mu m$ colloidal silica to obtain mirror finish quality, as required for performing EBSD. Scanning electron microscope (JEOL JSM-6100) equipped with TSL EBSD system was used to obtain EBSD patterns of the solder joint. The patterns were collected at a step size of $0.6\mu m$ on the entire solder joint cross-section area of about $300 \times 300\mu m$. These patterns were analyzed for its crystal orientation and then color coded using TSL OIM data collection and analysis software. To reduce the noise, the EBSD micrograph was processed using 'single average orientation' cleaning procedure inbuilt in the analysis software. This method provided the information for one complete cross-section. From here, the 3D experimental dataset is collected by using serial sectioning process. Mechanical polishing was done using a semi-automatic polisher which was standardized to polish a section depth of $2\mu m$ every step. EBSD maps were obtained at every polishing step and Avizo® Fire (VSG, Burlington, MA) software was used to import these images as a stack. 3D voxels were then defined by interpolation, thereby rendering the entire experimental volume in 3D.

For purposes of reconstruction, we consider that each color within the EBSD micrograph is associated with a "grain cluster", and convert the original orientation map into a multi-grain-cluster microstructure. Since the orientation map inevitably contains noise, we now describe our approach for image smoothing and extracting different grain clusters from the smoothed image. We select a rectangular portion of the micrograph as the reconstruction target and convert it from a RGB image into to an eight-bit grayscale image, in which each color in the original micrograph has a gray value ranging from 0 to 255. A histogram showing the distribution of the number of pixels over the gray values is obtained, which contains significant peaks at certain gray values, corresponding to distinct grains, see Fig.16(b). We then smooth the image by selecting the gray values associated with significant peaks and binning the remaining pixels to the closest peak values to form larger grain clusters. The smooth is done by removing the phases with volume fraction less than 0.01 and assign these pixels with the new value of their nearest neighbor with the largest frequency. The smoothed image, which contains 53 distinct grain clusters, is shown in Fig.16(a).

Once the smoothed target multi-grain-cluster microstructure is obtained, we now proceed to sample the correlation functions. Note that we assume that this single 2D image can statistically represent the 3D microstructure. This assumption might not be true for a general heterogeneous material. To verify our assumption, we need to examine the preparation history of the material. The solidification of solder joint and the associated grain growth are very sensitive to the temperature gradient. In this system, the temperature gradient is uniaxial, perpendicular to the two parallel surfaces of the wires to be joined. This leads to a transversely statistically homogeneous microstructure, i.e., the morphology of the cross section of joint perpendicular to the temperature gradient is statistically homogeneous. Therefore, the correlation function

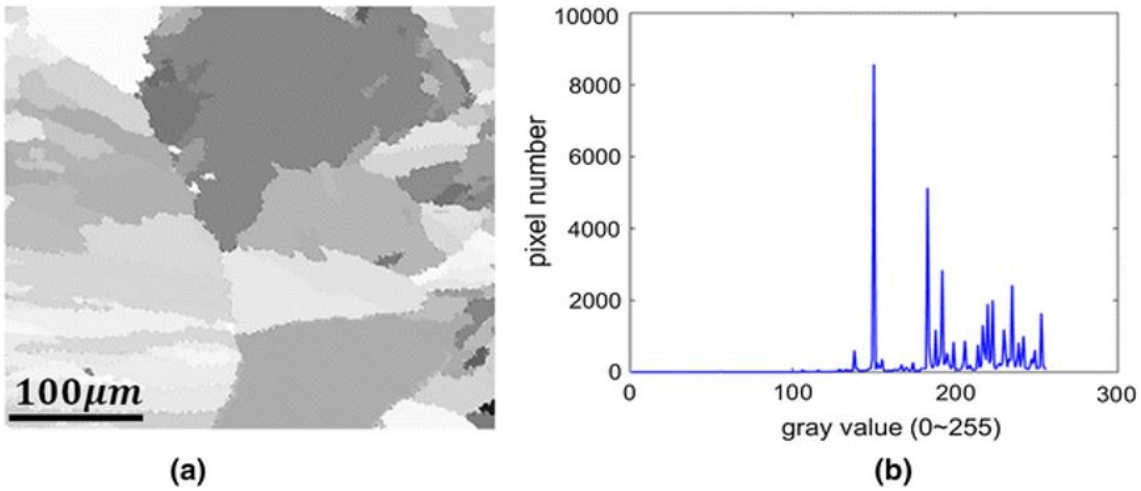

Figure 16: (a) The smoothed grayscale image, which contains 52 grain clusters. (b) The histogram showing the distribution of gray values in the non-smoothed grayscale image. A number of peak values can be clearly seen, which are selected for binning the remaining pixels to obtain a smoothed image. The linear size of the system is 300 by 240μm.

along the vertical direction sampled from the 2D micrograph should be sufficient to statistically represent the cross sectional morphology.

As discussed before, we employ the directional correlation functions to characterize the anisotropic grains. Recently studies have shown that S_2 along three orthogonal directions are sufficient to represent a wide class of anisotropic microstructure. Since the joint microstructure is transversely statistically homogeneous, we consider that S_2 along the two orthogonal directions in the transverse plane are identical and can be presented by the S_2 along the vertical direction in the 2D micrograph. Similarly, the S_2 along the horizontal direction in the 2D image quantify the microstructure along the temperature gradient in 3D. In the subsequent reconstructions, we will only consider the auto-correlation functions of the 53 grain clusters, which are shown in Fig.17. Previous studies have shown that the auto-correlation functions are sufficient to accurately represent the shape and size of individual grains. Since the spatial

correlations between different grains are taken into account via the length-scale decomposition, we do not incorporate the set of cross-correlation functions into the reconstruction. This will significantly reduce the computational cost without scarifying accuracy.

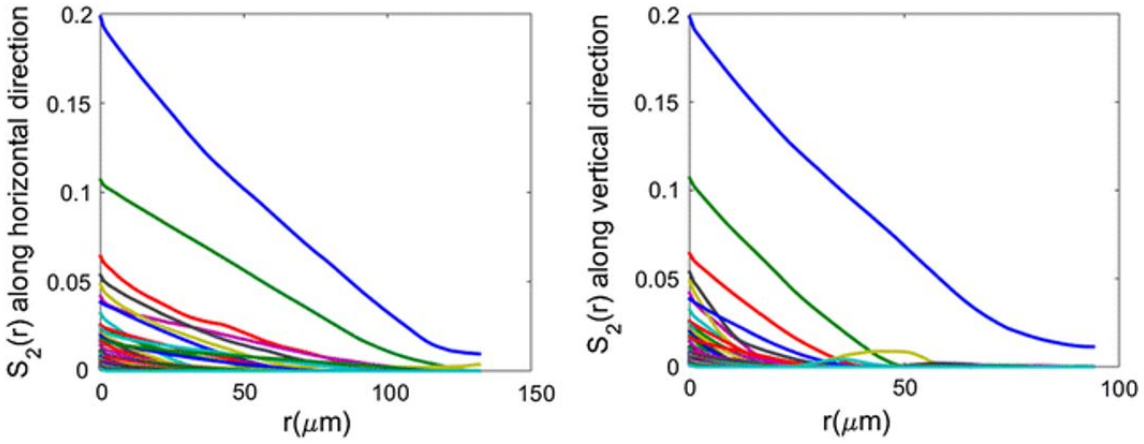

Figure 17: Directional two-point correlation functions associated with 53 different grain clusters in the smoothed grayscale image of the polycrystalline structure. (a) S_2 along the horizontal direction and (b) S_2 along the vertical direction.

3.4.2 Multi-scale Reconstruction Results

We now apply the multi-scale reconstruction procedure to our multi-grain-cluster microstructure. As discussed before, this procedure leads to better convergence for system with a large number of distinct grains and can significantly improve the reconstruction accuracy for grains with small volume fractions. Recall that we first merge the minor grains to produce temporary grain clusters of fairly large volume fraction, and subsequently restore the minor grains within the temporary grain

cluster. For the current system, the aforementioned process is repeated five times and reconstruction process is illustrated in Fig.18.

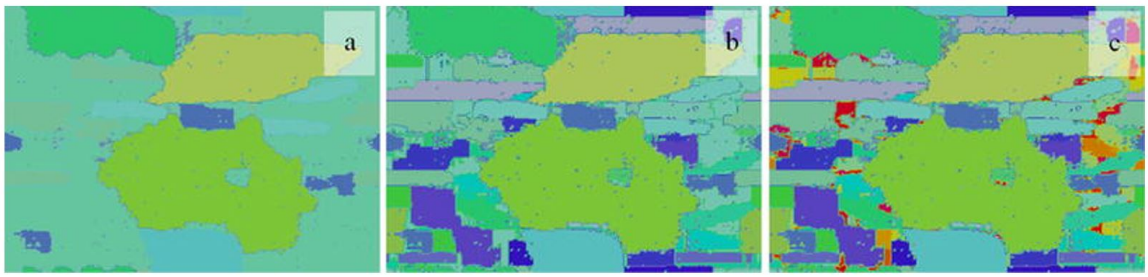

Figure 18: Illustration of the multi-scale synthetic reconstruction process (a through c). The minor grains are initially merged to generate temporary grain clusters, which are then restored in subsequent reconstructions. The linear size of the system is 300 by 240μm.

The final 3D reconstruction is shown in Fig.19. A filter is also applied to remove isolated voxels to further smooth the microstructure. This step is designed because there are a large amount of isolated pixels located at grain boundary and within the grains, which may be reconstructed small grains or computational artifacts. Because we cannot distinguish the small grains from computational artifacts and these isolated pixels significantly add the complexity to detecting individual grains, they are simply smoothed out here to avoid errors during post analysis. It can be clearly seen from the smoothed microstructure that a few large grains are distributed in the middle of the system and elongated small grains are distributed close to the boundary. In addition, the reconstructed microstructure is transversely homogeneous. These results indicate that our 3D reconstruction has qualitatively reproduced the salient morphological features of the target microstructure.

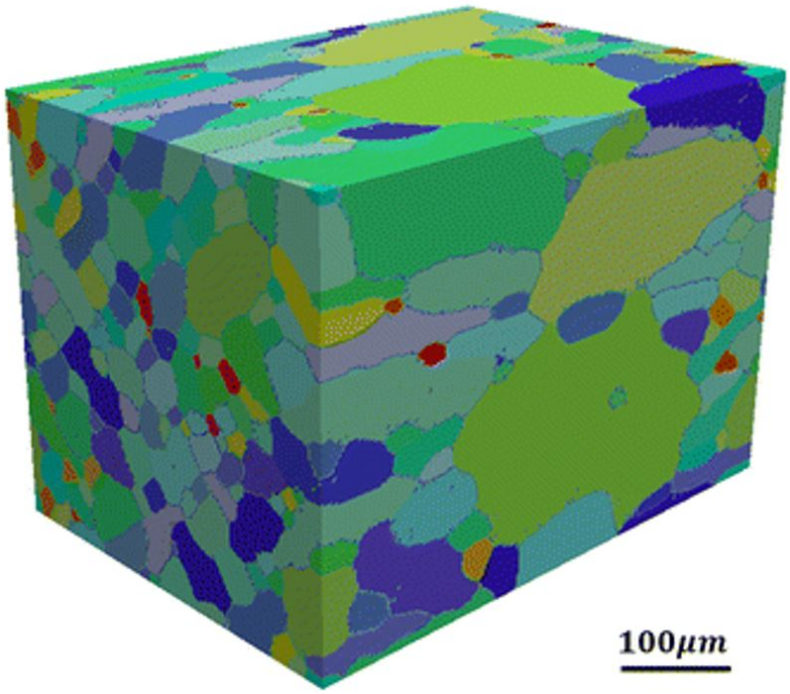

Figure 19: Virtual synthetic 3D reconstruction of the polycrystalline microstructure, which successfully reproduces the salient features of the target 2D EBSD micrograph and smoothed grayscale image obtained from experiment). The dimension of the system is 300 by 240 by 240μm.

3.4.3 Comparison of grain morphology statistics

To quantitatively verify the accuracy of the reconstruction, we compare the grain morphology statistics, i.e., the distribution of linear grain size and grain directors obtained from the virtual 3D structure and that of the target micrograph. Since only a thin section of the system is reconstructed using serial sections (see Fig.13), the morphology of larger grains may not be sufficiently obtained. Moreover, the virtual microstructure is reconstructed from quite limited information obtained from a single slice of EBSD image and based on the assumption that the microstructure of the material is transversely homogeneous and can be effectively characterized by the single

EBSD image, a comparison of microstructural information extracted from slices of the stochastically reconstructed and that of target slice should be sufficient. The statistics for the 3D system are obtained by considering individual 2D slices of the structure. As shown in Fig.20(a), the grain size distribution in the reconstruction agrees very well with that in the target 2D image, both of which contain a large number of small-sized grains. In addition, the grain size distribution of 3D reconstruction is smoother than the 2D image, indicating a larger number grains contributing the statistics. The comparison of grain director distributions is shown in Fig.20(b). It can be seen that the distribution in both the target image and reconstruction exhibit a peak around the zero degree with respect to the horizontal axis. This indicates that the anisotropic grains are elongated along the horizontal direction, which is also the direction of the temperature gradient. The excellent agreement of the grain morphology statistics between the target and reconstruction suggests that our 3D virtual microstructure is statistically robust and accurate.

3.5 Dynamic reconstruction

Although the standard two-point correlation function S_2 has been widely used in microstructure reconstructions, it has been found that large structural degeneracy could exist in the reconstruction, which leads to uncertainties and inaccuracies for nearly percolating systems. To improve reconstruction accuracy and reduce structural degeneracy, one can successively incorporate additional morphological information (e.g., nonconventional or higher-order correlation functions) from a dynamic process like sintering, which amounts to reshaping the energy landscape to create deep (local) energy minimum. In this paper, we present a dynamic reconstruction procedure

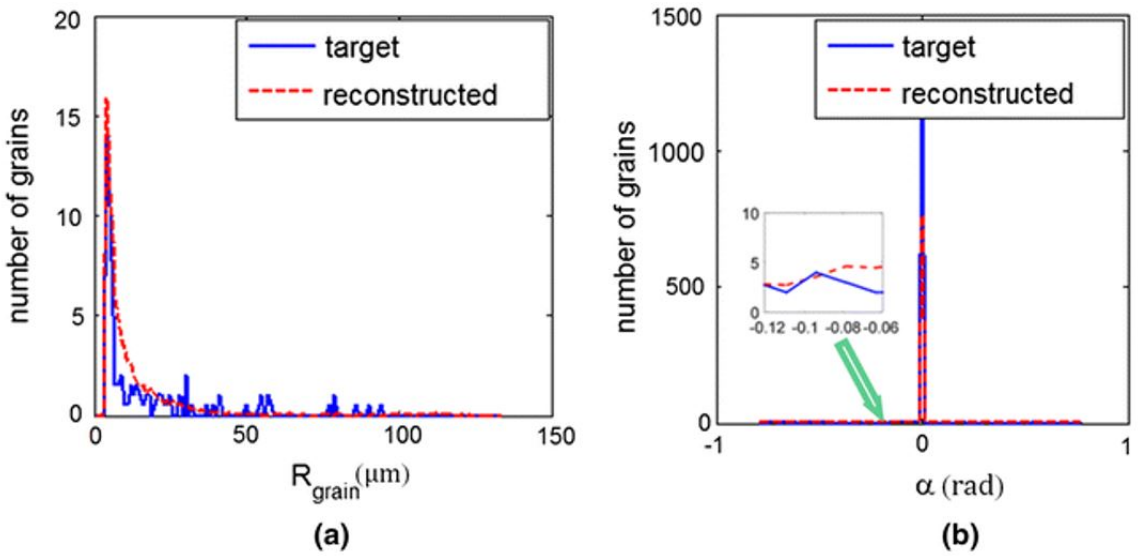

Figure 20: Comparison of (a) grain size distributions and (b) grain director distributions between the target 2D EBSD micrograph and the synthetic reconstruction.

that allows one to additively use a series of S_2 to achieve high level of accuracy. In particular, instead of randomly sampling the microstructure space as in the simulated annealing scheme, our procedure utilizes the series of microstructures that comes from a physical structural evolution process (e.g., densification in sintering, grain growth in phase transition). In contrast to commonly used evolution reconstruction approaches that separately generate individual static configurations, our procedure continuously evolves a single microstructure according to a time-dependent correlation function. The utility of our procedure is illustrated by successfully reconstructing constantly growing to nearly percolating hard-sphere packings and particle-reinforced composites as well as the coarsening process in a binary metallic alloy.

3.5.1 Computing correlation functions from images

The aforementioned correlation functions can be effectively computed from given digital images of a material, in which the microstructure is represented as a 2D (or 3D) array of pixels (or voxels). In such arrays, each entry indicates the local state (e.g., phase) of that pixel. For a binary system, the array is simply a collection of black and white pixels on a regular lattice. The probabilistic interpretation of the correlation functions enable us here to develop a general sampling method for reconstruction of statistically homogeneous and isotropic digitized textures based on the lattice-gas formalism, which is introduced in ref.[44] and generalized in ref.[41]. In the generalized formalism, pixels with different values (occupying the lattice sites) correspond to distinct local states and pixels with the same value are considered to be molecules of the same gas species. The correlation functions of interest can be obtained by binning the separation distances between the selected pairs of molecules from particular species.

For example, the standard two-point correlation function S_2 can be computed as follows:

$$S_2(r) = N_P(r)/N_S(r) \tag{3.20}$$

where $N_S(r)$ is the number of lattice-site separation distances of length r and $N_P(r)$ gives he number of molecule-pair separation distances of length r. The two-point cluster function C_2 is given by

$$C_2(r) = \sum_i N_P^i(r)/N_S(r) \tag{3.21}$$

where $N_P^i(r)$ denotes the pair distances of length r between the molecules within the

same cluster i. The surface-surface correlation function F_{ss} can be obtained by

$$F_{ss}(r) = N^{ss}(r)/N_S(r) \tag{3.22}$$

where $N_{ss}(r)$ gives the number of distances between two surface molecules with length r.

3.5.2 Algorithm

In the original YT scheme, the microstructure space is randomly sampled and thus, the evolution of the trial microstructure during the reconstruction is not associated with any physical process. In addition, the convergence of the reconstruction strongly depends on the energy landscape defined over the microstructure space. For certain nearly percolating systems (e.g., dense particle packings), the energy landscape associated with the reconstruction using $S_2(r)$ alone is very rough and contains many local minima, which usually lead to large structural degeneracy and inaccurate reconstructions. For example, in a typical reconstructed structure, the degree of clustering is significantly overestimated and the particle phase, which is supposed to be disconnected, usually percolates and forms a system spanning cluster [42, 54]. One approach to reduce structural degeneracy is to incorporate additional correlation functions such as C_2 and F_{ss}, which reshape the energy landscape to create a deep (local) energy minimum with a wide and smooth basin of attraction. Such a minimum is usually associated with a high probability being visited and selected by the random microstructure research.

The dynamic reconstruction procedure we devise here uses successive energy landscapes to bias the microstructure evolution towards a favored reconstruction. This allows one to use a series of S_2 to achieve the same level of reconstruction accuracy

as those incorporating additional nonconventional correlation functions. It works as follows: given each digitized two-phase microstructure (2D or 3D) possessing a volume fraction $\phi^{(0)}$ for each phase of interest at the beginning of process, the associated two-point correlation function $S_2^{(0)}(r)$ is computed. Then microstructure evolution proceeds by one time step, which results in a slightly modified volume fraction of each phase, i.e., $\phi^{(1)}$ and the associated two-point correlation function $S_2^{(1)}(r)$ is computed. This process is repeated n times until the process comes to an end or become equilibrium, which results in a series of correlation functions $\{S_2^{(0)}(r), S_2^{(1)}(r), S_2^{(n)}(r)\}$.

To reconstruct the dynamic system, we start from $S_2^{(0)}$ associated the lowest volume fraction $\phi^{(0)}$ and a corresponding microstructure is then reconstructed using the YT procedure, which has been shown to be highly efficient in generating accurate reconstruction at such low ϕ. The reconstructed microstructure is then used as the initial configuration for reconstructing the structure with $\phi^{(1)}$ from $S_2^{(1)}$. Specifically, a new trial microstructure is generated from the current configuration by adding pixels to randomly selected locations at the surface of each phase to increase the volume fraction from $\phi^{(0)}$ to $\phi^{(1)}$. Then YT procedure is applied in which only surface pixels are randomly selected and displaced on the surface. The resulting new trial microstructure is accepted with a Metropolis probability and simulated annealing is used to evolve the system.

We note that this approach is distinct from a conventional YT procedure in two aspects: (i) an initial configuration from last step is used at each new reconstruction, which is already in the basin associated with an energy minimum; (ii) more efficient evolution kinetics that only involves displacing surface pixels is employed. This corresponds to evolve the energy minimal configuration $M^{(k)}$ associated with $S_2^{(k)}$ to the nearest energy minimal configuration $M^{(k+1)}$ in the energy landscape associated with

$S_2^{(k+1)}$ via surface optimization. This process is repeated to successively generate a series of microstructures $M^{(k)}, M^{(k+1)}, \cdots, M^{(n)}$ in order to finally accurately reconstruct the microstructure evolution of the process. It can be seen that during the entire reconstruction process, a series of energy landscapes are constructed, each associated with a $S_2^{(k)}(k = 0, 1, \cdots, n)$. These landscapes successively and additively bias the evolution path of the trial microstructure to improve the convergence of the reconstruction (see Fig.21). Our procedure is also different from a recently developed dilation and erosion method[51, 55], which transforms a topologically complex structure to simpler one, and utilizes appropriate topological descriptors such as C_2 for accurate reconstructions of the original system. In our case, the series $\{S_2^{(0)}(r), S_2^{(1)}(r), S_2^{(n)}(r)\}$ characterizes snapshots of the materials at successive time points during the evolution and thus, which can be considered as a single time-dependent correlation function evaluated at different time points. In contrast to commonly used evolution reconstruction approaches that separately generate individual static configurations, our procedure continuously evolves a single microstructure according to a time-dependent correlation function.

3.5.3 Reconstructing nearly percolating microstructure

In this section, we apply the dynamic reconstruction procedure to generate virtual microstructures of 3D binary heterogeneous materials in which one of the phases is nearly percolating. Specifically, two systems are considered here: a packing of equal-sized hard spheres[56] and a SiC particle reinforced Al-matrix composite [57] with a particle phase volume fraction close to the corresponding percolation thresholds. Previous studies have shown that the standard YT reconstruction using S_2 alone

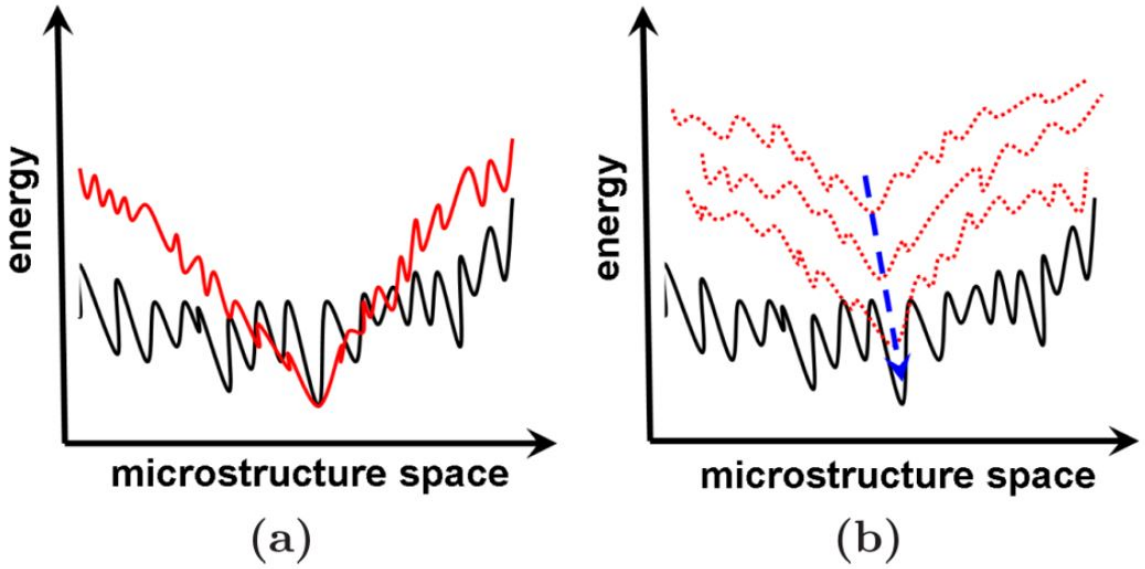

Figure 21: Schematic illustration of different modifications of energy landscape to improve convergence for different reconstruction methods within the Yeong-Torquato framework. The original funnel energy landscape associated with S_2 is illustrated by the black curve in both panels. (a) Incorporating additional correlation functions amounts to reshaping the energy landscape to create deep (local) energy minimum with a wide and smooth basin (red curves or dark gray curves in print version). (b) The dynamic reconstruction utilizes a series of energy landscapes (dashed red curves) to bias the convergence of reconstruction to the favor microstructure.

significantly overestimates the degree of clustering of the particle phase in such systems. In the following, we will show that our procedure not only correctly reproduces the connectedness of the particle phase but also reasonably resolve the shape and size distribution for the SiC particles.

3.5.3.1 SiC/Al composite

Fig.22 shows a model microstructure of SiC-particle reinforced Al-matrix composite [58] with particle volume fraction $\phi = 0.31$. It can be seen that the isotropic SiC particles possess a wide size distribution. Although the final volume fraction is close

to the percolation threshold, the particle phase is still disconnected, which makes the system very difficult to reconstruct using the standard YT procedure based on S_2 alone. The process is a DEM modeling of the growth of SiC particle, which starts from equal-sized nuclei and then coarsens at various rates until its volume fraction reaches 0.31.

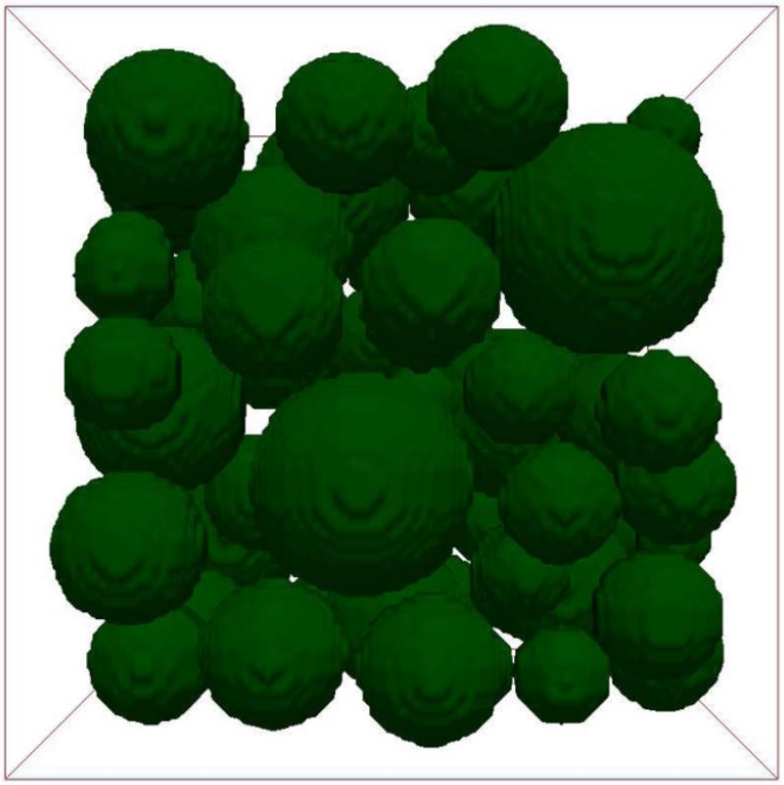

Figure 22: A SiC-particle reinforced Al-matrix composite material with final particle volume fraction $\phi = 0.31$. Only the particle is shown and the matrix is transparent. The linear size of the system is $200\mu m$. The whole system is digitized into 100 by 100 by 100 voxels.

The computed correlation functions $S_2^{(j)}$ are employed to successively reconstruct the microstructures, see Fig.23. The final reconstruction is shown in Fig.24(a). It can be clearly seen that the size distribution of SiC particles are very well resolved in

the reconstruction. This is also quantitatively indicated from the comparison of the two-point cluster function C_2 and surface-surface correlation function F_{ss} computed from the target and the reconstruction, as shown in Fig.24(c, d). Also shown is the reconstructed system using the standard YT procedure from S_2 alone (Fig.24(b)), in which the clustering of the particle phase is again significantly overestimated.

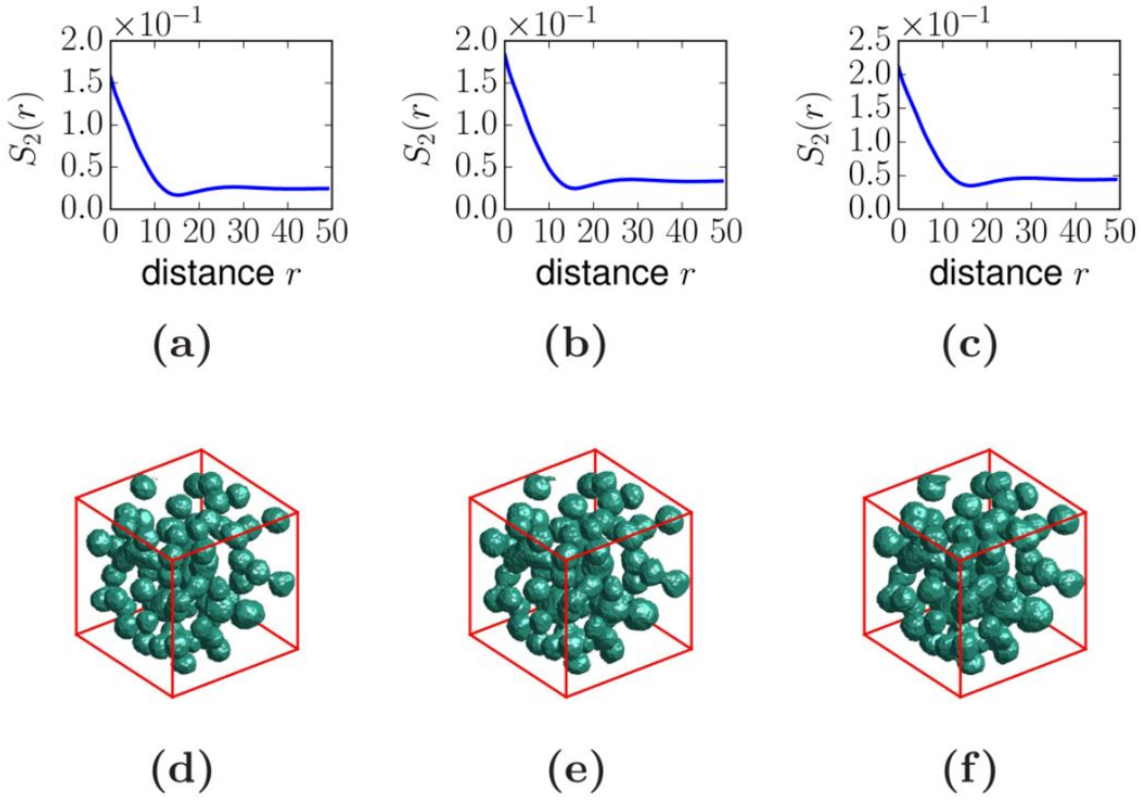

Figure 23: Dynamic reconstruction of the SiC/Al composite system. (d)-(f) Intermediate structures are successively reconstructed from the (a)-(c) associated correlation functions based on previously reconstructed structures as favored initial configurations.

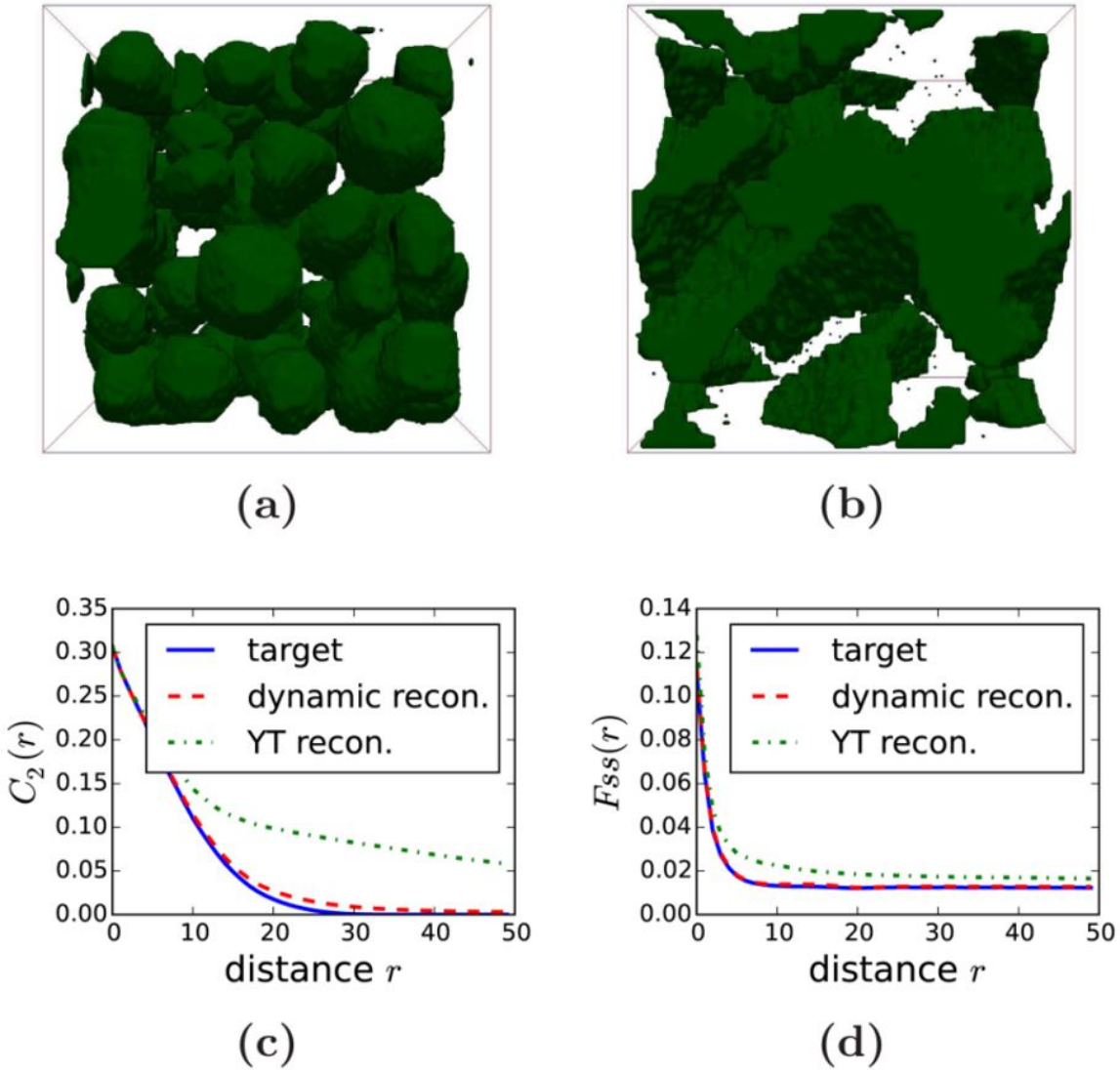

Figure 24: Reconstructed systems based on S_2 alone. (a) Dynamics reconstruction. (b) Standard YT reconstruction. Comparison of (c) C_2 and (d) F_{ss} computed from the target and reconstructed microstructures.

3.5.3.2 Reconstructing microstructure during coarsening

In this section, we apply the dynamic reconstruction procedure to reproduce the microstructure coarsening process in a binary lead/tin alloy aged at 448 K up to 216 hours[52]. It has been shown that the scaled autocorrelation function of this system,

i.e.,

$$f(r) = \frac{S_2(r) - \phi^2}{\phi(1-\phi)} \tag{3.23}$$

which is same for both the Pb-rich and Sn-rich phases, can be approximated via the following expression

$$f(r;t) = \exp[-ar/\lambda(t)]\cos[\pi r/\lambda(t) + b]/\cos(b) \tag{3.24}$$

where $a = 3.5$ and $b = 0.60$ are dimensionless fitting parameters depending on the aging temperature and Pb composition and

$$\lambda(t) = [\lambda_0^3 + (\lambda_f^3 - \lambda_0^3)\frac{t}{t_f}]^{1/3} \tag{3.25}$$

where λ_0 and λ_f are respectively the length scale in the as-processed and final aged microstructures, and t_f is the associated time of aging.

To reconstruct the coarsening process, the two-point correlation function S_2 of the Pb-rich phase is computed at different time points during the evolution. The dynamic reconstruction is employed to successively evolve the microstructure according to the series of S_2, see Fig.25. We note that the coarsening process is diffusion controlled, thus, the phase morphological changes occur through the two-phase interface. This makes the surface-evolution kinetics utilized in our reconstruction procedure naturally mimics the actual physical evolution process, and therefore highly efficient in reconstructing the structural evolution.

To quantitatively ascertain the quality of the reconstruction, the reconstructed system at selected time points are compared both visually and qualitatively to the 2D optical micrographs of the alloy at the corresponding time points during the aging experiment, see Fig.26(a,b). Fig.26(c,d) respectively show the two-point cluster function C_2 and surface-surface correlation function F_{ss} computed from the 2D micrographs

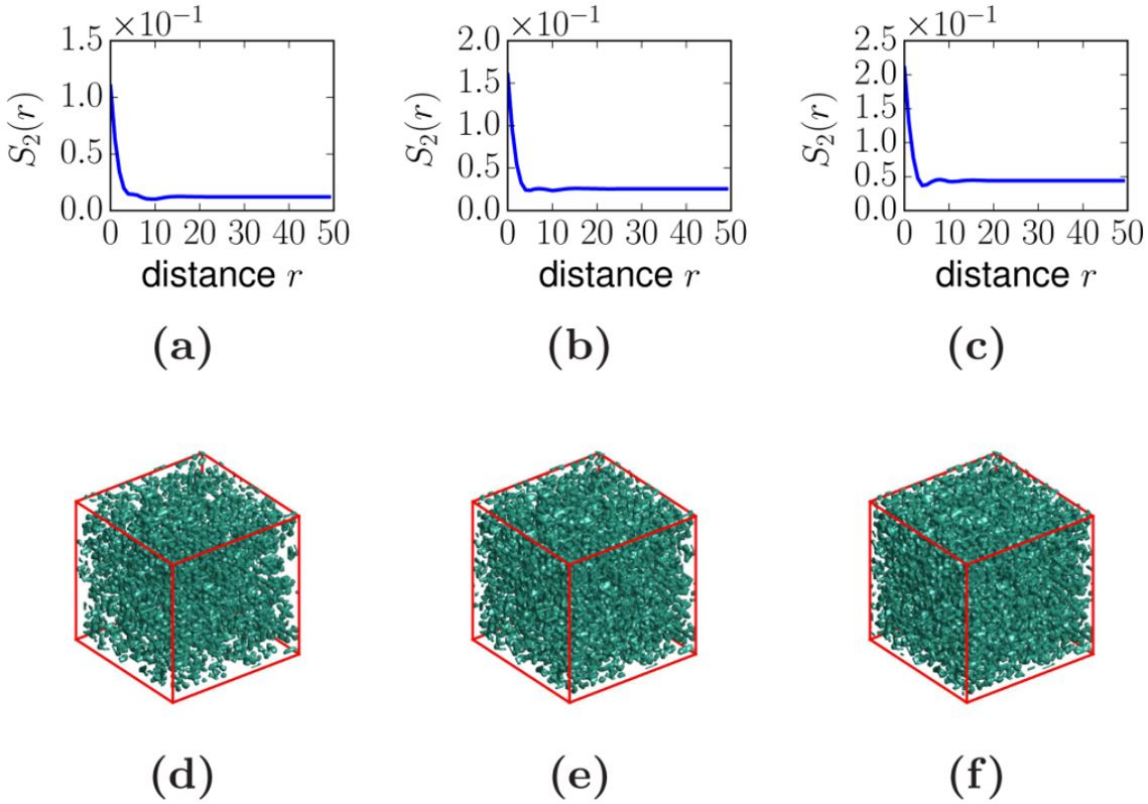

Figure 25: Reconstruction of the coarsening process in a lead/tin alloy from a time-dependent correlation function. (a)-(c) S_2 at different time points during the evolution (i.e., respectively 12, 24, and 48 hours after annealing starts). (d)-(f) The associated microstructures generated using the dynamic reconstruction in which only the Pb-rich phase is shown. The coarsening of the phase is apparent. The linear size of the system is $250\mu m$. The total annealing time for the alloy is 216 hours.

and 2D slices of the reconstructed alloy structures. The excellent agreement between the reconstructed and experimental correlation functions clearly indicates the accuracy of the dynamic reconstruction in reproducing the entire microstructure evolution process.

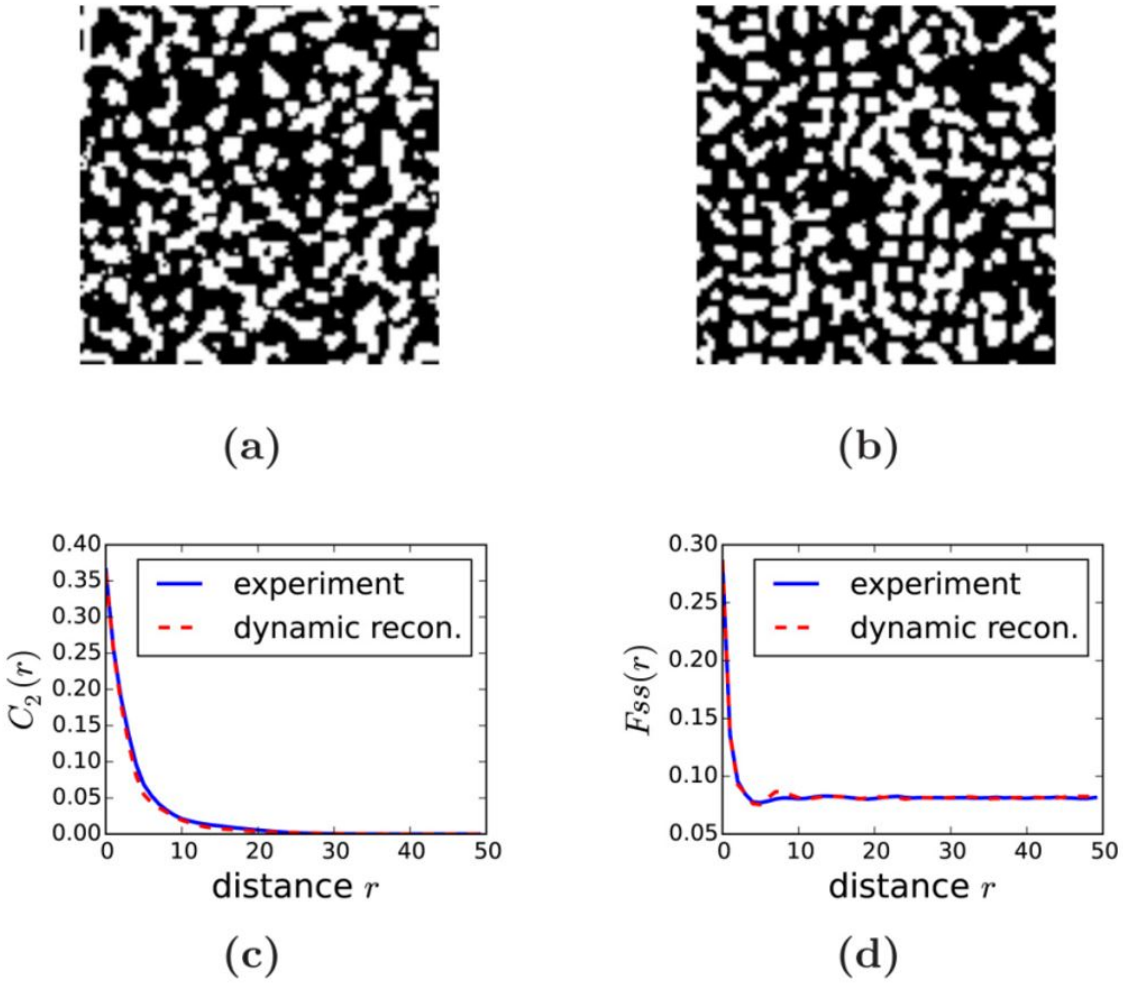

Figure 26: Top: Comparison of (a) a 2D optical micrograph of the alloy at 36 hours after annealing starts and (b) a corresponding 2D slice of the reconstructed structure at the same time point. Bottom: Comparison of the two-point cluster functions (c) C_2 and the surface-surface correlation function (d) F_{ss} for the experimental and reconstructed systems.

3.6 Summary

We have developed novel simulated annealing based Monte Carlo method to model both static microstructure and morphology evolution during physical processes. For static reconstruction, we use S_2 for each phase along two orthogonal directions and YT

procedure to reconstruct statistically similar 3D microstructure to the input microstructure. For evolving microstructure, we have invented a layer-by-layer reconstruction scheme which allows one to use a series of S_2 to accurately reconstruct heterogeneous materials in which one of the phases is nearly percolating. Such systems are extremely difficult to reconstruct using the standard YT procedure, which usually significantly overestimates the degree of clustering unless additional nonconventional correlation functions containing appropriate topological information are incorporated. Different from the YT scheme in which the microstructure space is randomly sampled, our procedure utilizes a series of energy landscapes and surface-evolution kinetics to bias the microstructure evolution path and improve the convergence of the reconstruction. This dynamic procedure can be naturally applied to reconstruct any microstructure evolution process by continuously evolving the microstructure at each stage according to a time-dependent correlation function. The utility of our procedure is illustrated by successfully reconstructing systems containing well-separated particles or phases with volume fraction near percolation point, i.e., the hard-sphere packing and SiC/Al composite, as well as a system containing bi-continuous interpenetrating phases of binary lead/tin alloy. These examples clearly validate the accuracy and efficiency of the dynamic reconstruction procedure in generating a wide class of complex microstructures and structural evolution. Although the two-point correlation function S_2 is employed as the input structural information for dynamic reconstruction, this procedure can be easily generalized to utilize other stochastic morphological information. For instance, limited-angle projections obtained via in situ x-ray tomography can be used to reconstruct the continuous evolution of a single material due to external stimuli[59]. This will significantly reduce the cost to separately reconstruct individual material microstructures at discrete time points.

The results demonstrated in this chapter are published in Metallurgical and Materials Transactions A 47, 1440 (2016) and Physical Review E 92, 023301 (2015).

Chapter 4

MODELING MICROSTRUCTURE EVOLUTION OF SOLID-STATE SINTERING

4.1 Background

In previous chapters, we have introduced two basic material simulation methods, DEM for powder packing and stochastic reconstruction of microstructure from low dimension (2D) to high dimension (3D), both of which can be incorporated in a lot of occasions. In this chapter, we are presenting our effort towards establishing a combinative modeling technique of DEM and kinetic Monte Carlo method for a common manufacturing process, the solid-state sintering, where DEM is used to generate powder packing and kinetic Monte Carlo is used to simulate microstructure evolution during sintering.

Solid-state sintering is a widely used material processing and manufacturing method[60, 61, 62]. The final sintered material microstructure is generally affected by the physical and chemical properties of the material (e.g., viscosity, diffusivity and chemical potential, etc.) as well as external processing parameters determined by the sintering conditions (such as temperature, heating and cooling rate, pressure, etc.). Sintering is generally an irreversible process, which is driven by interfacial energy minimization. After sintering, the initial particle compact (i.e., green body) becomes a dense bulk material, which is ready to be formed into various engineering parts.

Due to the its important role in material research and industry, theorists have been trying to formulate the applicable mathematical descriptions for solid-state sintering several decades ago, and the earliest work can be dated back in the 1940s.

The early theoretical models were mainly focused on individual mechanisms during different stages of sintering, including the initial bonding stage, intermediate shrinking stage and final sintering stage[63, 64, 65, 66]. Later on, more sophisticated models were developed, which used less simplifications and incorporated multiple physical mechanisms simultaneously[67, 68, 69, 70, 71, 72].

The final density, controlled by the sintering conditions and physical and chemical properties of material, is a key property for sintered materials, since porosity has a strong influence on subsequent processing and the mechanical properties of the final product[73]. A general model of densification during sintering, taking into account both grain boundary and volume diffusion[74], is established by Rusin et al., which is expressed as:

$$\frac{d\rho}{\rho dt} = \frac{3\gamma\Omega_a}{k_B T}[\frac{\delta D_b \Gamma_b}{G^4} + \frac{D_v \Gamma_v}{G^3}] \tag{4.1}$$

where ρ is density, γ is specific surface energy, Ω_a is atomic volume, G is the mean grain diameter, δ is the thickness of diffusion region, D_b and D_v are grain boundary diffusion coefficient and volume diffusion coefficient, and Γ_b and Γ_v are geometric factors for grain boundary and volume diffusion. Based on Eq.4.1, Su and Johnson [75] subsequently derived the following governing equation for sintering:

$$\Theta = \int \frac{1}{T} \exp(-\frac{Q_b}{RT}) dt \tag{4.2}$$

where Θ is a function of density. This is the so called master sintering curve (MSC). Under isothermal conditions, Eq.4.2 can be written as:

$$\Theta = \frac{t}{T} \exp(-\frac{Q_b}{RT}) \tag{4.3}$$

Recently, due to the rapid development modern computers, a significant amount of new efforts have been devoted in establishing general sintering models both analytically and numerically [76, 77, 78, 79, 80, 81]. In general, there are two categories of sintering models on mesoscale: deterministic and stochastic. The deterministic models are based on physical conservation laws (in the form of a set of partial different equations for mass and energy transfer) and employ standard numerical procedures (such as finite element method and finite difference method) to solve the equations for given boundary conditions[82, 83, 84]. For example, phase-field models have been used to investigate the detailed morphology evolution of two-particle system during sintering[85, 86].

On the other hand, in the stochastic models, the microstructure evolution during sintering is considered to be driven by the minimization of one or several predefined energy functionals, and is simulated using Monte Carlo methods (or coupled with finite element method)[87, 88, 89, 90, 91]. For example, Braginsky et al. successfully reproduced densification and grain growth by simulating the formation, diffusion and annihilation of vacancies[92]. Bjørk et al. explored the effect of particle size distributions on microstructural evolution during sintering using a similar Monte Carlo simulation[93]. Veena Tikare et al. use Potts model to study the microstructural evolution during solid state sintering of a complex 3D powder compact, which is in excellent agreement with 3D micro-tomographic images obtained from synchrotron radiation of Cu-powder compact[94].

Although successful in many aspects, most of the existing mesoscale numerical sintering simulations do not explicitly model the densification as a result of system-wide mass transport due to sintering stress. Here, we present a novel kinetic Monte Carlo model that models the densification process by iteratively applying effective particle displacements based on analytically derived heterogeneous densification rate,

grain boundary migration and interfacial energy minimization, which mimics to mass transport process. We also introduce an efficient two-step iterative interfacial energy minimization procedure with a "penalty energy" defined based on geometrical constraints for free-surface energy minimization. We prove that our model can accurately capture the diffusion-induced evolution of particle morphology, including neck formation and growth, as well as the overall densification behavior. The computationally obtained density evolution curves for both 2D and 3D sintering simulation are found in excellent agreement with the corresponding experimental master sintering curves. In addition, our model can be utilized to control a variety of structural and physical properties of the sintered materials by modifying corresponding simulation parameters. Combined with DEM simulation, which can be used to generate different packing configurations in terms of particle size distributions and particle shapes, it is possible to investigate the effect of powder precursor on microstructure evolution during solid-state sintering purely *in silico*.

4.2 Driving Force and Sintering Dynamics

4.2.1 Driving force in sintering: Interfacial energy minimization

In a typical sintering process, the microstructure evolution and densification result from the tendency of the system to minimize its total interfacial energy. For a sintering system under isothermal and isobaric conditions, the total energy includes several parts and can be expressed as[95]:

$$\phi_T = E_s + E_{coh} + PV \tag{4.4}$$

where $E_s = \gamma_{SV} A_{SV}$ is the total surface/interface energy, and γ_{SV} is specific surface/interface energy, A_{SV} is surface/interface area, E_{coh} is cohesive energy of particles, P is external pressure and V is the total volume.

For free solid state sintering (i.e., without externally applied pressures), the driving force is the reduction of interfacial energy of the material system, i.e., E_S in the Eq.4.4. The total reduction of interfacial energy can be expressed as:

$$\Delta(\gamma A) = \Delta\gamma A + \gamma \Delta A \tag{4.5}$$

Eq.4.5 indicates that, both the change of specific interfacial energy (or equivalently interfacial tension) and the change of interfacial area account for interfacial energy reduction. We note that although the main kinetic processes leading to interfacial energy reduction include surface diffusion (at the particle-pore interface) and grain boundary diffusion (at particle necks), other processes such as viscous flow and lattice diffusion can also lower the system's interfacial energy.

4.2.2 Discrete formulation of interfacial energy

In a discrete Monte Carlo model, the microstructure of the material during sintering is defined on a pixel-based grid. A popular form of surface/interface energy is given as follows[96]:

$$E_s = \frac{1}{2} \sum_{i}^{N} \sum_{j}^{m} \frac{J}{d_{ij}} [1 - \delta(q_i, q_j)] \tag{4.6}$$

where N is the total number of pixels included in the system, m is the number of nearest and next-nearest neighbor, d_{ij} is the distance between two pixels, $\delta(q_i, q_j)$ is

kronecker delta to exclude the sites of a same species and J is a parameter which is related to specific interfacial energy.

In our model, we introduce an additional "penalty energy" to further facilitate the minimization of the void-particle ("free") surface energy. Our formulation is motivated by the fact that the optimal shape of a single free particle is a perfect sphere (or circle in 2D). Thus, our "penalty" energy is defined as the difference between certain geometric moments (defined below) of a particle and the corresponding moments of the equivalent sphere (possessing the same volume of that particle). And the minimization of the penalty energy alone clearly tends to drive the particle to the associated spherical shape.

We now introduce the geometric moments used in the void-particle surface energy formulation. The geometry of a discrete object can be completely characterized via an indicator function:

$$I(\boldsymbol{x}) = \begin{cases} 0 & \text{if} \quad \boldsymbol{x} \text{ is occupided by material} \\ 1 & \text{if} \quad \boldsymbol{x} \text{ is occupided by void} \end{cases} \tag{4.7}$$

For a 3D object $f(x, y, z)$, the geometric moment with an order of $(p + q + r)$ is defiend as[97]:

$$m_{pqr} = \iiint x^p y^q z^r f(x, y, z) dx dy dz \tag{4.8}$$

For a discrete pixel-based object $I(x, y, z)$, its moment of $(i + j + k)$ can be calculated as summation:

$$m_{ijk} = \sum_x \sum_y \sum_z x^i y^j z^k I(x, y, z) \tag{4.9}$$

The geometric center of the image is defined as:

$$\bar{x} = \frac{m_{100}}{m_{000}}, \bar{y} = \frac{m_{010}}{m_{000}}, \bar{z} = \frac{m_{001}}{m_{000}} \tag{4.10}$$

The central moment (normalized form of geometric moment) with an order of $(p + q + r)$ is then defined as:

$$u_{pqr} = \sum_{x} \sum_{y} \sum_{z} (x - \bar{x})^p (y - \bar{y})^q (z - \bar{z})^r I(x, y, z) \tag{4.11}$$

Ghorbel et al.[98] have shown that for a general complex microstructure (or an image), the associated indicator function can be approximated as a summation of finite terms consisting of geometric moments with proper truncation. Therefore, the penalty energy for the void-particle surface energy minimization in our model is defined as:

$$E_{pn} = \sqrt{\sum_{p+q+r=0}^{p+q+r=n} (u_{pqr}(x_c, y_c, z_c) - u^0_{pqr}(x^0_c, y^0_c, z^0_c))^2} \tag{4.12}$$

where u_{pqr} and u^0_{pqr} are central geometric moments of object of interest and that of the equivalent sphere, (x_c, y_c, z_c) and (x^0_c, y^0_c, z^0_c) are centers of mass and n is the highest order used in the truncation.

4.2.3 Sintering stress

The sintering stress, which is originally defined for equilibrium state and is proportional to sintering rate (or shrinkage rate), has been widely used to characterize the total driving force [99, 100]. There are several definitions that can be used to calculate sintering stress [101]. Here, we employ a simple definition in which the sintering stress is considered as the variation of energy with respect to volume change:

$$S(t) = \frac{\delta E^*(t)}{\delta V^*(t)} = \frac{V_m \delta(\gamma_S A_S + \gamma_{gb} A_{gb} - E_0)}{E_0 \delta V} \tag{4.13}$$

where t is sintering time, E^* and V^* are normalized interfacial energy and volume respectively given by

$$E^* = \frac{\gamma_S A_S + \gamma_{gb} A_{gb} - E_0}{E_0} \tag{4.14}$$

$$V^* = \frac{V}{V_m} \tag{4.15}$$

where γ_s and γ_{gb} are specific energy of surface and grain boundary, A_s and A_{gb} are the values of surface and grain boundary areas, V_m is the total volume of all the particles, and E_0 is the initial interfacial energy. In our case, the Monte Carlo step can be naturally regarded as a measure of time, the values of E is calculated according to Eq.4.5. The curve of $S(t)$ vs. $V^*(t)$ is derived from calculating the slope of $E^*(t)$ vs. $V^*(t)$ plot.

4.2.4 Material deposition and densification rate

Using a first order approximation for the thickness deposition rate at grain boundary, Exner and Bross[102] calculated a parabolic stress distribution and the corresponding material transport along grain boundary during grain boundary diffusion. Their results showed that compressive stress occurs at central region of a neck and tensile stress occurs at neck surface. For a symmetric neck, the stress distribution is described by the following equation:

$$\delta(x) = \frac{\gamma}{R}\left(\frac{6}{g^3}(g - 2R)(x^2 - xg) + 1\right) \tag{4.16}$$

and the associated rate of material deposition at grain boundary is described by:

$$\frac{ld}{dt} = \frac{D_G b\Omega d^2\sigma}{kTdx^2} = \frac{12D_G b\Omega\gamma}{kTRg^3}(g-2R) \tag{4.17}$$

where $R = R_1 = R_2$ are the radii of neck surface curvature at the left and the right hand side, g is the length of the grain boundary, x is the distance from left neck surface along the grain boundary, dl is the height of material deposition at the grain boundary, γ is surface tension, D_G is the grain boundary diffusivity, b is the grain boundary width, and Ω is an intermediate coefficient, see Fig.27 for a schematic illustration. We note that Eq.4.16 and 4.17 were derived for a two-particle sintering system assuming that $\frac{dl}{dt}$ is linearly related to x.

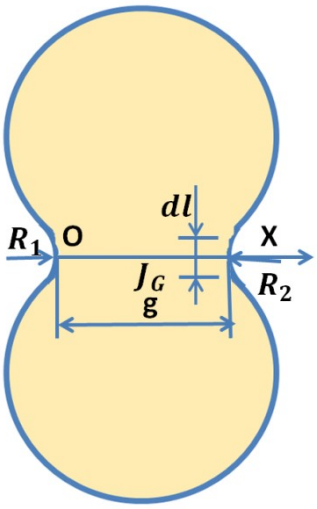

Figure 27: A schematic illustration of two-particle sintering configuration. R_1 and R_2 are the radii of neck surface curvature at the left and the right hand side, g is the length of the grain boundary, x is the distance from left along the grain boundary, dl is the height of material deposition at the grain boundary, J_G is atomic flux in grain boundary.

In a many-particle system, the material deposition due to grain boundary diffusion

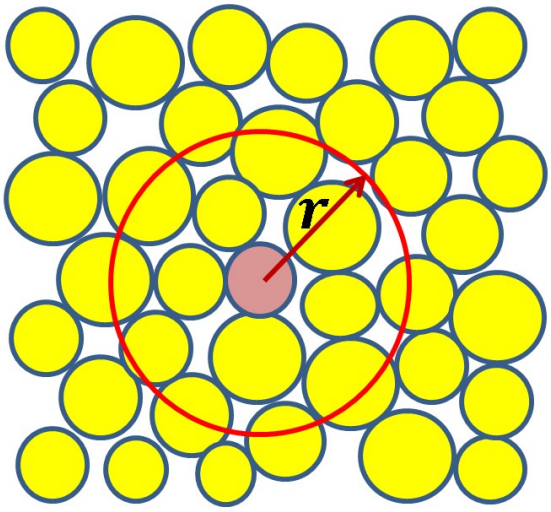

Figure 28: Schematic illustration of a spherical sub-region with radius r in the sintering material. The material deposition at the grain boundary leads to overall densification of the materials, i.e., shrinkage of radius r. As shown in the text, the densification (shrinkage) rate at the boundary of this sub-region is linearly proportion to r.

results in the overall densification of the system. In particular, consider that in the sintering system, the average coordination number for a particle is Z, the average grain boundary length at time t is a, the particle number density $\rho = N/V$, then the total length of the grain boundary $L(r)$ within a spherical region of radius r (see Fig.28 for schematic illustration) is given by

$$L(r) = \pi r^2 \rho \frac{Z}{2} a \tag{4.18}$$

During time interval dt, the void space taken up by material deposition is then given by

$$dV(h,t) = L(r) dl \tag{4.19}$$

We note that in general $L(r)$ is also a function of time due to the fact that a is

time-dependent. However, in our model, we assume that a is an average value whose rate of change is much smaller compared to the deposition rate and thus, can be approximately considered as a constant. According to mass conservation, we can compute the average densification rate $u_t(r)$ (the average shrinkage rate along the radial direction) at the boundary of the spherical region due to material deposition as follows:

$$u_t(r) = \frac{-dV/dt}{2\pi r} = -\frac{3D_G b\Omega\gamma\rho aZr}{kTRg^3}(g - 2R) = -C(T)r \tag{4.20}$$

From Eq.4.20, it is clear that under isothermal conditions, the densification rate at a point in the sintering system is linearly proportional to its distance r from the reference center. This result suggests that the overall densification of the system can be modeled by effective particle displacement, coupled with interfacial energy minimization steps, which we will discuss in detail in the subsequent section.

4.3 Algorithmic Details

4.3.1 Interfacial energy minimization for two-particle system

We first present our Kinetic Monte Carlo (KMC)[103] algorithm for a two-particle sintering system, in order to verify the incorporation of the penalty energy for free surface minimization. In particular, our algorithm includes two fundamental repeating processes: (i) overall interfacial energy minimization using Eq.4.6, and (ii) separate free surface energy minimization (using the penalty energy) and grain boundary energy minimization, which we describe in detail below.

Firstly, we use simulated annealing to minimize the total interfacial energy defined

by Eq.4.6, including both free surface and grain boundary. Many previous studies stop at this step when doing interfacial energy minimization. However, as we will show in following sections, this step alone is not sufficient to lead to densification in this two-particle sintering system. The interfacial energy minimization is implemented by randomly choosing a surface pixel or grain boundary pixel and exchanging its value with one of its neighbors which are of different pixel values from the selected pixel. Then the corresponding energy change is calculated according to Eq.4.6, and this trial exchange is accepted based on the Metropolis rule, i.e.,

$$p_{acc(old \to new)} = \begin{cases} e^{-\frac{E_{new}-E_{old}}{T}} & \text{if} \quad E_{new} \geq E_{old} \\ 1 & \text{if} \quad E_{new} < E_{old} \end{cases} \tag{4.21}$$

where T is an annealing parameter that is gradually decreased during the simulation and does not related to the actual temperature of the sintering system. We note that the diffusion coefficients of free surface diffusion and grain boundary diffusion are significantly different, i.e., grain boundaries are usually considered as perfect source and sink of atoms so that no energy is required for atom attaching and detaching. To take into account this, during the interfacial energy minimization, the specific interfacial energy parameter J in Eq.4.6 for grain boundary pixel is set to be 0.5, while that for free surface pixel is set to be 1.0.

Secondly, we perform energy minimization on free surface and grain boundary separately for each particle. For free surface energy minimization, the grain boundary is kept stationary and the penalty energy is used, i.e., the free surface of a particle is evolved (by randomly exchanging free surface pixels) using simulated annealing to minimize the difference of its geometric moment from that of the equivalent sphere, without moving the pixels at grain boundary. For the subsequent grain boundary

energy minimization, the surface pixels are kept fixed and the grain boundary pixels are randomly exchanged and the associated energy is computed using Eq.4.6 and minimized using simulated annealing. The same parameters are used for all simulated annealing simulations, which include an initial temperature of 0.1, a cooling rate of 0.99 and an initial acceptance rate of 0.3. The aforementioned two steps (overall interfacial energy minimization and separate free surface/grain boundary energy minimization) are repeated to drive the system to global energy minimum which is very difficult to achieve by using single interfacial minimization for Eq.4.6 alone.

4.3.2 Effective particle displacement for densification in many-body sintering

For a many-body sintering system, the numerical interfacial energy minimization procedure alone is not sufficient to result in densification. A widely-used densification scheme (i.e., the vacancy annihilation model)[92] is to exchange internal void pixel with a material pixel on the external free surface of the sintering system. Here, we present a novel procedure for densification by applying effective particle displacements. Following Exner and Bross's work on sintering stress induced material deposition[102], we have derived an analytical expression of densification (displacement) rate at any position within the sintering system, which is linearly proportional to the distance of that position to a reference center, see Eq.4.20. In our simulation, we set $C(T) = 0.1$, in order to match the experimental sintering master curve. The unit of distance r is in pixel and dt is taken to be the time for a single simulation cycle.

Our many-body sintering simulation proceeds in a very similar way as the two-body sintering, except that for the many-body system we explicitly incorporate effective particle displacement due to system-wide mass transport driven by grain boundary

diffusion, which is necessary for densification. The algorithm which includes two repeating steps is described as follows:

Firstly, we use simulated annealing method to minimize the total interfacial energy of the system (including both free surface energy and grain boundary energy), following the same procedures used for the two-particle system (i.e., the iterative two-step energy minimization). The parameters used include an initial temperature of 0.1, a cooling rate of 0.99 and an initial acceptance rate of 0.3.

Secondly, we apply the effective particle displacement according to Eq.4.20 to achieve densification of the sintering system. Specifically, we first obtain the position of center of mass (COM) of particle i, i.e., $\boldsymbol{x}_i$, and its effective displacement $\boldsymbol{u}_i(r)$ calculated based on the densification rate given by Eq.4.20, where r is the distance of the COM to the reference line in the system. Then, we apply simulated annealing by randomly moving the free surface pixels of the particle to minimize interfacial energy as well as difference between the geometric moment of that particle and that of the equivalent sphere centered at $(\boldsymbol{x}_i + \boldsymbol{u}_i)$, i.e., the "penalty energy". Finally, the migration of grain boundary between two contacting particle i and j is considered when the magnitude of $(\boldsymbol{u}_i + \boldsymbol{u}_j)/2$ is greater than one pixel length. This is achieved by first depositing the grain boundary pixels of the particle closer to the reference center to the surface of that particle, and then randomly moving the surface pixels of the other particle to fill the vacant sites. We note that the aforementioned procedures mimic the sintering stress induced mass transfer process that result in densification of the system. These two steps (interfacial energy minimization and effective particle displacement) are repeated until the sintering system is fully densified or a prescribed density value is achieved.

4.4 Case 1: Modeling two-particle sintering behavior

In this section, we use the algorithm described in previous sections to investigate the densification behavior of a two-particle system during sintering and quantitatively compare our simulation result with experimentally obtained master sintering curve (MSC).

In particular, we consider two congruent spherical particles with a radius of 30 pixels. Initially, the two spherical particles are just touching one another with their centers separated by a distance of 60 pixels. Different values are assigned to the pixels belonging to different particles for the convenience of calculating surface energy, although the particles are made of the same material. In the beginning of the simulation, the total interfacial energy and six second order central moments $(u_{xx}, u_{yy}, u_{zz}, u_{xy}, u_{yz}, u_{xz})$ are computed[104]. Then the two-step iterative interfacial energy minimization procedure will be applied.. For the purpose of comparison, we also perform standard Monte Carlo simulation to minimize the interfacial energy alone, without the additional separate surface-energy/ grain-boundary energy minimization step.

Fig.29 shows microstructure evolution as a result of two-step energy minimization, while Fig.30 shows microstructure evolution via standard MC energy minimization. It is obvious that the final microstructure in Fig.29 possesses a more compact morphology than that in Fig.30. This has been quantitatively verified by comparing the particle center-center distance after each sintering step. To further quantitatively validate our sintering model, we obtain the relative density as a function of Monte Carlo step (see Fig.31) and compare it with the mater sintering curve, in which the relative density is calculated according to the following equation:

$$\rho = \frac{1}{(d/L)^3} = \frac{L^3}{d^3} \tag{4.22}$$

where d is the instant distance between center of mass of the particles, while L is the initial separation. From Fig.31, it can be seen that our simulated curve is in excellent agreement with the Master Sintering Curve[75] under isothermal conditions, where the density increases rapidly in the initial state of the sintering and slows down when approaching the maximum density. On the other hand, in the case of standard MC energy minimization, the density fluctuates and no significant overall densification is seen, as shown in Fig.32. This indicates that interfacial energy minimization alone via standard MC simulation is not sufficient to induce densification and lead to the global minimum energy state.

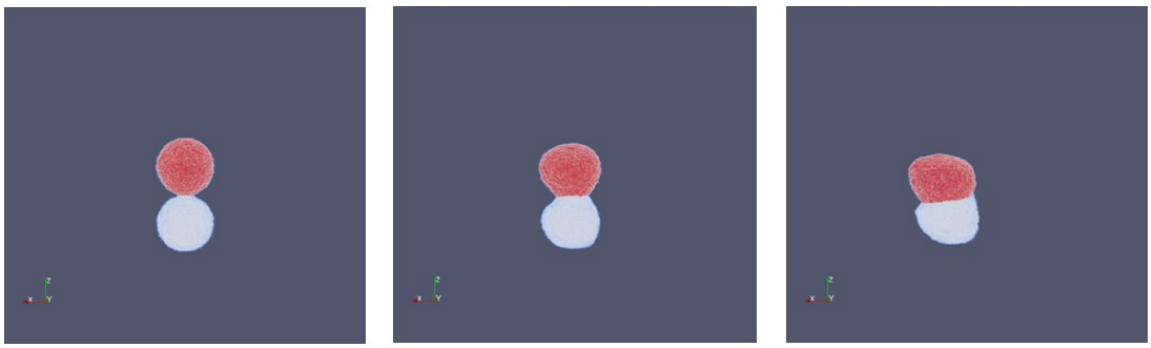

Figure 29: Microstructure evolution of a 3D two-particle sintering system as simulated via the two-step energy minimization method.

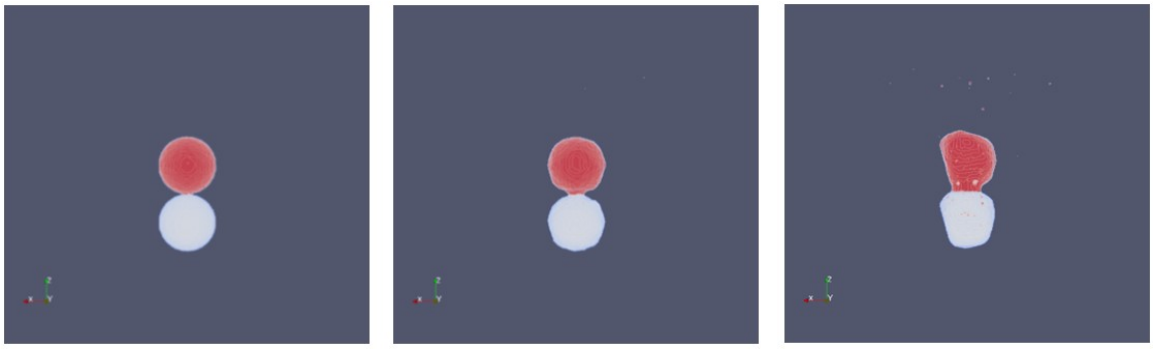

Figure 30: Microstructure evolution of a 3D two-particle sintering system as simulated via the standard Monte Carlo energy minimization method.

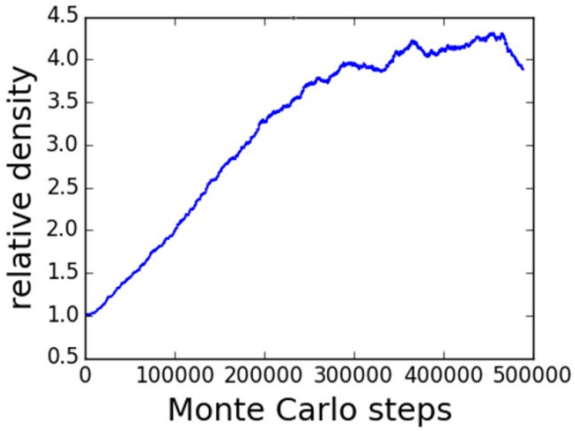

Figure 31: Density evolution for the 3D two-particle sintering system as simulated via the two-step energy minimization method.

4.5 Case 2: Modeling many-particle sintering in two dimension

After the two-particle sintering model validation, we now employ our algorithm to simulate the sintering behavior of a many-body system in two dimensions, which models the densification via iterative effective particle displacement (as a result of sintering stress induced mass transport) and two-step interfacial energy minimization. In addition, we also simulate a sintering system that is driven by interfacial energy minimization alone for the purpose of comparison.

The initial configurations of both cases are identical, whih consist of 100 2D

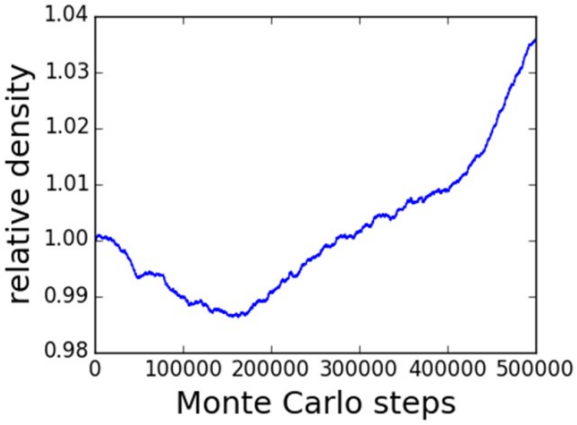

Figure 32: Density evolution for the 3D two-particle sintering system as simulated via the standard Monte Carlo energy minimization method.

spherical particles with a normal distribution of their radii. It is generated by uniformly growing an initially dilute sphere packing to a near-jamming configuration using DEM simulation. The packing configuration for sintering simulation is then discretized on a square grid with 600 by 600 pixels, which results in a mean radius of 15 pixels and radius standard deviation of 5 pixels. Hereafter, all the distances reported are measured in the length of pixel. Coarsening will be considered at later stages of sintering, which takes the role of hindering further densification and has significant effects on the mechanical properties of sintered materials. In this simulation scheme, we employ the Potts model to continuously change the value of interfacial pixels and constantly modify the shape of interface in search of lowest energy state during the later stages of sintering. Specifically, interfacial pixels are first tracked and randomly picked to calculate the surface energy associated with this pixel; then its value is changed to be the same as its neighboring pixel with the largest frequency of occurrence. If the change decreases the total interfacial energy, then it's accepted; if it increases the surface energy, it is accepted at a predefined rate of 0.0001, which will be referred as coarsening rate parameter.

Fig.33 shows the microstructure evolution of the sintering system simulated using effective particle displacement. Note that due to the application of periodic boundary condition along the vertical direction (to simulate an infinite large size thin layer), no shrinkage can be observed in this direction. This also implies that our model sintering system possesses a reference central line, and the densification rate at any point in the system is proportional to the distance of that point to the central line. The sintering density vs. Monte Carlo steps is plotted and shown in Fig.34. The left panel shows the total density evolution, which is in excellent agreement with the corresponding MSC. The right panel shows the density distribution along horizontal direction at selected stages. We can clearly see that densification takes place as sintering proceeds. At later stage, density along y direction becomes uniform, suggesting a fully densified configuration. The sintering stress due to interfacial energy reduction is also computed at different stages, and plotted with respect to the specific volume. The fitted curve is obtained based on a third order polynomial using least square fitting method. In Fig.35, the left panel shows interfacial energy, while the right shows sintering stress.

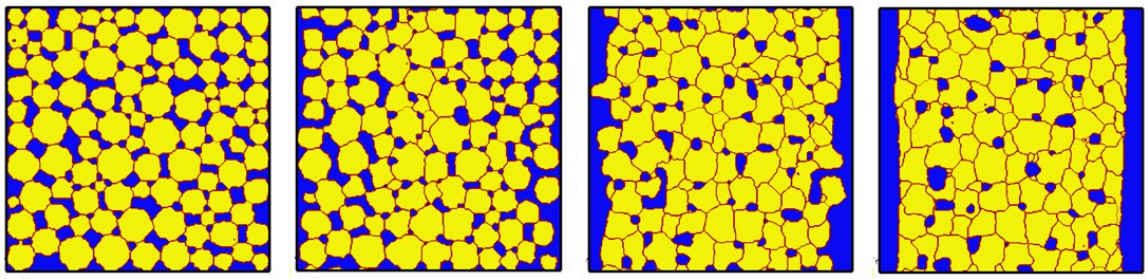

Figure 33: Microstructure evolution at Monte Carlo stages 1, 50, 300, and 900 (from left to right panels) for a 2D sintering system simulated by considering mass transport effects.

Fig.36 shows the microstructure evolution of a system driven by standard MC in-

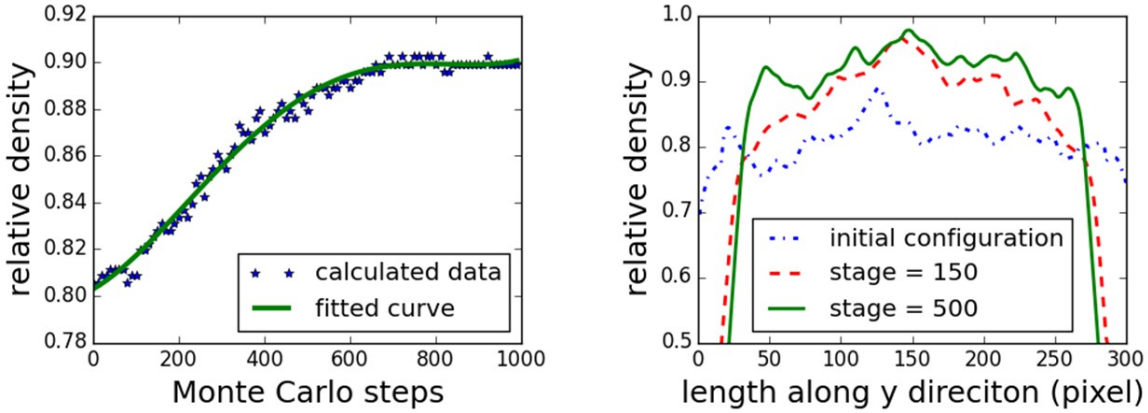

Figure 34: Left panel: Relative density evolution as a function of Monte Carlo steps for the 2D sintering system simulated by considering mass transport effects. Right panel: Relative density distribution along y direction (the non-periodic direction) at MC stages 0, 150, and 500.

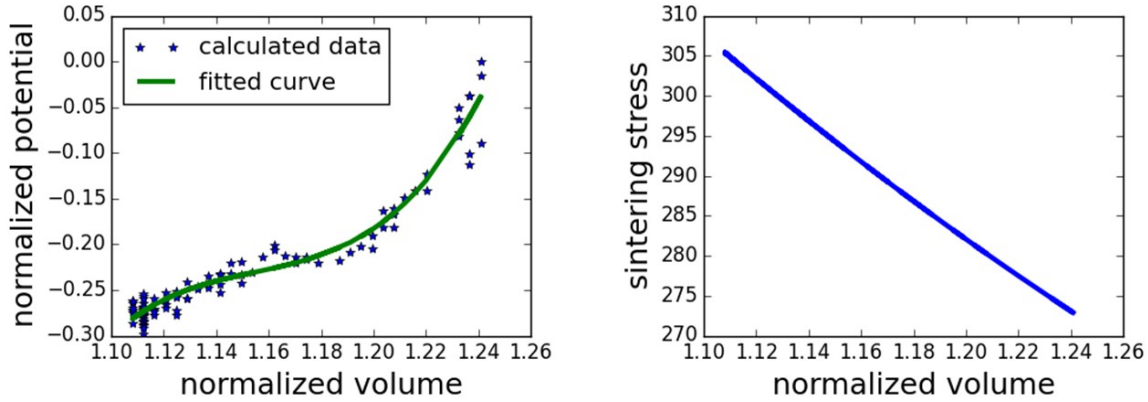

Figure 35: Left panel: Normalized interfacial potential with respect to normalized volume for the 2D sintering system simulated by considering mass transport effects. Right panel: Sintering stress with respect to normalized volume.

terfacial minimization. As a comparison, no significant densification could be observed just like the two-particle sintering case using standard MC energy minimization. This can be quantitatively verified via the density evolution along the horizontal direction, as shown in Fig.37, which remains almost unchanged as simulation proceeds. However, we note that although the density does not increase appreciably, initially prolonged

pores tend to be more isotropic, leading to smaller curvatures and thus reducing interfacial energy.

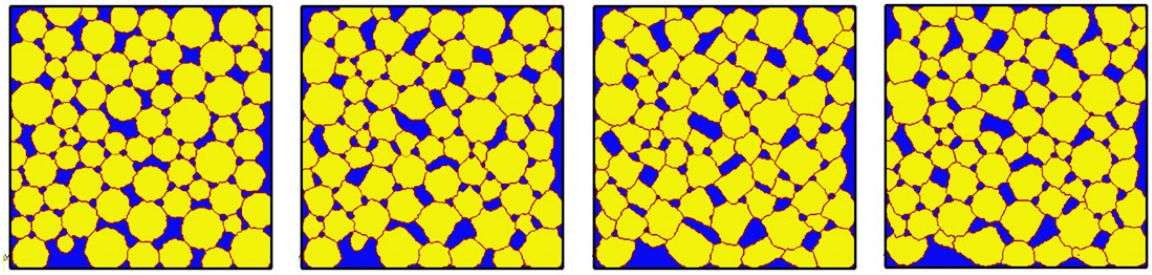

Figure 36: Microstructure evolution at Monte Carlo stages 1, 50, 300, and 900 (from left to right panels) for a 2D powder compact simulated by applying MC interfacial energy minimization alone.

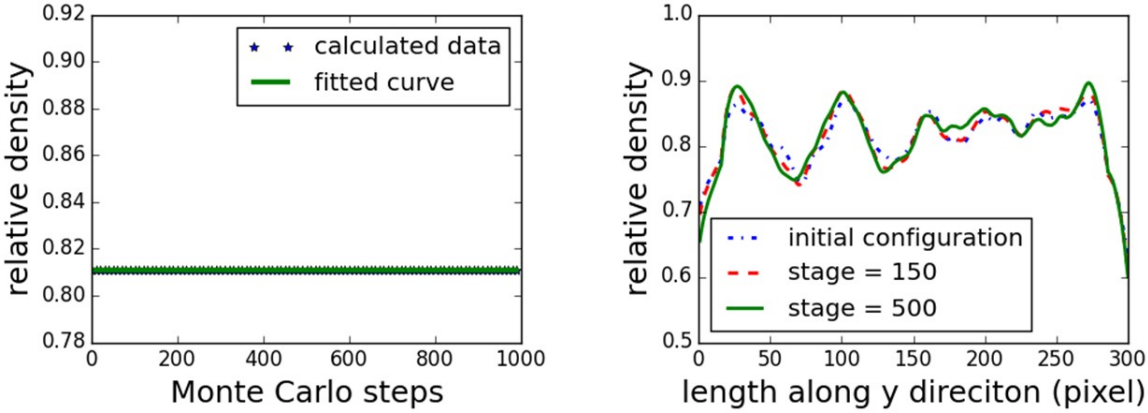

Figure 37: Left panel: Normalized interfacial potential with respect to normalized volume for the 2D sintering system simulated by applying MC interfacial energy minimization alone. Right panel: Sintering stress with respect to normalized volume.

4.6 conclusion

Microstructure control is an important subject in solid-state sintering and plays a crucial role in determining material properties, such as density, strength, toughness,

etc. Different from existing sintering simulations, most of which are driven by surface energy minimization only and the densification of them are realized by either dilating the particles or using the vacancy annihilation method, we have developed a novel combinative modeling scheme of discrete element method (DEM) and kinetic Monte Carlo method (kMCM) to model morphology evolution and densification during free sintering simultaneously. Specifically, we have derived analytically a heterogeneous densification rate of the sintering system by considering sintering stress induced mass transport. Our model is proved to be able to accurately capture the diffusion-induced evolution of particle morphology, including neck formation, growth, and coarsening, as well as realistically reproduce the overall densification process. The computationally obtained density evolution curves for both two-particle sintering and many-particle sintering are found in excellent agreement with the corresponding experimentally summarized master sintering curve. Our model can be utilized to guide the control of a variety of structural and physical properties of the sintered materials, such as the pore size and final material density.

Additionally, our model can be easily generalized to incorporate more complex processing conditions, such as changing sintering temperature field or externally applied pressure, which provides the potential to systematically investigate the effects of material types, initial powder packing configurations and different sintering conditions on microstructure evolution during solid-state sintering. Although most of the simulations demonstrated here are performed on 2D, the corresponding 3D microstructure can be immediately obtained using stochastic reconstruction algorithm introduced in chapter 3.

The content in this chapter can be found in Modeling and Simulation in Materials Science and Engineering 24, 085003 (2016).

Chapter 5

MODELING PHASE TRANSITION OF SELECTIVE LASER SINTERING OF TITANIUM ALLOY

5.1 Background

In previous chapter, we presented a combinative model for solid state sintering, where DEM served to generate powder packing and kinetic Monte Carlo is engaged to simulate microstructure evolution. In this chapter, we are going to introduce another cominative model for selective laser sintering (SLS), where particles not only interconnect and coarsen but also undergo phase transition from one solid state to another.

As a typical rapid additive manufacturing technology, selective laser sintering (SLS) has been extensively used in metal processing, product design, biomedical applications, and energy and sustainability applications and so on[105]. With the help of computer-aided design (CAD) models, materials can be developed into complicated geometries efficiently to satisfy various application situations, including design testing, find functional parts manufacturing, etc.[106]. Other advantages, such as low time costs, high material utilization rate, wide range support of commercial powders, are also being attractive factors to modern industry, which makes it popular in just two decades since its invention[107].

To establish a model for laser sintering, countless efforts have been made in experiments, fundamental theories, as well as computer simulation. In particular, numerical simulation of laser sintering has gained significant progresses, however,

inventing a thorough modeling technique to include powder packing, heat transfer, melting, phase transition and finally solidification is still a challenging task. In this chapter, we are introducing a combinative model of FEM and cellular automata for the simulation of selective laser sintering, where melting, phase transition and microstructure evolution will be simulated by first modeling temperature field evolution using finite element analysis and then modeling nucleation and growth using cellular automata.

The material we are going to use for laser sintering simulation is Ti_6Al_4V, which has been a widely used high performance structural material due to its lower density, superior mechanical properties, high chemical corrosion resistance, as well as easier to for working and processing, compared to conventional metallic materials[108]. For selective laser sintering of Ti_6Al_4V, the microstructure evolution during $\beta \rightarrow \alpha$ phase transition is a key factor that affects the properties of final product, which is dependent on the processing parameters, such as the laser power, scanning speed, and scanning pattern, and so forth. These processing parameters are directly reflected by the temperature filed evolution as laser spot moves. We will incorporate these processing conditions into a standard finite element analysis model to solve the transient temperature field.

The microstructure evolution during phase transition will be simulated via a cellular automata (CA) model. Cellular Automata (CA) is first developed by Stanisław Ulam and John von Neumann for Los Alamos National Lab in 1940s. One of the very first applications of CA is studying the growth of crystals[109]. CA models have been constantly gaining popularity as discrete dynamical system simulator, vehicles for studying pattern formation and complexity, and novel devices modelling fundamental physics. Though being relaxed commonly, in general four basic characters define a CA:

discrete n-dimensional lattice of cells, discrete states for each cell, local interactions, and discrete dynamics. Because of its efficiency and phenomenologically soundness, CA has been extensively explored in material science research[110, 111, 112, 113, 114, 115].

5.2 FEM model on temperature field evolution during laser sintering

Past decades have seen a lot of researches conducted to calculate temperature field during laser sintering, both analytically or computationally. For example, a pragmatic engineering model using an enthalpy formulation incorporating the effects of shrinkage and laser penetration is developed to investigate the laser melting (SLM) process [116]; a process map of pulsed selective laser sintering is generated by conducting numerical simulation of heat equations as well as experiments [117]; finite Element Method (FEM) is used to study the thermal cycles and temperature field by allowing element birth and death [118], etc.

Despite the fact that extensive work have been done to study the laser induced temperature field and some properties of the sintered body, it is still not clear about how the microstructure evolves due to the agitation of scanning laser and what kind of properties will be produced if certain microstructure evolution takes place. In the following sections, we will introduce the FEM simulation to calculate the transient temperature field at arbitrary time as laser beam moves. The temperature field obtained can be used to direct the evolution of Ti_6Al_4V microstructure in a robust cellular automata model, which will be discussed later.

5.2.1 FEM model details

The entire simulation domain will be restricted to $5mm$ by $5mm$ by $2mm$ block. When generating mesh, another bock of $1mm$ by $3mm$ by $0.5mm$ which is defined as laser spot affecting area, is selected for finer element size with an average of $0.025mm$, while the rest is meshed with coarser element with an average size of $0.1mm$, see Fig.38(a). We have tried different mesh sizes on the laser affecting area, and it turns out that $0.025mm$ is right close the critical size that guarantees stability of the solution while maintain descent efficiency.

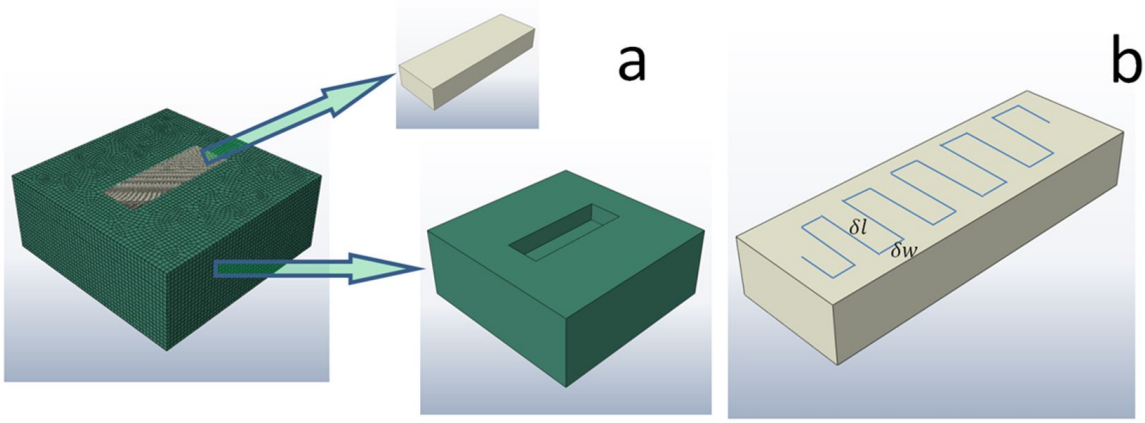

Figure 38: (a) geometry and mesh of FEM simulation domain: the overall size is $5mm$ by $5mm$ by $2mm$ meshed with $0.1mm$ elements, the laser spot affecting area is $1mm$ by $3mm$ by $0.5mm$ meshed with $0.025mm$ elements. (b)the scanning path, $\delta l = 0.6mm$,$\delta w = 0.2mm$.

The laser spot moves in a zigzag fashion and is restricted to the fine meshed area. The process parameters utilized in this model are $120W$ for laser power, $100\mu m$ for laser spot radius, $200mm/s$ for laser scanning speed and the scanning pattern is shown on Fig.38(b).

The thermodynamic properties of Ti_6Al_4V powders for laser sintering vary ac-

cording to different fabricating approaches and measuring states. Here we use the temperature dependent density, thermal conductivity and specific heat as provided in [119], which are replicated here in Fig.39(a)(b)(c).

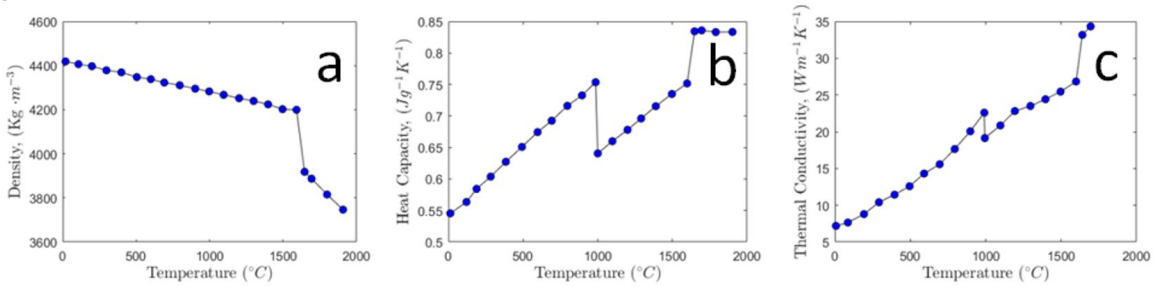

Figure 39: Temperature dependent thermodynamic properties of Ti_6Al_4V. (a) density; (b) heat capacity; (c) thermal conductivity.

The heat flux of laser beam is commonly modeled as a Gaussian distribution, which is given as:

$$Q(\boldsymbol{r}) = \frac{2AP}{\pi r_0^2} e^{-2\boldsymbol{r}/r_0^2} \tag{5.1}$$

where P is laser power, r_0 is laser spot radius, $\boldsymbol{r}$ is an arbitrary position in the incident surface and A is the absorption coefficient of the material, the value of which is chosen to be 0.3, as the intrinsic absorptance of Ti with Nd:YAG wavelength $1.06\mu m$, following ref.[117].

The initial temperature of the entire simulation body is $300K$, and the lateral and bottom sides are fixed at $300K$ during sintering, under the assumption that these boundaries are far enough from the laser spot. The additive surface is defined as heat convection and radiation boundary, with an average heat transfer coefficient $300W/(m^2K)$ and emissivity 0.5.

5.2.2 FEM simulation results

The contour plot of temperature field at $0.01s$ is demonstrated on Fig.40, both with an overview of the whole simulation domain (a) and an inset of the laser affected region (b), while Fig.41 shows the corresponding heat flux. From the contour plots, we find the maximum temperature can reach as high as $3500K$, and there exists very large temperature gradient near laser spot. This obtained temperature field will be used for cellular automata simulation of microstructure evolution of this sintering process.

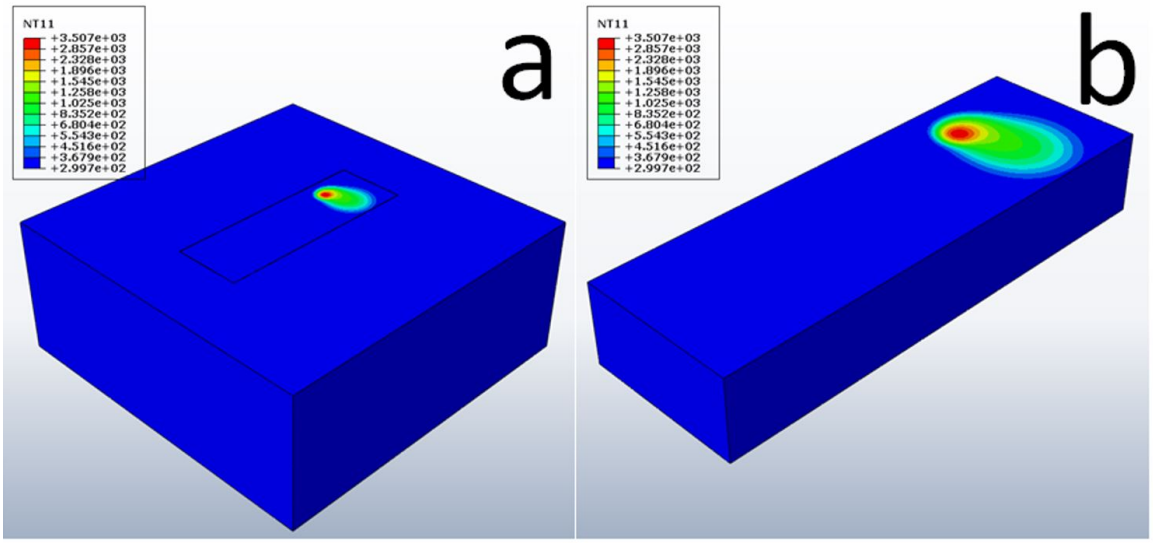

Figure 40: Contour plot of temperature field at $0.01s$. Maximum temperature is $3500K$, (a)whole simulation domain, (b)laser spot affecting domain.

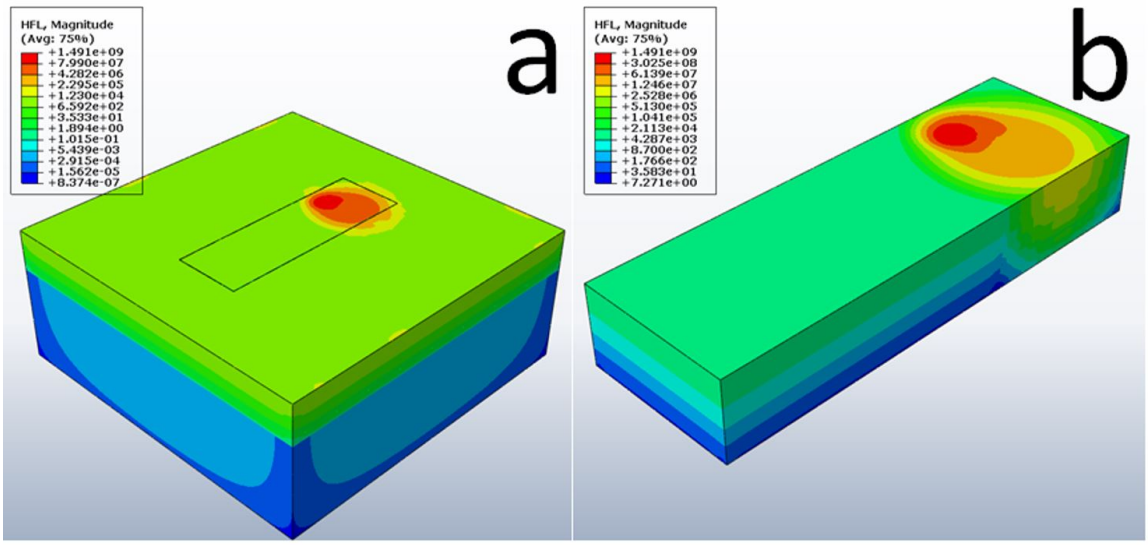

Figure 41: Contour plot of magnitude of heat flux filed at $0.01s$. (a)whole simulation domain, (b)laser spot affecting domain.

5.3 Theoretical background for CA modeling of phase transition

5.3.1 crystalline structure transition

For pure titanium, body centered cubic (BCC) structure is the stable phase at high temperature, referred as β phase. Upon cooling, BCC structure transforms into a modified ideally hexagonal close packed structure, which is the low temperature stable phase, known as α phase. This transition takes place at 882±2°C. During this $\beta \rightarrow \alpha$ transition, the densest packed {110} plane in β transforms to the {0001} plane of α, satisfying the follow orientation relation[120]:

$$\begin{cases} \{0001\}_\alpha \parallel \{110\}_\beta \\ \langle 1120 \rangle_\alpha \parallel \langle 111 \rangle_\beta \end{cases} \tag{5.2}$$

Due to crystallographic symmetries, there could be 12 possible α orientations precipitating from a particular β parent grain following the orientation relationships[121].

With different cooling rate, the microstructure of transformed α phase could be significantly distinct. Generally speaking, fine structure such as needle-like α phase (referred to as acicular phase) is produced at high cooling rate, while plate shape is formed at slow cooling rate. At intermediate cooling rate, the well-known Widmanstätten pattern is developed, within which α plates grow from grain boundaries of precursor β phase and are separated by high-vanadium-concentration β remainings. The radial spread of α plates is along the {110}plane of bcc structure. It is also worth to mention that when cooling rate is high enough the growth front of each lamellar packets can be potential nucleation sites as well, and Martensitic transformation occurs at such high cooling rate, characterized by a very fine basket-weave structure with needle-like α grains due to diffusionless nucleation. Other microstructure, such as equiaxed α grain, is a result of recrystallization.

5.3.2 Kinetics of transition

The kinetics of the $\beta \rightarrow \alpha$ transformation under isothermal condition can be characterized by Johnson-Mehl-Avrami theory (JMA):

$$f = 1 - \exp(-kt^n) \tag{5.3}$$

f is the α phase volume fraction, k is a constant, n is the Averami index associated with nucleation and growth mechanisms. It is assumed that nucleation frequency is constant and nuclei are spatially randomly formed.

The JMA equation under continuous cooling is commonly expressed as[122]:

$$f = 1 - \exp(-\theta^n) = 1 - \exp(-(k_0 \exp \int (\frac{-Q}{RT})dt)^n) \tag{5.4}$$

where k_0 is a constant, Q is the overall activation energy.

In practice, the kinetics of phase transformation during continuous cooling can be numerically obtained by discretizing the JMA equation into a sum of small consecutive isothermal steps using fictitious time:

$$\begin{aligned} f_i &= 1 - \exp(-k_i(t_i + \Delta t)^{n_i}) \\ t_i &= \sqrt[n_i]{\frac{-\ln(1-f_i)}{k_i}} \end{aligned} \tag{5.5}$$

for simplicity, n_i can be regarded as constant, $n = 1.13$ for Ti_6Al_4V empirically. Reaction rate k, on the other hand, varies significantly with temperature demonstrated in Fig.42 as a function of temperature for Ti_6Al_4V, which is replicated from reference[123].

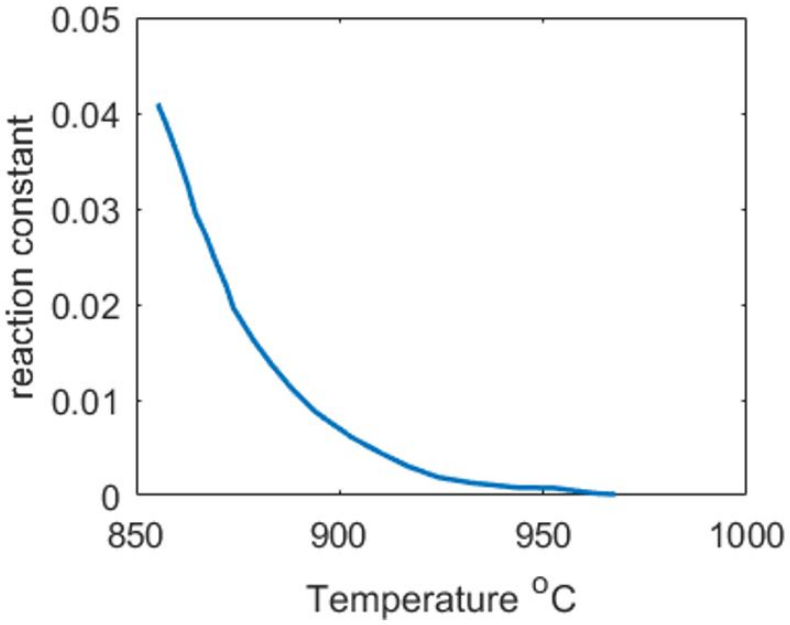

Figure 42: Calculated reaction constant for Ti_6Al_4V in JMA equation.

5.3.3 Formulation of nucleation and growth

Assuming an intermediate cooling rate, all the α grains nucleate at the grain boundary of beta phase, the rate of which is influenced by the element concentration field and temperature field. The growth rate or the α/β interface migration rate is dependent on the intrinsic mobility of impurity atoms and diffusion energy barrier. The mathematical formulation of nucleation is similar to that of a common solidification process[124]:

$$\begin{aligned} N &= \frac{N_v k_b T}{\hbar} \exp(\frac{-\Delta G_m + \Delta G_c^*}{k_b T}) \\ \Delta G_c^* &= \frac{16\pi\gamma_{\alpha\beta}^3}{3\Delta g^2} S(\theta) = \frac{16\pi}{3} \frac{\gamma_{\alpha\beta}^3 T_c^2}{L_v^2} \frac{1}{(\Delta T)^2} S(\theta) \\ S(\theta) &= \frac{1}{2}(2+\cos(\theta))(1-\cos(\theta))^2,\ \Delta T = T_c - T \end{aligned} \tag{5.6}$$

where N_v is the potential nucleation sites per unit volume, ΔG_c^* is the nucleation barrier, ΔG_m is the activation energy of atomic migration across the interface, $\gamma_{\alpha\beta}$ is the free interface energy of α/β phase boundary, Δg is the volumetric free energy difference between α and β phase or the driving force, T_c is the transition temperature, L_v is the latent heat of phase transition, θ is the wetting angle, and ΔT is undercooling which is the difference between transition temperature and current temperature.

Within the range of phase transition, as T decreases, ΔT increases, ΔG_c^* decreases, and the overall contribution of $\exp(\frac{-\Delta G_c^*}{k_b T})$ increases, meanwhile, $\exp(\frac{-\Delta G_m}{k_b T})$ decreases.

Furthermore, through integration the total number of nuclei at a potential nucleation site at time t can be obtained as:

$$\begin{aligned} J(t) &= \int_{S_\beta}\int_{t_0}^{t} N dt dx = \int_{S_\beta}\int_{t_0}^{t} aT(t,x)\exp(\frac{-b}{T(t,x)})\exp(\frac{-c}{\Delta T(t,x)^2 T(t,x)^2}) dt dx \\ a &= \frac{N_v k_b}{\hbar}, b = \frac{\Delta G_m}{k_b}, c = \frac{16\pi}{3}\frac{\gamma_{\alpha\beta}^3 T_c^2}{L_v^2} S(\theta)\frac{1}{k_b} \end{aligned} \tag{5.7}$$

where S_β denotes the spatial integration domain of β grain boundaries, t_0 is the transformation starting time, a, b, c are treated as constants in CA simulation.

It has been found that the growth of α plate is mainly controlled by the diffusion of vanadium atoms during $\beta \rightarrow \alpha$ phase transformation of Ti_6Al_4V. Suppose the atomic mobility of vanadium is M, the Gibbs free energy difference between α and β phase is ΔG, the molar volume of α phase is V_m, then the atomic migrating velocity is $v = M\frac{\Delta G}{V_m}$, meaning that the migration rate of vanadium atom is proportional to grain boundary mobility and energy decrement per unit volume which is the driving force of phase transition. The atomic flux due to chemical potential is $J_\mu = vC = MC\frac{\Delta G}{V_m}$.

Besides, concentration gradient also plays a role in vanadium atoms migration. According to Fick's law, $J = -D\frac{\partial C}{\partial x}$, where D is diffusion coefficient and $D = D_0 \exp(-\Delta G^a/RT)$, where ΔG^a is thermal activation energy, D_0 is a constant depending on atomic vibration frequency, coordination number and number of atoms per unit volume.

Therefore, it is easy to find that the net atomic flux at interface can be expressed as:

$$\begin{aligned} J_{net} = J_\mu + J_{\alpha\rightarrow\beta} + J_{\beta\rightarrow\alpha} = MC\frac{\Delta G}{V_m} + \\ D_\alpha \exp(-\Delta G^a_\alpha/RT)\frac{\partial C_{i_\alpha}}{\partial x} + D_\beta \exp(-\Delta G^a_\beta/RT)\frac{\partial C_{i_\beta}}{\partial x} \end{aligned} \tag{5.8}$$

where $D_\alpha, \Delta G^a_\alpha$ are the diffusion constant and thermal activation barrier in α phase, while $D_\beta, \Delta G^a_\beta$ are the diffusion constant and thermal activation barrier in β phase. $C_{i_\alpha}, C_{i_\beta}$ are the vanadium concentration at interface to the α phase limit and β phase limit respectively, as shown Fig.43. Note that $C_\alpha < C_i \leq C^{eq}_\beta$, which is the concentration of beta phase when phase transformation arrives at equilibrium state. To simplify the expression for J_{net}, it's assumed that $\Delta G^a_\beta = \Delta G^a_\alpha + \Delta G$, $D_\alpha \exp(-\Delta G^a_\alpha) =$

$D_\beta \exp(-\Delta G^a_\alpha) = D$, $\frac{\partial C_{i_\alpha}}{\partial x} = -\frac{\partial C_{i_\beta}}{\partial x} = \frac{\partial C}{\partial x}$. Then we have

$$J_{net} = MC\frac{\Delta G}{V_m} + D\frac{\partial C}{\partial x}(\exp(-\Delta G/RT) - 1) \tag{5.9}$$

Expand $\exp(-\Delta G/RT) - 1$ at $\Delta G = 0$, the above expression is approximated with first order as

$$J_{net} = (MC - \frac{DV_m}{RT}\frac{\partial C}{\partial x})\frac{\Delta C}{V_m} \tag{5.10}$$

Considering dt time interval, the α grain boundary migrates dx along direction $\boldsymbol{n}$ normal to the interface. As a consequence of mass conservation, we have the following equation in 3D

$$(C - C_\alpha)dx = J_{net}dt = (CM - \frac{DV_m}{RT}\nabla C \cdot \boldsymbol{n})\frac{\Delta G}{V_m}dt \tag{5.11}$$

further

$$v_{GB} = (\frac{C}{C - C_\alpha}M - \frac{DV_m}{RT(C - C_\alpha)}\nabla C \cdot \boldsymbol{n})\frac{\Delta G}{V_m} \tag{5.12}$$

Intuitively, this approximation contains two components of grain boundary migration. The first one comes from Gibbs energy decrement, and slows down with increasing vanadium concentration at interface; the second one is due to vanadium concentration gradient which speeds up with the extent of vanadium segregation at interface. Understandably, the interface stops migrating at certain transformation point due to the equilibrium of these two counter effects.

It has been observed that the migration rate of vanadium atom can be pronounced anisotropic, related to the inherent anisotropy of hcp structure of α phase[120, 124]. For example, the migration rate is magnitudes slower along the direction normal to α plate than that along the plate expanding direction. Consequently, the migration rate can be written as a vector, and the interface moving velocity at arbitrary position of α grain boundary will be

$$\boldsymbol{v}|_{int} = (\frac{C}{C - C_\alpha}M - \frac{d}{T(C - C_\alpha)}\nabla C \cdot \boldsymbol{n})f \tag{5.13}$$

$$d = \frac{DV_m}{R}, f = \frac{\Delta G}{V_m}$$

Due to the orientation relationship between β and α phase, $\boldsymbol{M} = \boldsymbol{R}\boldsymbol{M}_0$, where spatial orientation of a β grain in terms of $\{110\}$ plane, and $\boldsymbol{M}_0 = (\boldsymbol{M}_{\parallel}, \boldsymbol{M}_{\parallel}, \boldsymbol{M}_{\perp})$, where $\boldsymbol{M}_{\parallel}$ is the atomic migration rate along most densely packed plane, while $\boldsymbol{M}_{\perp}$ perpendicular to it. Although it has been observed that the orientation of α plates on some level is dependent on the orientation of grain boundary allotriomorphic α, which is related to the orientations of adjacent β grains on both sides of the boundary, we simplify the scenario here by assuming that the orientation of a α plate is completely decided by the orientation of β grain it grows into. And we further assume that the 12 variants are of the same possibility to occur.

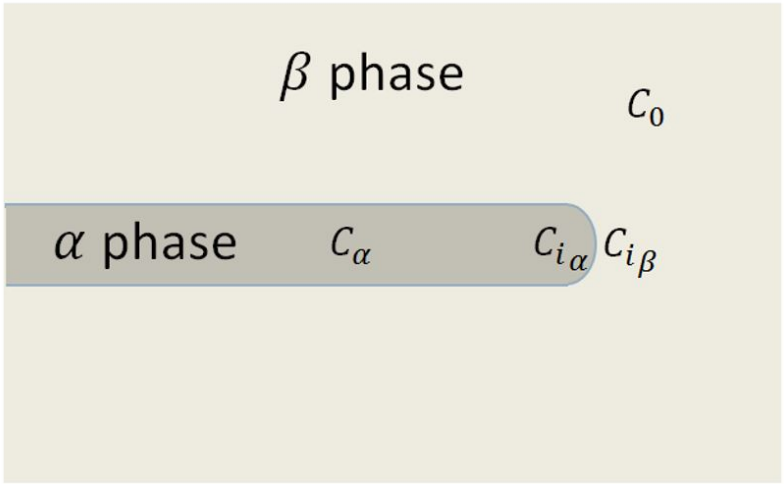

Figure 43: Schematic demonstration of lamellar α growth and the concentration variables.

5.4 The cellular automata model

In our model, each grid is regarded as a cell, which is assumed to be a parcel of atoms. Each cell is functionally defined by seven parameters: position $\boldsymbol{x}$, crystal orientation of k of β phase, grain index z, crystallographic variant s of α phase, initial position $\boldsymbol{x}_N$ of the nuclear seed each cell belongs to, vanadium concentration C, and temperature T. The global hyper parameters defined are: nucleation constant a, atomic migration barrier b, nucleation barrier c, migration rate $\boldsymbol{M}_{\parallel}$, $\boldsymbol{M}_{\perp}$, along and perpendicular most densely packed plane in α, diffusion coefficient d, driving force of phase transformation f. Moore neighborhood definition is used, and the grid correction for the neighbors but the nearest ones is 0.07. The value of each hyper parameter used in the simulation is listed in table 3. Specifically, α^{GB} is for grain boundary α, α^{side} is for lamellar α. Particularly, the value of parameter f is dynamically chosen so that the maximum component $\boldsymbol{v}|_{int}$ is 1.

Table 3: The numerical values for hyper parameters in CA model.

α^{GB}	1	b^{sid3}	10^3	$\boldsymbol{M}_{\parallel}^{GB}$	100	$\boldsymbol{M}_{\parallel}^{side}$	1
α^{side}	1	c^{GB}	10^4	$\boldsymbol{M}_{\perp}^{GB}$	1	d	1
b^{GB}	10^3	c^{side}	10^3	$\boldsymbol{M}_{\perp}^{side}$	100	f	—

We cut a $1mm$ by $1mm$ by $0.375mm$ bock and discretize it into 1000 by 1000 by 375 grids. When FEM simulation is done, the time dependent temperature field on each node is extracted from FEM result and linearly interpolated for each grid for CA simulation. Knowing the $\beta \rightarrow \alpha$ phase transition occurs at 990°C, we assume that, during heating stage, all the cells whose temperature builds up to or above 990°C

become β phase while the rest stays with what they used to be, the state of which will not be modified during the following CA procedure anyway.

To date, there isn't a sufficiently general and efficient model to simulate particle morphology evolution to the knowledge of the authors, even though we have devoted to building novel models for solid state sintering with or without external pressure[125, 126], when it comes to 3D, they become very complicated and computation demanding. To avoid the complexity by devising a posteriori model, we first label all the cells whose highest temperature exceeding 990°C as potential β transformation sites. We then use a separate CA simulation by randomly seeding β nuclei within the labeled area, noting that the number β nuclei can be used to control the average size of β grains. The total number of β grains is set to 100 in this simulation. Next, the β nuclei grow until all the potential β transformation sites are occupied by β cells. Fig.44 shows the obtained beta phase microstructure.

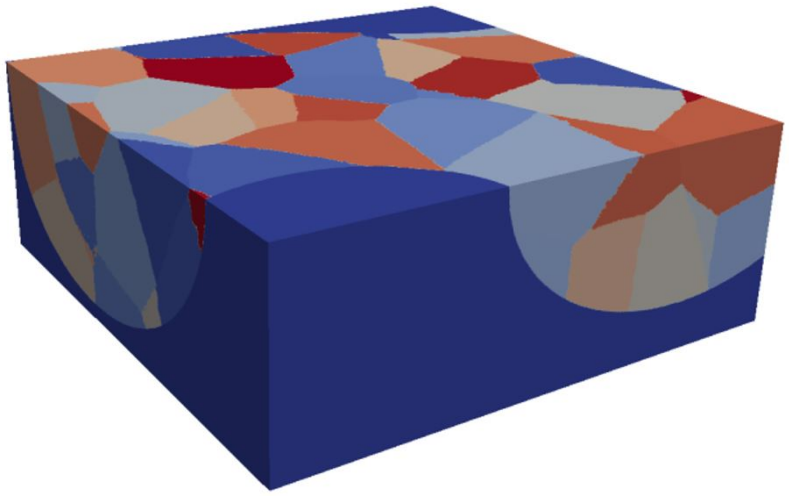

Figure 44: The microstructure of parent β phase generated by a separate CA process.

In next procedure, cooling induced $\beta \rightarrow \alpha$ transformation below 990°C, the nucleation and growth of α phase is modeled. There are roughly two stages of

microstructure evolution during $\beta \rightarrow \alpha$ transformation. First, the allotriomorphic α, also called grian-boundary (GB) α, nucleate and grow along the β grain boundaries. Then, α lamellae nucleate and grow from GB α into β matrix forming large colonies, while β plates are separated by vanadium concentrated β layers. Obviously, for both stages, the mobility of vanadium atoms is anisotropic: for grain boundary α, the rotation matrix $\boldsymbol{R}$ denotes the orientation of tangent plane at a grain boundary point, which is approximately calculated for every GB point before α transformation; for lamellar α, $\boldsymbol{R}$ denotes the orientation of the most densely packed plane, which is decided by the spatial configuration of parent phase as well as variant choice from those 12 variants. Fig.45(a) shows the 3D microstructure obtained at t=0.1s, Fig.45(b) corresponding vertical slice contour and Fig.45(c) horizontal slice contour.

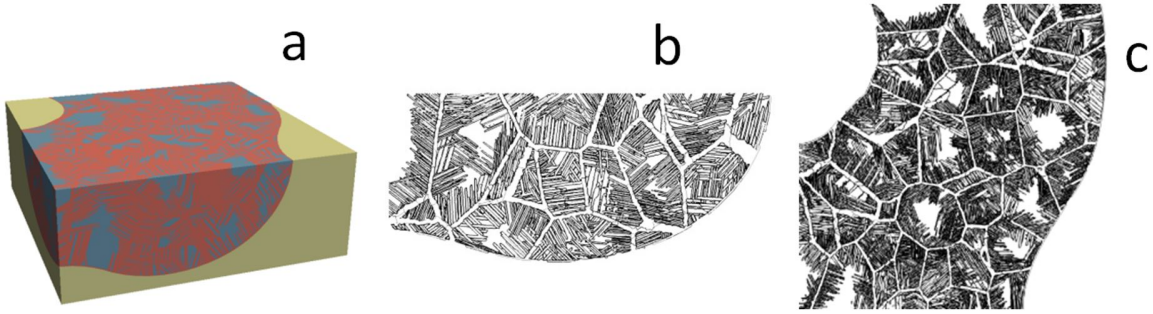

Figure 45: The microstructure of α phase at $t = 0.1s$. (a) 3D visualization; (b) contour of vertical slice; (c) contour of horizontal slice.

To examine the soundness of our model, the volume fraction of transformed α phase is plotted against temperature, compared with the theoretical JMC prediction in Eq.5.3 and 5.4 under linear cooling schedule, in Fig.46. Although it may be straightforward to compare transformed fraction against time, there is a scale gap between experiment and our model, meaning that it's still not clear that how much physical time is equivalent to CA time or CA step. As we can see, two curves agree

reasonably well with each other, from which we can clearly identify the nucleation and growth stage. The overall shift of CA curve is due to the pre-existing grain boundary α before nucleation and growth of lamellar α. Additionally, due to the remaining β phase, the final transformation rate of our simulation is about 0.9, different from the ideally theoretical prediction.

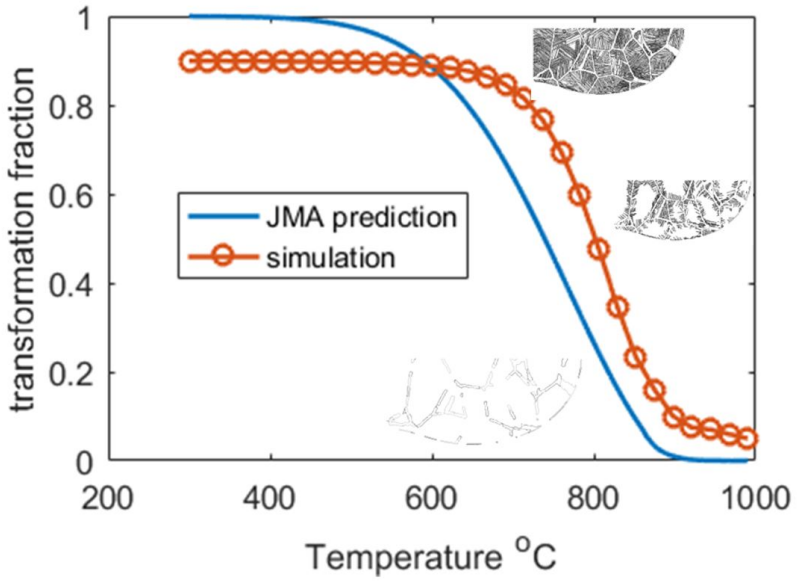

Figure 46: The comparison of transformation fraction between simulation and theoretical prediction.

5.5 Summary

The goal of this work is to establish an integrated model of finite element method and cellular automata to numerically investigate the effects of processing parameters on final microstructure. The FEM part efficiently provides us real time temperature distribution, then the calculated temperature field directs microstructure evolution simulated by cellular automata model. The combinative model is engaged to simulate

the process of selective laser sintering of Ti_6Al_4V, which involves complicated microstructure evolution and solid-state phase transition involving nucleation and growth of irregular grains. It is phenomenologically validated by comparing the kinetics of $\beta \rightarrow \alpha$ phase transition of our simulation with experimentally summarized JMA theory. Based on the obtained titanium alloy microstrucutre after sintering, it's easy to do property predictions and performance evaluations for the produced materials. There are already several algorithms designed for the calculations of basic properties from material microstructure, such as the lattice-spring model, through which we can build surrogate model to quantitatively link the processing parameters and product properties. Such an numerical technique may shed light on *in silico* product design.

The content in this chapter can be found in Chen et al 2018 Modelling Simul. Mater. Sci. Eng. *https://doi.org/10.1088/1361-651X/aabcad.*

Chapter 6

COMPUTING ELASTIC MODULUS FIELD OF HETEROGENEOUS EXTRA-CELLULAR MATRIX VIA INVERSE FEM

6.1 Background

Previous chapters are mainly focused on modeling material microstructure and its time-dependent evolution. In this chapter, we will discuss the algorithm aimed for mechanical property calculation. Basically, there are two ways to determine material properties computationally: the *ab initio* approach and the macroscopic stimulus-response approach. It's reasonable to expect that as the theoretical foundations become more and more developed and the computational platforms become more and more powerful, *ab initio* approach will be heavily applied in a lot of occasions where conventionally only experiments can fulfill the goals. However, based on current situation, it's more computationally feasible to use the other approach, i.e., stimulus-response method, to build combinative model from microstructure to material properties. Here, an inverse finite element method is introduced, which is used to determine the elastic modulus of a material sample through analyzing the responsive displacement filed upon external pressure. Usually, FEM is engaged to compute the displacement field when an object is deformed by external stress, with known mechanical properties, such as elastic modulus and Poisson's ratio. If the mechanical properties are the unknown targets to be calculated, the conventional FEM formulations need to be rearranged, for example, the boundary forces have to

be expressed in terms of integrals involving the local strain (gradient of displacement field) and unknown variables of elastic modulus.

Our inverse FEM computational scheme will be elaborated over the application of calculating the elastic modulus field of extra-cellular matrix (ECM), where the heterogeneity of the mechanical properties are explicitly considered. Specifically, a general formulation will be provided to reconstruct the distinct local elastic modulus values of the heterogeneous ECM from a pre-measured displacement field within the interested region, which may contain active cells of arbitrary shapes. Through the proposed inverse FEM scheme, we are able to establish a set of homogeneous linear equations based on the stress equilibrium conditions where the unknowns are the local modulus values. Given an experimentally measured overall modulus of the ECM E_0, the local modulus values can be uniquely determined by solving the aforementioned set of homogeneous equations and multiply the solution vector by E_0, which also indirectly provides the values of stress and strain including the traction force on the cell surface if there are any.

We first validate our procedure by reconstructing a highly heterogeneous 3D model ECM with alternating arrangement of soft and stiff regions and provide a systematic mesh-size dependency and convergence analysis. Then we employ the procedure to compute the distribution of elastic modulus and stress in a heterogeneous type-I collagen network as well as the traction force on a rounded breast cancer cell in the ECM, based on the deformation field data obtained via 3D reflectance force microscopy. Note that in this system the contraction magnitude is small, and the cell maintains a rounded shape, which indicate linear elastic deformation dominates in the ECM and serves as ideal demonstration case for our general procedure. Finally, the generalization of our formulation for nonlinear situations is also discussed.

6.2 Related work on determining elastic modulus of extra-cellular matrix

Accurately resolving the traction forces on active cells in ECM is crucial to understanding stress homeostasis in cellularized ECM systems and the resulting collective cellular behavior. The majority of 3D traction force microscopy techniques, which compute the stress distribution in ECM as well as cellular traction forces from experimentally measured deformation field in the ECM using dispersed tracing particles or fluorescently-tagged matrix proteins, have assumed a spatially homogeneous ECM with constant material properties at every location in the system. Recent studies have shown that ECM can exhibit significant heterogeneity due to the disordered nature of collagen network as well as cell remodeling. In this paper, we develop a novel procedure for accurately resolving the cellular traction forces by explicitly reconstructing the distinct local elastic modulus values of the heterogeneous ECM containing an arbitrary shaped cell from a measured displacement field in the ECM. Our formulation does not require any a priori knowledge of the boundary conditions, and simultaneously results in the distribution of the heterogeneous modulus values and stress field in the ECM, as well as the traction forces on the cell. We first validate our procedure by reconstructing a highly heterogeneous 3D model ECM with alternating arrangement of soft and stiff regions and provide a systematic mesh-size dependency and convergence analysis. Then we employ the procedure to compute the distribution of elastic modulus in a heterogeneous type-I collagen gel as well as the traction force on a rounded breast cancer cell in the gel, based on the deformation field data obtained via 3D reflectance force microscopy. Finally, the generalization of our formulation for nonlinear situations is also discussed.

Recent studies have shown that the mechanical interactions between cells and

extra-cellular matrix (ECM) play an important role in regulating individual and collective cell migration behaviors in many physiological processes such as wound healing and cancer metastasis [127, 128, 129, 130, 131, 132, 133, 134]. Specifically, a migrating cell can generate active pulling forces on ECM fibers through actomyosin contraction and cell-ECM adhesions [135, 136, 137, 138, 139]. Reciprocally, the local stress state of ECM fibers can also bias the formation of new focal adhesion sites and thus, affects the overall migration of the cells [140, 141].

Due to its great importance and physiological relevance, a significant amount of research efforts have been spent to understand the cell-ECM mechanical interactions[142, 143, 144, 145, 146, 147, 148, 149]. One of the most commonly used approaches is the traction force microscopy, which allows one to compute the stress distribution in the cell-ECM system by tracking the deformation of ECM regions[150]. Specifically, fluoresce-labelled micro-beads are typically embedded in the collagen gel. The displacements of beads are then obtained via time-lapse confocal imaging, which quantitatively represents the displacement field of the ECM. The bead displacement field can be further interpolated and mapped to a prescribed mesh grid points. The stress distribution in the ECM region is subsequently computed for a given (nonlinear) constitutive relation of the ECM material, from which the traction forces on the cells embedded in the ECM can be resolved.

Very recently, a 3D reflectance traction microscopy has been developed, which combines confocal reflection imaging and partial volume correlation post-processing [151]. Specifically, the local displacement field is obtained via individual pixel-based digital image correlation. In contrast to employing dispersed tracing particles or fluorescently-tagged matrix proteins, this method provides a label-free, computationally effective strategy to study the cell mechanics in native 3D extracellular matrix in a

non-invasive fashion. More importantly, it allows one to directly resolve the ECM displacement field on mesh grids without further interpolations.

Most of the traction force microscopy techniques assume that the ECM is a spatially homogeneous medium, i.e., the constitutive relations and local material properties (such as elastic moduli) do not vary at different locations of the material. This assumption allows one to employ constant material properties to compute the stress distribution in the ECM and subsequently resolve the traction forces on the cell. However, recent studies have shown that ECM heterogeneity can significantly affect the stress homeostasis in cellularized ECM systems [152]. The heterogeneity of ECM mechanical properties can be resulted from the original structural and topological disorder of the collagen fiber network [153, 154, 155, 156], as well as the network remodeling by the active cells[157, 158, 159]. In particular, it has been shown that continuous cell contraction can lead to significant fiber bundle formation between neighboring cells, which creates gradients of mechanical properties of the local ECM [34]. Recently, non-uniform local perturbations in ECM mimicking those generated of a cell has been investigated, which indicated ECM heterogeneities can lead to a wide spectrum of mechanical responses to such perturbations[160, 161].

6.3 Method

6.3.1 General reconstruction framework

Reconstruction of the material properties from its response to external or internal stimuli is a classical inverse problem. For example, in many biomedical imaging applications, visualizing the distribution of elastic modulus within a sample of material,

a tissue for example, based on the measured displacements due to perturbations from a ultrasonic or magnetic source, allows one to discriminate the bulk tissue into normal and abnormal regions for further diagnosis [162, 163]. Based on the types of external stimulus, elastic modulus reconstructions generally fall into two categories: (i) reconstruction under dynamic perturbations [164, 165, 166, 167, 168, 169, 170], such as sono-elasticity; and (ii) reconstruction under static perturbations such as simply compressing or stretching the material at boundaries[171, 172, 173, 174, 175, 176]. The static compression based reconstructions, depending on whether or not requiring the actual boundary conditions, can be further divided into absolute modulus reconstruction [177] and relative modulus reconstruction [178, 179], with the latter only calculating the pattern of modulus distribution instead of absolute values.

In this work, we focus on the reconstruction of the distribution of local elastic moduli in a heterogeneous ECM. We model the ECM as a cuboid domain containing an arbitrarily shaped cell. The 3D cell morphology is obtained via confocal microscopy analysis. The displacement field in the ECM region is obtained using 3D reflectance force microscopy and an overall effective elastic modulus of the ECM is experimentally measured. In this case, the stresses on neither the exterior boundary of the bulk ECM nor the cell-ECM interface (i.e., the cell traction forces) are known a priori. These stresses are expressed in terms of the surface or interface strain and local elastic moduli to be solved.

Given the experimentally measured displacements resolved at discrete mesh grids, we first obtain the associated strain field by approximating a continuous displacement field using linear shape functions. To minimize the effects due to the uncertainties in the measured displacement fields and the possible local discontinuities of the material, the directly calculated strain field is smoothed using the least-square approach [180].

Next, we use the smoothed strain field and the unknown local elastic modulus at each boundary node to approximate the boundary forces. Subsequently, the forward finite-element equations based on stress equilibrium conditions are rearranged and reformulated into a set of homogeneous linear equations with the local elastic modulus values as the unknown variables. Finally, those homogeneous linear equations are solved and the relative modulus at each location is obtained. By rescaling the relative modulus with the experimentally measured overall modulus of the ECM, the actual distribution of heterogeneous elastic modulus for the material can be obtained.

We note that our novel procedure distinguish itself from previous modulus reconstruction research in two aspects. First, we provide a general 3D reconstruction formulation that only requires the displacements as input and requires no knowledge or assumptions on the boundary forces. Secondly, it allows us to immediately obtain both the distribution of the heterogeneous modulus and the traction forces on cell surface without further forward finite-element-method calculations. On the other hand, the preponderance of previous researches on reconstruction was focused on 2D systems using plane strain or plane stress approximation and the reconstructions are usually based on the assumption that the moduli at boundary points are identical [178] or the stress distribution is constant [179] within the material.

6.3.2 Strain fitting

One of the important steps in our reconstruction process is to obtain an accurate estimation of the strain field given the measured displacement field, which will be used to approximate the boundary forces. The continuous displacement field within

the ECM material is approximated by

$$\boldsymbol{u}(\boldsymbol{x}) = \boldsymbol{N}(\boldsymbol{x})\boldsymbol{u}^m \tag{6.1}$$

where $\boldsymbol{u}^m$ is the measured displacement data at mesh grids, and $\boldsymbol{N}(\boldsymbol{x})$ is the global shape function. Conventionally, the strain field can be calculated as

$$\boldsymbol{\epsilon}^m = \boldsymbol{\nabla}_s \boldsymbol{u} = \boldsymbol{B}\boldsymbol{u}^m \tag{6.2}$$

where the strain-displacement matrix B consists of spatial derivative of $\boldsymbol{N}(\boldsymbol{x})$. Because $\boldsymbol{\epsilon}^m$ is calculated as the derivative of measured displacements and the uncertainties associated with the displacement measurement may be amplified, we need to further calculate the smoothed strain filed. Assuming $\boldsymbol{\epsilon}^m$ is equal to the linear approximation of the strain field parameterized by smoothed nodal strain $\boldsymbol{\epsilon}^s$ at each location, we have

$$\boldsymbol{N}\boldsymbol{\epsilon}^s = \boldsymbol{\epsilon}^m \tag{6.3}$$

which can be solved by multiplying both sides with $\boldsymbol{N}^T$, i.e.,

$$\boldsymbol{\epsilon}^s = (\boldsymbol{N}^T\boldsymbol{N})^{-1}\boldsymbol{N}^T\boldsymbol{\epsilon}^m \tag{6.4}$$

This strain smoothing scheme can also be used to smooth the measured displacement, however, we observe that strain smoothing is sufficient to obtain accurate modulus reconstruction. Therefore, to keep the algorithm concise and robust, displacement smoothing is not considered as a necessary step here.

6.3.3 Forward FEM formulation

The most commonly used procedure of FEM on static linear elasticity problem works as follows: (1) decide the element to be used; (2) create mesh on the geometry;

(3) calculate element stiffness matrix and construct the global stiffness matrix; (4) apply boundary conditions; (5) solve the linear equations for nodal displacement[181]. In ensuing discussions, we briefly describe the governing differential equations and corresponding matrix form for forward linear elastic problem which will be the basis towards the derivation of modulus reconstruction formulation.

For a material under static (quasi-static) force equilibrium condition, we have

$$\boldsymbol{\nabla}_s^T \boldsymbol{\sigma} + \boldsymbol{b} = 0 \tag{6.5}$$

where $\boldsymbol{\sigma}$ is the stress tensor, $\boldsymbol{b}$ is the body force term and

$$\boldsymbol{\nabla}_s^T = \begin{bmatrix} \frac{\partial}{\partial x} & 0 & 0 & 0 & \frac{\partial}{\partial x} & \frac{\partial}{\partial y} \\ 0 & \frac{\partial}{\partial y} & 0 & \frac{\partial}{\partial z} & 0 & \frac{\partial}{\partial x} \\ 0 & 0 & \frac{\partial}{\partial z} & \frac{\partial}{\partial y} & \frac{\partial}{\partial x} & 0 \end{bmatrix} \tag{6.6}$$

The strain is calculated according to the kinematics equation describing the strain-displacement relation, which is given by:

$$\boldsymbol{\epsilon} = \boldsymbol{\nabla}_s \boldsymbol{u} \tag{6.7}$$

For a linear elastic material, the stress and strain are linearly related by the constitutive equation:

$$\boldsymbol{\sigma} = \boldsymbol{D}\boldsymbol{\epsilon} \tag{6.8}$$

where $\boldsymbol{D}$ is the fourth-order stiffness tensor. Eqs. (5)-(8) define an elasticity problem, the solution of which also requires the specification of proper boundary conditions. There are generally two types of boundary conditions: (i) the natural boundary condition or the force boundary condition, in which the traction forces at material boundary are specified, i.e.,

$$\boldsymbol{\tau}\boldsymbol{n} = \bar{\boldsymbol{t}} \quad \text{on} \quad \Gamma_t \tag{6.9}$$

and (ii) the essential boundary condition or the displacement boundary condition, in which the displacements at the boundary are specified, i.e.,

$$\boldsymbol{u} = \bar{\boldsymbol{u}} \quad \text{on} \quad \Gamma_u \tag{6.10}$$

where Γ_t indicates the traction boundary, and Γ_u indicates the displacement boundary.

In the case that the material under consideration is isotropic and there is no body force, we have

$$\boldsymbol{D} = E\boldsymbol{D}_0 = \frac{E}{(1+v)(1-2v)} \begin{bmatrix} 1-v & v & v & 0 & 0 & 0 \\ v & 1-v & v & 0 & 0 & 0 \\ v & v & 1-v & 0 & 0 & 0 \\ 0 & 0 & 0 & \frac{1-2v}{2} & 0 & 0 \\ 0 & 0 & 0 & 0 & \frac{1-2v}{2} & 0 \\ 0 & 0 & 0 & 0 & 0 & \frac{1-2v}{2} \end{bmatrix} \tag{6.11}$$

$$\boldsymbol{\nabla}_s^T \boldsymbol{\sigma} = \boldsymbol{0} \tag{6.12}$$

$$\boldsymbol{\sigma} = \boldsymbol{D}\boldsymbol{\nabla}_s \boldsymbol{u} \tag{6.13}$$

where E and v are local elastic modulus and Poisson's ratio respectively. By converting the strong form into weak form and using Eq.6.1 to approximate a piecewise displacement field based on the nodal displacement $\boldsymbol{u}$ at the meshed grids, we can immediately obtain the following linear equation set:

$$\sum_L \boldsymbol{B}^T \boldsymbol{D}\boldsymbol{B}\boldsymbol{u} = \boldsymbol{K}\boldsymbol{u} = \boldsymbol{f} \tag{6.14}$$

where $\boldsymbol{B}$ is the matrix version of $\boldsymbol{\nabla}_S$, global stiffness matrix $\boldsymbol{K} = \sum_L \boldsymbol{B}^T \boldsymbol{D}\boldsymbol{B}$, and $\boldsymbol{L}$ is a gathering matrix, which maps the local stiffness matrix and forces on element onto a global stiffness matrix and force vector. With proper boundary conditions [c.f. Eq.6.9 and 6.10], the Eq.6.14 can be solved for the nodal displacements.

6.3.4 Inverse reconstruction formulation

In the inverse reconstruction problem, the nodal displacement in the ECM is known from experiment, and the corresponding displacement field is obtained through linear interpolation within each element using the nodal values (see Eq.6.1). The formulation for our inverse modulus reconstruction is derived by rearranging the forward FEM Eq.6.14, in which the displacement field and its gradient (i.e., the strain field) are used to construct the coefficient matrix (similar to the stiffness matrix in forward FEM calculation) while the local elastic modulus values in each element are treated as the unknowns.

In particular, the essential and natural boundary conditions are expressed in terms of the known displacement field and its derivative as well as the unknown local elastic modulus, i.e.,

$$\bar{\boldsymbol{u}} = \boldsymbol{u}(\boldsymbol{x}), \quad \boldsymbol{x} \in \Gamma_u \tag{6.15}$$

and

$$\bar{\boldsymbol{t}} = \boldsymbol{D}\boldsymbol{\epsilon}^s(\boldsymbol{x}) = \boldsymbol{D}(\boldsymbol{N}^T\boldsymbol{N})^{-1}\boldsymbol{N}^T\boldsymbol{\nabla}_s\boldsymbol{u}(\boldsymbol{x}), \quad \boldsymbol{x} \in \Gamma_t \tag{6.16}$$

Specifically, the traction forces on boundaries are calculated in two steps: first, we compute and smooth out the strain field $\boldsymbol{\epsilon}^s$ according to Eq.6.4; then, the nodes and corresponding element facets for both the exterior boundary of the reconstruction domain and the cell-ECM interface are detected and the traction forces on these boundaries are expressed as $\boldsymbol{D}\boldsymbol{\epsilon}^s$.

Using the calculated strain $\boldsymbol{\epsilon}^s$ to replace $\boldsymbol{B}\boldsymbol{u}$ and $\bar{\boldsymbol{t}}$ and explicitly separating the nodal modulus $\boldsymbol{E}^n$ as the unknown variable, the left-hand side Eq.6.14 can be rearranged and transformed into $\boldsymbol{B}^T\boldsymbol{D}_0\boldsymbol{\epsilon}^s\boldsymbol{N}\boldsymbol{E}^n$, while the right-hand side can be

expressed as $\boldsymbol{N}\boldsymbol{D}_0\boldsymbol{\epsilon}^s_{\Gamma_t}\boldsymbol{N}\boldsymbol{E}^n$. Then the forward FEM equation (14) becomes

$$\sum_L \boldsymbol{B}^T\boldsymbol{D}_0\boldsymbol{\epsilon}^s\boldsymbol{N}\boldsymbol{E}^n \;=\; \sum_L \boldsymbol{N}\boldsymbol{D}_0\boldsymbol{\epsilon}^s_{\Gamma_t}\boldsymbol{N}\boldsymbol{E}^n \tag{6.17}$$

moving the term on the right-hand side to the left, we have

$$\sum_L (\boldsymbol{B}^T\boldsymbol{D}_0\boldsymbol{\epsilon}^s\boldsymbol{N} - \boldsymbol{N}\boldsymbol{D}_0\boldsymbol{\epsilon}^s_{\Gamma_t}\boldsymbol{N})\boldsymbol{E}^n \;=\; \mathbf{0} \tag{6.18}$$

We denote the constant term in front of $\boldsymbol{E}$ by $\boldsymbol{K}_E$, i.e.,

$$\boldsymbol{K}_E\boldsymbol{E}^n \;=\; \mathbf{0} \tag{6.19}$$

We employ a constrained optimization method to find the nontrivial solutions to Eq.6.19. Specifically, the "trust region" algorithm[182] is utilized which uses a quadratic function to approximate the function to be minimized at current search point. In addition, the local minimizer of the approximation function is obtained within a confined neighborhood defined as a hypersphere region. If the attempt fails, the radius of the neighborhood shrinks, and the local minimization step is repeated until a successful trial is achieved. To avoid degrading into the trivial solutions, the constraints on the optimization problem, i.e., a prescribed lower bound on the local elastic modulus, should be satisfied for all attempted solutions. Here, the reflective Newton method is employed to find the solutions satisfying the lower bound, which has been proved to be efficient for large scale problem and exhibit superior convergence behavior [183].

6.4 Results

6.4.1 Modulus reconstruction for a 3D model heterogeneous material

To validate and ascertain the accuracy of reconstruction procedure, a 3D model of heterogeneous material with alternating arrangement of soft and stiff regions characterized by an analytical modulus distribution is designed. After generating a mesh upon a cubic region with tetrahedron elements, we first obtain the nodal displacements under a uniaxial tensile boundary condition using forward FEM calculation. Then, the nodal displacements are provided as the input for our modulus reconstruction algorithm to recover the modulus distribution within the material. We also perform a systematic analysis on how the convergence of our reconstruction algorithm is affected by the mesh resolution used to discretize the material.

Our test material possesses a cubic geometry with edge length L=8 mm and is meshed upon n nodal points with tetrahedral elements. Tetrahedral elements are more flexible to mesh complex geometry such as a motile cell than brick elements, and the corresponding mesh can be easily generated using Delaney tessellation given an arbitrary point cloud without mapping them onto regular grid. The distribution of Young's modulus within material is given by the following analytical function:

$$\frac{\boldsymbol{E}(x,y,z)}{E_0} = 1.0 + 0.1 \sin 0.7x \cos 0.7z(\sin 0.7y + \cos 0.7y) \tag{6.20}$$

where E_0 is a scaling constant (i.e., overall effective modulus) which we set it to 10^6 Pa in our forward FEM displacement calculation, which is cancelled out after normalization. Poisson's ratio is set to be 0.3. In addition, we consider the material is under uniaxial tensile force along the x direction. The corresponding boundary

conditions are

$$\boldsymbol{u}(x=0) \,=\, \mathbf{0}, \quad \boldsymbol{\tau}(x=L) \,=\, [1.0\times 10^4, 0, 0]^T \tag{6.21}$$

We note that in the forward problem, the number of nodes n used to mesh the domain is an important factor determining the accuracy of the calculated displacements. This corresponds to the resolution of the displacement field measured in 3D traction force microscopy, which plays a crucial role to the accuracy of the reconstructed modulus distribution and the resolved traction forces on cells. Therefore, we perform a systematic mesh-size dependency analysis by varying the number of mesh nodes n and obtaining the corresponding displacement fields with different resolution via FEM calculations.

The inverse reconstruction procedure described above is then employed to reproduce the modulus distribution in Eq.6.20 solely based on the nodal displacement data. To better capture the intrinsic spatial variation of the local modulus, in the ensuing discussions we use the normalized modulus defined via

$$E_i \,=\, \frac{E_i^* - E_{\min}}{E_{\max} - E_{\min}} \tag{6.22}$$

where E_i and E_i^* are respectively the normalized and original modulus values at node i, $E_($ max) and $E_{\min}$ are the maximum and minimum modulus value of all the nodes. Clearly, through Eq.6.22, the modulus distribution in each case is mapped into the range [0,1] for easy comparison. This also removes the dependency of the reconstructed modulus on the average modulus value of the entire system. Fig.47 shows the distribution of normalized modulus according to Eq.6.20 and two representative reconstructions from displacement fields associated with 20 and 57 nodes along each dimension respectively.

To quantitatively measure the accuracy of reconstruction, we define the following

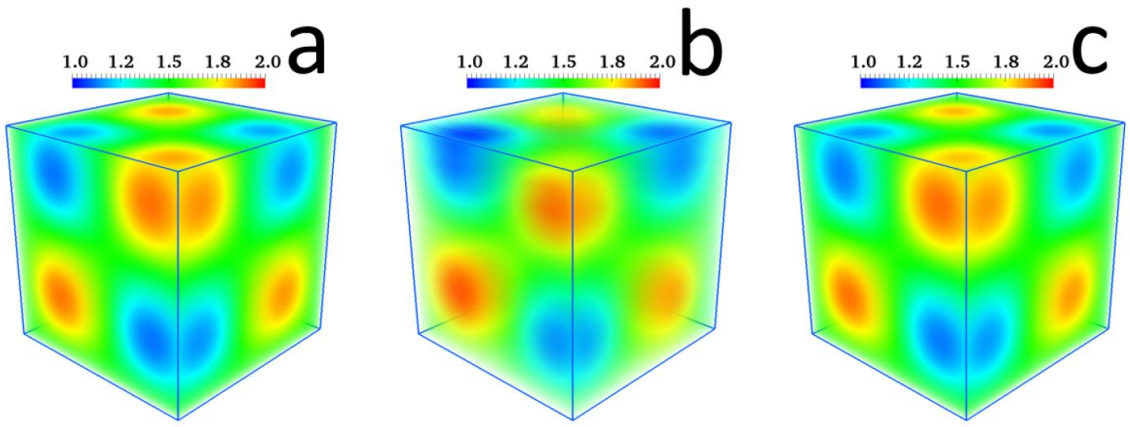

Figure 47: The normalized modulus distribution in a 3D cubic modeling material with edge length $L = 8mm$. (a) Original modulus distribution. (b) Reconstructed modulus distribution associated with a linear mesh size (i.e., number of nodes along each direction) of 20. (c) Reconstructed modulus distribution associated with a linear mesh size of 57. The reconstruction in (b) already captures the main features of the initial modulus distribution, while the reconstruction in (c) almost exactly reproduces the initial modulus distribution.

error metric R, i.e.,

$$R = \frac{1}{n} \sum_i \frac{E_i^{true} - E_i^{reconstr}}{E_i^{reconstr}} \tag{6.23}$$

where n is number of nodes, E_i^{true} and $E_i^{reconstr}$ are the respectively true and reconstructed elastic modulus at node i. Fig.48 shows the plot of the reconstruction error metric R as a function of mesh resolution (i.e., number of nodes). It can be clearly seen from the figure that the reconstruction error monotonically decreases as the mesh resolution increases. This suggests that a high-resolution displacement data measured from experiment can result in more accurate modulus reconstruction and thus, the resolution of the traction forces on the cells.

We also note that our reconstruction procedure is very robust and reliable to produce accurate results even with very low-resolution displacement data. For example, even with the displacement data computed with only 8000 nodes (20 by 20 by 20), we

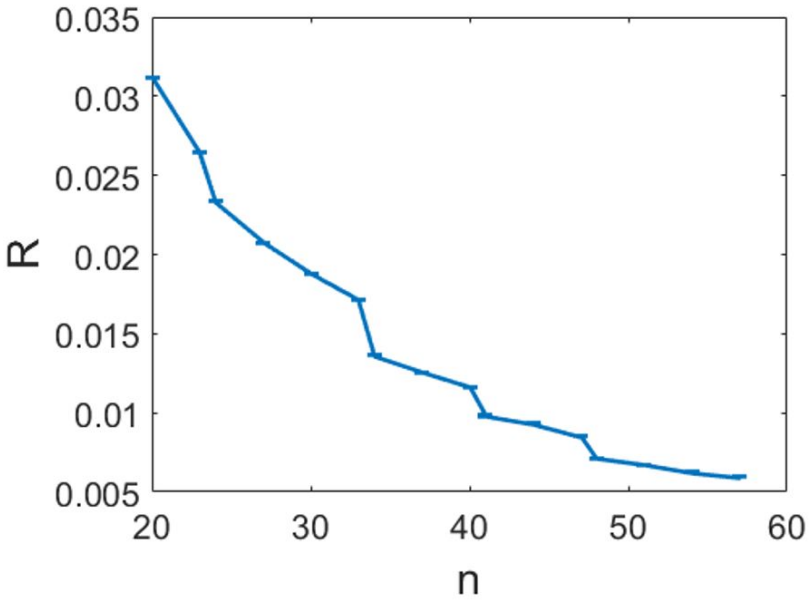

Figure 48: The reconstruction error R as a function of linear mesh size (number of nodes along each direction), which is monotonically decreasing as mesh density increases. The error R is already very small (3%) even when there is only 20 nodal points along each dimension.

can still achieve a 97% reconstruction accuracy for the distribution of modulus values. In addition, when mesh resolution (node number) is sufficiently high (>48 on each dimension, for instance), further increasing the mesh resolution (adding the number of displacement data points) does not significantly improve the reconstruction accuracy. This implies that one can use moderate-resolution displacement data in practice.

6.4.2 Resolving traction forces on breast cancer cell in heterogeneous ECM

With our reconstruction procedure validated, we now apply it to resolve traction forces on a rounded MDA-MB-231 breast cancer cell embedded in type-I collagen gel (ECM) with collagen concentration of $2mg/ml$. This system is particular selected since the contraction magnitude of the cell is relatively small, and the cell maintains a

rounded shape. In this case, it is reasonable to assume that linear elastic deformation dominates in the ECM and it serves as ideal demonstration case for our general reconstruction procedure. The Poisson's ratio of ECM is set to be 0.33. We note that recent studies have shown that ECM can possess a unusual asymmetric Poisson's ratio due to fiber micro-buckling in case of large deformation [150]. Here, we still use the normal value, which is a good approximation for small linear deformations. Our procedure can also apply to other matrices such as elastic hydrogels used in Ref. [148].

The morphology of the cell is obtained via confocal microscopy and the displacement field within the ECM region is obtained via 3D reflectance force microscopy. The reconstruction domain is a cubic box with linear sizes $354.64um$ by $354.64um$ by $130um$ along each direction. Obviously, the finer the mesh is constructed, the more accurate the result will be. However, with ultra fine mesh, the geometry of the cell will be compromised based on the available experimental data. Therefore, the domain is meshed into 63 by 63 by 65 grids to fully utilize the displacement data meanwhile accurately resolve the geometry of the cell. The total number of experimentally measured displacement points within the ECM region is 255405, which are then interpolated to generate a continuous displacement field according to Eq.6.1.

Similar to the validation case described before, the reconstruction domain is first meshed with linear tetrahedral elements and the available displacement data are mapped to the corresponding mesh grid points. Specifically, the mesh for ECM is generated as follows: first, we tessellate the entire system into tetrahedral elements including both the ECM region and the cell region. We then check each element and exclude those elements which contain at least one node within the cell. The remaining ECM elements and the associated nodes are re-ordered and each is assigned with a new global element (node) index. The surface of the cell is approximated by an appropriate

triangle tessellation compatible with the tetrahedral elements at cell-ECM interface, see Fig.49. The normal vector of each boundary facet, including the exterior boundary reconstruction domain and the cell-ECM interface is obtained for approximating boundary forces using the unknown modulus and smoothed boundary strain.

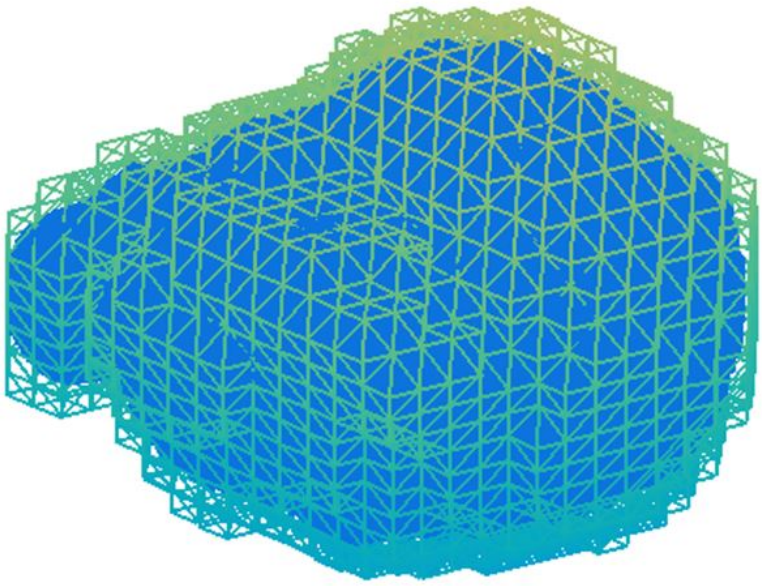

Figure 49: The geometry of the MDA-MB-231 breast cancer cell embedded in the ECM and its surface mesh using tetrahedral elements.

The strain field is calculated and smoothed to reduce the influence the random error introduced in experimental measurement for displacements. The smoothed strain field is then plugged into Eq.6.19 for unknown modulus, which is subsequently solved to obtain the modulus distribution. Fig.50(a) shows the reconstructed distribution of the Young's modulus of the ECM, from which the heterogeneous nature of the modulus distribution can be clearly seen. We note that the far away from the cell, stiff and soft regions of ECM generally possess a uniform distribution, which is mainly due to the disordered nature of collagen network. In addition, the stiff regions tend to cluster towards the cell, which might be due the ECM remodeling in regions close

to the cell. Although the normalized modulus values are used for visualization, the actual modulus values can be easily obtained by a rescaling with respect to the overall average modulus of the ECM $E_0 = 2KPa$. Fig.50(b) shows the variation of the normalized modulus values as one moves away from the cell surface. A clear stiffness gradient can be observed, i.e., as one moves away from the cell surface, the normalized modulus first rapidly decreases and then reaches a plateau value. We note this trend is qualitatively consistent with the experimentally measured local stiffness in cellularized collagen [184].

Once the distribution of ECM modulus is known, it is straightforward to calculate the stress distribution in both the ECM region and one the cell surface according to $\boldsymbol{\sigma} = \boldsymbol{E}\boldsymbol{\epsilon}$, which are respectively shown in Fig.51 and Fig.52. Both the ECM bulk stress distribution and cell surface stress distribution indicate that the cell is in a polarized state, with one end generating isotropic pulling forces (e.g., the red regions on the cell surface) and the opposite end generating compressive forces (e.g., the blue regions on the cell surface). This analysis suggests that the cell is active contracting on one side while swelling on the other side, corresponding to typical state during cell migration. This study clearly demonstrates the utility and robustness of our approach.

6.5 Conclusions and discussion

In this chapter, we have developed a novel procedure for accurately resolving the cellular traction forces by explicitly taking into account the heterogeneity of the ECM. Specifically, we have reconstructed the distinct local elastic modulus values of the

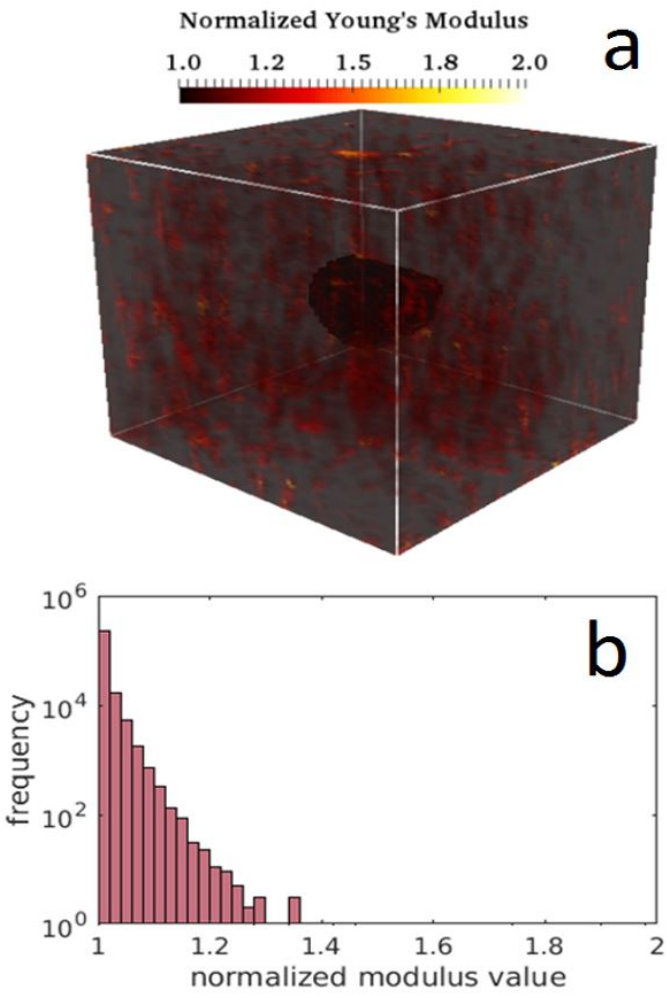

Figure 50: Reconstructed distribution of the normalized modulus within the ECM. The dark region shows the embedded cell. The red color indicates locally stiff regions. (b) The frequency distribution (in log scale) of normalized local modulus values.

heterogeneous ECM containing an arbitrary shaped cell, based on a prescribed ECM displacement field and an overall modulus of the ECM. Our formulation does not require any assumptions on the boundary conditions for the reconstruction domain and directly provides the forces on the exterior boundary of the reconstruction domain as well as the traction forces on the cell. We have validated our procedure by reconstructing a highly heterogeneous 3D model ECM with alternating arrangement of

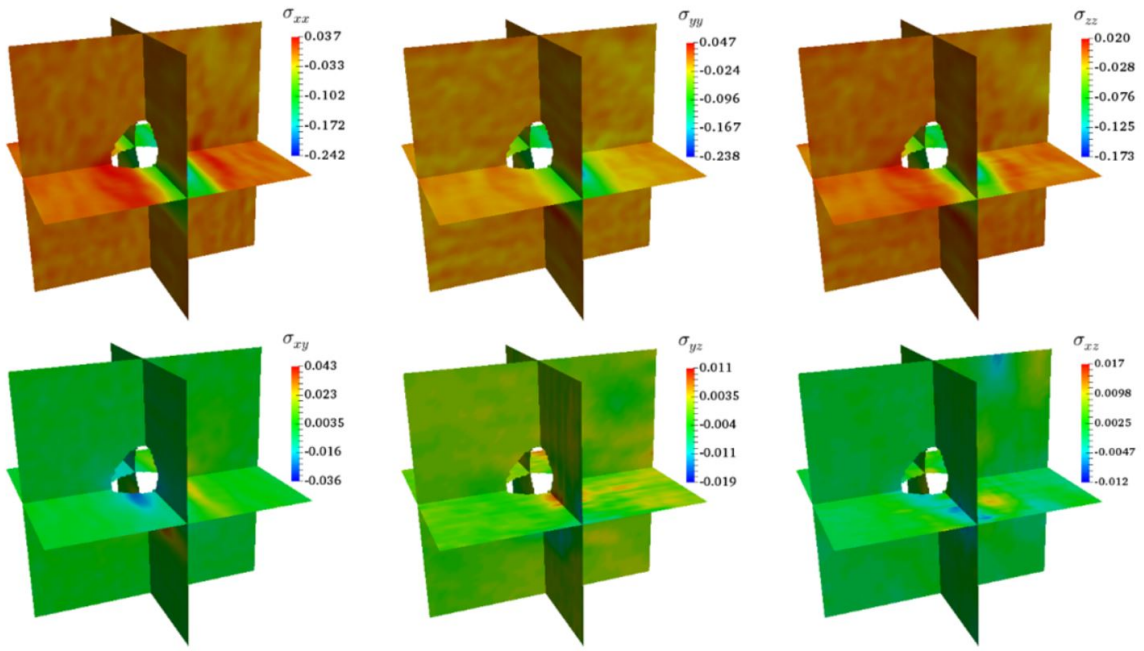

Figure 51: Distribution of normalized stress within in the ECM. σ_{xx}, σ_{yy} and σ_{zz} are normal stresses along x,y,z directions, positive values indicate traction and negative values indicate compression; σ_{xy}, σ_{yz} and σ_{xz} are shear stresses.

soft and stiff regions and provided a systematic mesh-size dependency and convergence analysis. In addition, we have employed the procedure to compute the distribution of elastic modulus and stress in a heterogeneous type-I collagen network as well as the traction force on a motile breast cancer cell in the ECM, based on the deformation field data obtained via 3D reflectance force microscopy. Our analysis showed that the cell is in a polarized state with contracting and swelling modes on opposite ends, indicating its active motion. Our procedure allows one to dynamically track the stress and traction forces on migrating cells with time-lapse displacement data and to obtain insights on the mechanisms for force-regulated collective cell migration.

We note that in the examples considered in this paper, we have assumed linear elasticity in the ECM. This is true for relative small cell induced ECM deformations. However, the general reconstruction formulation can be readily extended to non-linear

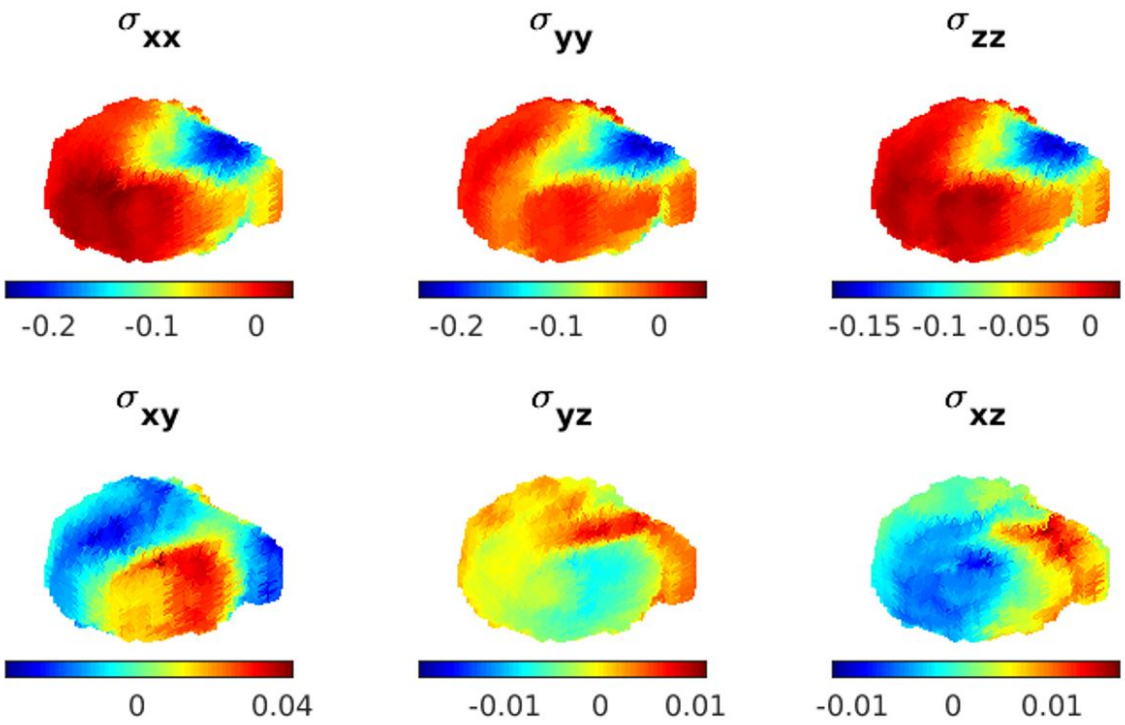

Figure 52: Distribution of normalized stress on cell surface. In the cases of normal stress (i.e., the upper panels), the red region corresponds to cell contraction and the blue region corresponds to cell stretching.

situations where large deformation occurs. Following a similar procedure as introduced above, instead of only recording the final state, a time-lapse nodal displacement data $\boldsymbol{u}(\boldsymbol{x}, t)$ will be obtained and the static Eq.6.19 is generalized to the time-dependent equation

$$\boldsymbol{K}_E(t)\boldsymbol{E}^n(t) \;=\; \mathbf{0} \tag{6.24}$$

To solve Eq.6.24 at a particular time t, the displacement data at time t and time $t + \Delta t$ can be treated as the initial and final state and our procedure for the linear case can be applied assuming that the ECM is not significantly distorted by the cell within a small time interval t. In this way, not only can we deal with non-linear large

deformations of the ECM, but also numerically investigate the dynamical interaction between and active cell and the variation of ECM modulus due to cell remodeling.

Finally, the proposed inverse FEM computational scheme can be applied to any solid material system, and the experimentally measured displacement filed can also be replaced by numerically obtained displacement field using recently reported algorithms, such as lattice-spring model. Specifically, to generate numerical displacement field using lattice-spring model, the microstructure of a material sample need to be converted into a discrete lattice points linking by artificially defined springs. Upon the application of stress and displacement boundaries, each lattice point will translate by a certain amount and each spring will deform by some degree, which can be conveniently regarded as the displacement field. Based on such a displacement field, we can use the inverse FEM to calculate elastic modulus field of the material sample.

Chapter 7

FUTURE WORK

In this thesis, our efforts towards establishing combinative modeling techniques are introduced, which are aiming to simulate the whole procedure of "processing→microstructure evelution→property prediction" in solid state sintering. Specifically, the packing configuration of solid powders is generated via DEM simulation (chapter 2), the interconnection of powders and accompanying densification is simulated using kinetic Monte Carlo method (chapter 4), possible phase transition during sintering is simulated using celluar automata approach (chapter 6), and material property, such as elastic modulus, can be obtained using inverse FEM (chapter 6). In addition, to further reduce the simulation cost of homogeneous materials, their microstructure related modelings and simulations can be performed in 2D first and the corresponding 3D microstructure can be easily obtained using stochastic reconstruction technique (chapter 3), the accuracy of which has been proved satisfying for the 3D microstructure reconstruction of polycrystalline materials. The preliminary results reported the thesis indicate that coupling multiple simulation methods to describe complicated physical processes is possible and effective. However, to truly create an integrated model capable of simulating the whole process of powder compaction, microstructure evolution and all the way to material properties, long-term efforts are still required, especially in following aspects:

- Create more efficient microstructure evolution algorithms. Current kinetic Monte Carlo algorithm discussed in chapter 4 is proven effective in resolving microstructure evolution during solid state sintering. However, it's quite time

consuming if directly augmented to 3D configuration. Generally speaking, MC based algorithm is difficult to be parallelized, therefore, new algorithms need to be invented in future.

- Densification and phase transition need to be coupled. Currently, densification process is simulated phenomenologically regardless of the chemical activities taking place at smaller length scale, which however plays an important role in controlling density evolution in reality. Such a coupling should be addressed explicitly in a combinative model.
- More sophisticated model is needed to calculate material properties based on simulated microstructure. The lattice-spring model currently is only efficient in determining elastic modulus filed and related material properties. Viscoelastic property and plastic behavior should also be considered in future model development.
- Both individual models and model couplings should be carefully calibrated via experimental data. Specifically, there are quite a few simulation parameters introduced in the combinative model, these parameters may or may not correspond to existing physical quantities, therefore, their effective value should be determined or fitted experimentally.
- Uncertainty of the modeling and simulation should be addressed and quantified. When coupling different models, the simulation uncertainty may propagate and be amplified through the interfacing algorithms. As a result, the overall uncertainty may become the most significant factor that jeopardize the effectiveness of the integrated model. Therefore, uncertainty should be quantified for each model as well as its propagation behavior across different models.

If above tasks are fulfilled, the combinative numerical simulation modeling will be

quite promising in place of experiments under a lot of circumstances. As the constant development of powerful computers proceeds, atomic level numerical methods, such density functional theory (DFT) for electronic structure calculation and molecular dynamics (MD) for atomic activity simulation, can also be incorporated in the combinative model in future.

REFERENCES

[1] A. A. Mahmood and M. Elektorowicz. "A Review of Discrete Element Method Research on Particulate Systems". en. In: *IOP Conference Series: Materials Science and Engineering* 136.1 (2016), p. 012034. ISSN: 1757-899X. DOI: 10.1088/1757-899X/136/1/012034. URL: http://stacks.iop.org/1757-899X/136/i=1/a=012034 (visited on 04/14/2017).

[2] Tingwen Li et al. "The NETL MFiX Suite of multiphase flow models: A brief review and recent applications of MFiX-TFM to fossil energy Technologies". In: *Chemical Engineering Science* (). ISSN: 0009-2509. DOI: 10.1016/j.ces.2016.07.043. URL: http://www.sciencedirect.com/science/article/pii/S0009250916304171 (visited on 04/14/2017).

[3] M. Syamlal et al. "Advanced coal gasifier designs using large-scale simulations". en. In: *Journal of Physics: Conference Series* 180.1 (2009), p. 012034. ISSN: 1742-6596. DOI: 10.1088/1742-6596/180/1/012034. URL: http://stacks.iop.org/1742-6596/180/i=1/a=012034 (visited on 04/14/2017).

[4] Rupak Biswas. *Parallel Computational Fluid Dynamics: Recent Advances and Future Directions*. DEStech Publications, Inc, 2010.

[5] Sreekanth Pannala, Ed D'Azevedo, and Madhava Syamlal. "Hybrid (OpenMP and MPI) Parallelization of MFIX: A Multiphase CFD Code for Modeling Fluidized Beds". In: *Proceedings of the 2003 ACM Symposium on Applied Computing*. SAC '03. New York, NY, USA: ACM, 2003, pp. 199–206. ISBN: 978-1-58113-624-1. DOI: 10.1145/952532.952574. URL: http://doi.acm.org/10.1145/952532.952574 (visited on 04/14/2017).

[6] Tingwen Li et al. "Open-source MFIX-DEM software for gas-solids flows: Part II ??Validation studies". In: *Powder Technology*. Selected Papers from the 2010 NETL Multiphase Flow Workshop 220 (Apr. 2012), pp. 138–150. ISSN: 0032-5910. DOI: 10.1016/j.powtec.2011.09.020. URL: http://www.sciencedirect.com/science/article/pii/S0032591011005031 (visited on 04/14/2017).

[7] Tingwen Li et al. "Open-source MFIX-DEM software for gas-solids flows: Part II ??Validation studies". In: *Powder Technology*. Selected Papers from the 2010 NETL Multiphase Flow Workshop 220 (Apr. 2012), pp. 138–150. ISSN: 0032-5910. DOI: 10.1016/j.powtec.2011.09.020. URL: http://www.sciencedirect.com/science/article/pii/S0032591011005031 (visited on 04/14/2017).

[8] Kyle J. Berger and Christine M. Hrenya. "Challenges of DEM: II. Wide particle size distributions". In: *Powder Technology* 264 (Sept. 2014), pp. 627–633. ISSN: 0032-5910. DOI: 10.1016/j.powtec.2014.04.096. URL: http://www.sciencedirect.com/science/article/pii/S0032591014005427 (visited on 04/14/2017).

[9] Y. Jiao, F. H. Stillinger, and S. Torquato. "Distinctive features arising in maximally random jammed packings of superballs". In: *Physical Review E* 81.4 (Apr. 2010), p. 041304. DOI: 10.1103/PhysRevE.81.041304. URL: https://link.aps.org/doi/10.1103/PhysRevE.81.041304 (visited on 04/14/2017).

[10] Christoph Kloss et al. "Models, algorithms and validation for opensource DEM and CFD-DEM". In: *Progress in Computational Fluid Dynamics, an International Journal* 12.2-3 (Jan. 2012), pp. 140–152. ISSN: 1468-4349. DOI: 10.1504/PCFD.2012.047457. URL: http://www.inderscienceonline.com/doi/abs/10.1504/PCFD.2012.047457 (visited on 04/14/2017).

[11] Heather N. Emady et al. "Prediction of conductive heating time scales of particles in a rotary drum". In: *Chemical Engineering Science* 152 (Oct. 2016), pp. 45–54. ISSN: 0009-2509. DOI: 10.1016/j.ces.2016.05.022. URL: http://www.sciencedirect.com/science/article/pii/S0009250916302627 (visited on 04/14/2017).

[12] William R Ketterhagen et al. "Granular segregation in discharging cylindrical hoppers: a discrete element and experimental study". In: *Chemical Engineering Science* 62.22 (2007), pp. 6423–6439.

[13] Douglas S Massey and Nancy A Denton. *American apartheid: Segregation and the making of the underclass*. Harvard University Press, 1993.

[14] Aleksandar Donev, Salvatore Torquato, and Frank H. Stillinger. "Neighbor List Collision-Driven Molecular Dynamics Simulation for Nonspherical Particles. I. Algorithmic Details II. Applications to Ellipses and Ellipsoids". In: *arXiv:physics/0405089* (May 2004). arXiv: physics/0405089. URL: http://arxiv.org/abs/physics/0405089 (visited on 04/15/2017).

[15] Anthony D. Rollett et al. "Three-Dimensional Characterization of Microstructure by Electron Back-Scatter Diffraction". In: *Annual Review of Materials Research* 37.1 (2007), pp. 627–658. DOI: 10.1146/annurev.matsci.37.052506.084401. URL: http://dx.doi.org/10.1146/annurev.matsci.37.052506.084401 (visited on 04/16/2017).

[16] David M. Saylor et al. "Statistically representative three-dimensional microstructures based on orthogonal observation sections". en. In: *Metallurgical and*

Materials Transactions A 35.7 (July 2004), pp. 1969–1979. ISSN: 1073-5623, 1543-1940. DOI: 10.1007/s11661-004-0146-0. URL: https://link.springer.com/article/10.1007/s11661-004-0146-0 (visited on 04/16/2017).

[17] A. Brahme et al. "3D reconstruction of microstructure in a commercial purity aluminum". In: *Scripta Materialia*. Viewpoint set no. 41 Characterization and Analysis of Materials??Organized by G. Spanos 55.1 (July 2006), pp. 75–80. ISSN: 1359-6462. DOI: 10.1016/j.scriptamat.2006.02.017. URL: http://www.sciencedirect.com/science/article/pii/S1359646206001229 (visited on 04/16/2017).

[18] Michael Groeber et al. "A framework for automated analysis and simulation of 3D polycrystalline microstructures.: Part 1: Statistical characterization". In: *Acta Materialia* 56.6 (Apr. 2008), pp. 1257–1273. ISSN: 1359-6454. DOI: 10.1016/j.actamat.2007.11.041. URL: http://www.sciencedirect.com/science/article/pii/S1359645407007914 (visited on 04/16/2017).

[19] Michael Groeber et al. "A framework for automated analysis and simulation of 3D polycrystalline microstructures. Part 2: Synthetic structure generation". In: *Acta Materialia* 56.6 (Apr. 2008), pp. 1274–1287. ISSN: 1359-6454. DOI: 10.1016/j.actamat.2007.11.040. URL: http://www.sciencedirect.com/science/article/pii/S1359645407007872 (visited on 04/16/2017).

[20] F Ochoa, JJ Williams, and N Chawla. "Effects of cooling rate on the microstructure and tensile behavior of a Sn-3.5 wt.% Ag solder". In: *Journal of Electronic Materials* 32.12 (2003), pp. 1414–1420.

[21] F Ochoa, X Deng, and N Chawla. "Effects of cooling rate on creep behavior of a Sn-3.5 Ag alloy". In: *Journal of electronic materials* 33.12 (2004), pp. 1596–1607.

[22] Hefei Zou, Qingsheng Zhu, and Zhefeng Zhang. "Growth kinetics of intermetallic compounds and tensile properties of Sn–Ag–Cu/Ag single crystal joint". In: *Journal of Alloys and Compounds* 461.1-2 (2008), pp. 410–417.

[23] MR Harrison, JH Vincent, and HAH Steen. "Lead-free reflow soldering for electronics assembly". In: *Soldering & Surface Mount Technology* 13.3 (2001), pp. 21–38.

[24] Mulugeta Abtew and Guna Selvaduray. "Lead-free solders in microelectronics". In: *Materials Science and Engineering: R: Reports* 27.5-6 (2000), pp. 95–141.

[25] Minhua Lu et al. “Effect of Sn grain orientation on electromigration degradation mechanism in high Sn-based Pb-free solders”. In: *Applied Physics Letters* 92.21 (2008), p. 211909.

[26] Yanghua Xia et al. “Coupling effects at Cu (Ni)–SnAgCu–Cu (Ni) sandwich solder joint during isothermal aging”. In: *Journal of alloys and compounds* 417.1-2 (2006), pp. 143–149.

[27] MA Dudek et al. “Three-dimensional (3D) visualization of reflow porosity and modeling of deformation in Pb-free solder joints”. In: *Materials Characterization* 61.4 (2010), pp. 433–439.

[28] Milad Maleki, Joë Cugnoni, and John Botsis. “Isothermal Ageing of SnAgCu Solder Alloys: Three-Dimensional Morphometry Analysis of Microstructural Evolution and Its Effects on Mechanical Response”. In: *Journal of electronic materials* 43.4 (2014), pp. 1026–1042.

[29] Salvatore Torquato. *Random Heterogeneous Materials: Microstructure and Macroscopic Properties*. en. Google-Books-ID: UTfoBwAAQBAJ. Springer Science & Business Media, Apr. 2013. ISBN: 978-1-4757-6355-3.

[30] C. L. Y. Yeong and S. Torquato. “Reconstructing random media”. In: *Physical Review E* 57.1 (Jan. 1998), pp. 495–506. DOI: 10.1103/PhysRevE.57.495. URL: https://link.aps.org/doi/10.1103/PhysRevE.57.495 (visited on 04/15/2017).

[31] C. L. Y. Yeong and S. Torquato. “Reconstructing random media. II. Three-dimensional media from two-dimensional cuts”. In: *Physical Review E* 58.1 (July 1998), pp. 224–233. DOI: 10.1103/PhysRevE.58.224. URL: https://link.aps.org/doi/10.1103/PhysRevE.58.224 (visited on 04/15/2017).

[32] David M Saylor et al. “Distribution of grain boundaries in aluminum as a function of five macroscopic parameters”. In: *Acta Materialia* 52.12 (2004), pp. 3649–3655.

[33] Megan E Frary and Christopher A Schuh. “Correlation-space description of the percolation transition in composite microstructures”. In: *Physical Review E* 76.4 (2007), p. 041108.

[34] Samuel E Wilding and David T Fullwood. “Clustering metrics for two-phase composites”. In: *Computational Materials Science* 50.7 (2011), pp. 2262–2272.

[35] Dongsheng Li. “Review of structure representation and reconstruction on mesoscale and microscale”. In: *JOM* 66.3 (2014), pp. 444–454.

[36] BL Hansen et al. “On the reconstruction of polycrystalline microstructures from two-point correlation statistics”. In: *Journal of computer-aided materials design* 10.3 (2005), pp. 163–173.

[37] David T. Fullwood, Stephen R. Niezgoda, and Surya R. Kalidindi. “Microstructure reconstructions from 2-point statistics using phase-recovery algorithms”. In: *Acta Materialia* 56.5 (Mar. 2008), pp. 942–948. ISSN: 1359-6454. DOI: 10.1016/j.actamat.2007.10.044. URL: http://www.sciencedirect.com/science/article/pii/S1359645407007458 (visited on 04/15/2017).

[38] S. Torquato. “Microstructure characterization and bulk properties of disordered two-phase media”. en. In: *Journal of Statistical Physics* 45.5-6 (Dec. 1986), pp. 843–873. ISSN: 0022-4715, 1572-9613. DOI: 10.1007/BF01020577. URL: https://link.springer.com/article/10.1007/BF01020577 (visited on 04/15/2017).

[39] Sudhanshu S Singh et al. “Modeling anisotropic multiphase heterogeneous materials via directional correlation functions: Simulations and experimental verification”. In: *Metallurgical and Materials Transactions A* 43.12 (2012), pp. 4470–4474.

[40] Kirill M Gerke et al. “Improving pattern reconstruction using directional correlation functions”. In: *EPL (Europhysics Letters)* 106.6 (2014), p. 66002.

[41] Y. Jiao, F. H. Stillinger, and S. Torquato. “Modeling heterogeneous materials via two-point correlation functions. II. Algorithmic details and applications”. In: *Physical Review E* 77.3 (Mar. 2008), p. 031135. DOI: 10.1103/PhysRevE.77.031135. URL: https://link.aps.org/doi/10.1103/PhysRevE.77.031135 (visited on 04/15/2017).

[42] C. J. Gommes, Y. Jiao, and S. Torquato. “Density of States for a Specified Correlation Function and the Energy Landscape”. In: *Physical Review Letters* 108.8 (Feb. 2012), p. 080601. DOI: 10.1103/PhysRevLett.108.080601. URL: https://link.aps.org/doi/10.1103/PhysRevLett.108.080601 (visited on 04/16/2017).

[43] S. Torquato. “Interfacial surface statistics arising in diffusion and flow problems in porous media”. eng. In: *The Journal of chemical physics* 85.8 (1986), pp. 4622–4628. ISSN: 0021-9606. URL: http://cat.inist.fr/?aModele=afficheN&cpsidt=8388305 (visited on 04/15/2017).

[44] Y. Jiao, F. H. Stillinger, and S. Torquato. “A superior descriptor of random textures and its predictive capacity”. en. In: *Proceedings of the National Academy of Sciences* 106.42 (Oct. 2009), pp. 17634–17639. ISSN: 0027-8424, 1091-6490. DOI:

10.1073/pnas.0905919106. URL: http://www.pnas.org/content/106/42/17634 (visited on 04/15/2017).

[45] S. Torquato and M. Avellaneda. "Diffusion and reaction in heterogeneous media : pore size distribution, relaxation times, and mean survival time". eng. In: *The Journal of chemical physics* 95.9 (1991), pp. 6477–6489. ISSN: 0021-9606. URL: http://cat.inist.fr/?aModele=afficheN&cpsidt=5453067 (visited on 04/15/2017).

[46] S. Torquato, J. D. Beasley, and Y. C. Chiew. "Two-point cluster function for continuum percolation". In: *Journal of Chemical Physics* 88 (May 1988), pp. 6540–6547. ISSN: 0021-9606. DOI: 10.1063/1.454440. URL: http://adsabs.harvard.edu/abs/1988JChPh..88.6540T (visited on 04/15/2017).

[47] Muhammad Sahimi. *Heterogeneous Materials I: Linear transport and optical properties*. Vol. 22. Springer Science & Business Media, 2003.

[48] VA Snyder, J Alkemper, and PW Voorhees. "The development of spatial correlations during Ostwald ripening: a test of theory". In: *Acta Materialia* 48.10 (2000), pp. 2689–2701.

[49] Ming-Kuei Hu. "Visual pattern recognition by moment invariants". In: *IRE transactions on information theory* 8.2 (1962), pp. 179–187.

[50] C Manwart and R Hilfer. "Reconstruction of random media using Monte Carlo methods". In: *Physical Review E* 59.5 (1999), p. 5596.

[51] En-Yu Guo et al. "Accurate modeling and reconstruction of three-dimensional percolating filamentary microstructures from two-dimensional micrographs via dilation-erosion method". In: *Materials Characterization* 89 (Mar. 2014), pp. 33–42. ISSN: 1044-5803. DOI: 10.1016/j.matchar.2013.12.011. URL: http://www.sciencedirect.com/science/article/pii/S1044580313003823 (visited on 04/16/2017).

[52] Yang Jiao, Eric Padilla, and Nikhilesh Chawla. "Modeling and predicting microstructure evolution in lead/tin alloy via correlation functions and stochastic material reconstruction". In: *Acta Materialia* 61.9 (May 2013), pp. 3370–3377. ISSN: 1359-6454. DOI: 10.1016/j.actamat.2013.02.026. URL: http://www.sciencedirect.com/science/article/pii/S1359645413001481 (visited on 04/16/2017).

[53] Salvatore Torquato et al. “Elastic properties and structure of interpenetrating boron carbide/aluminum multiphase composites”. In: *Journal of the American Ceramic Society* 82.5 (1999), pp. 1263–1268.

[54] Yang Jiao, Frank H. Stillinger, and Salvatore Torquato. “Geometrical ambiguity of pair statistics. II. Heterogeneous media”. In: *Physical Review E* 82.1 (July 2010), p. 011106. DOI: 10.1103/PhysRevE.82.011106. URL: https://link.aps.org/doi/10.1103/PhysRevE.82.011106 (visited on 04/16/2017).

[55] Chase E. Zachary and Salvatore Torquato. “Improved reconstructions of random media using dilation and erosion processes”. In: *Physical Review E* 84.5 (Nov. 2011), p. 056102. DOI: 10.1103/PhysRevE.84.056102. URL: https://link.aps.org/doi/10.1103/PhysRevE.84.056102 (visited on 04/16/2017).

[56] Yang Jiao, Frank H. Stillinger, and Salvatore Torquato. “Nonuniversality of density and disorder in jammed sphere packings”. eng. In: *Journal of applied physics* 109.1 (2011). ISSN: 0021-8979. URL: http://cat.inist.fr/?aModele=afficheN&cpsidt=24277613 (visited on 04/16/2017).

[57] N. Chawla, V. V. Ganesh, and B. Wunsch. “Three-dimensional (3D) microstructure visualization and finite element modeling of the mechanical behavior of SiC particle reinforced aluminum composites”. In: *Scripta Materialia* 51.2 (July 2004), pp. 161–165. ISSN: 1359-6462. DOI: 10.1016/j.scriptamat.2004.03.043. URL: http://www.sciencedirect.com/science/article/pii/S1359646204001915 (visited on 04/16/2017).

[58] S. Torquato and Y. Jiao. “Dense packings of the Platonic and Archimedean solids”. en. In: *Nature* 460.7257 (Aug. 2009), pp. 876–879. ISSN: 0028-0836. DOI: 10.1038/nature08239. URL: https://www.nature.com/nature/journal/v460/n7257/full/nature08239.html (visited on 04/16/2017).

[59] Hechao Li, Nikhilesh Chawla, and Yang Jiao. “Reconstruction of heterogeneous materials via stochastic optimization of limited-angle X-ray tomographic projections”. In: *Scripta Materialia* 86 (Sept. 2014), pp. 48–51. ISSN: 1359-6462. DOI: 10.1016/j.scriptamat.2014.05.002. URL: http://www.sciencedirect.com/science/article/pii/S1359646214001900 (visited on 04/16/2017).

[60] Randall M German. “Sintering theory and practice”. In: *Solar-Terrestrial Physics (Solnechno-zemnaya fizika)* (1996), p. 568.

[61] Zhigang Zak Fang. *Sintering of advanced materials*. Elsevier, 2010.

[62] Mohamed N Rahaman. *Ceramic processing*. CRC press, 2017.

[63] George C Kuczynski. "Self-diffusion in sintering of metallic particles". In: *JOM* 1.2 (1949), pp. 169–178.

[64] Robert L Coble. "Sintering crystalline solids. I. Intermediate and final state diffusion models". In: *Journal of applied physics* 32.5 (1961), pp. 787–792.

[65] W_ D_ Kingery and Morris Berg. "Study of the initial stages of sintering solids by viscous flow, evaporation-condensation, and self-diffusion". In: *Journal of Applied Physics* 26.10 (1955), pp. 1205–1212.

[66] JK Mackenzie and R Shuttleworth. "A phenomenological theory of sintering". In: *Proceedings of the Physical Society. Section B* 62.12 (1949), p. 833.

[67] D Lynn Johnson. "New Method of Obtaining Volume, Grain-Boundary, and Surface Diffusion Coefficients from Sintering Data". In: *Journal of Applied Physics* 40.1 (1969), pp. 192–200.

[68] MF Ashby. "A first report on sintering diagrams". In: *Acta Metallurgica* 22.3 (1974), pp. 275–289.

[69] W Beere. "The second stage sintering kinetics of powder compacts". In: *Acta Metallurgica* 23.1 (1975), pp. 139–145.

[70] George W Scherer. "Sintering of Low-Density Glasses: I, Theory". In: *Journal of the American Ceramic Society* 60.5-6 (1977), pp. 236–239.

[71] HE Exner. "Solid-state sintering: critical assessment of theoretical concepts and experimental methods". In: *Powder Metallurgy* 23.4 (1980), pp. 203–209.

[72] Eugene A Olevsky. "Theory of sintering: from discrete to continuum". In: *Materials Science and Engineering: R: Reports* 23.2 (1998), pp. 41–100.

[73] Syed Ismail Ahmad, P Koteshwar Rao, and Iizhar Ahmed Syed. "Sintering temperature effect on density, structural and morphological properties of Mg- and Sr-doped ceria". In: *Journal of Taibah University for Science* 10.3 (2016), pp. 381–385.

[74] James D Hansen et al. "Combined-Stage Sintering Model". In: *Journal of the American Ceramic Society* 75.5 (1992), pp. 1129–1135.

[75] Hunghai Su and D Lynn Johnson. "Master sintering curve: a practical approach to sintering". In: *Journal of the American Ceramic Society* 79.12 (1996), pp. 3211–3217.

[76] Hermann Riedel and Bernhard Blug. “A comprehensive model for solid state sintering and its application to silicon carbide”. In: *Multiscale deformation and fracture in materials and structures*. Springer, 2000, pp. 49–70.

[77] Yu U Wang. “Computer modeling and simulation of solid-state sintering: A phase field approach”. In: *Acta materialia* 54.4 (2006), pp. 953–961.

[78] P Bross and HE Exner. “Computer simulation of sintering processes”. In: *Acta Metallurgica* 27.6 (1979), pp. 1013–1020.

[79] Huilong Zhu. “Sintering processes of two nanoparticles: a study by molecular dynamics simulations”. In: *Philosophical Magazine Letters* 73.1 (1996), pp. 27–33.

[80] Vishal N Koparde and Peter T Cummings. “Molecular dynamics simulation of titanium dioxide nanoparticle sintering”. In: *The Journal of Physical Chemistry B* 109.51 (2005), pp. 24280–24287.

[81] JL Shi. “Solid state sintering of ceramics: pore microstructure models, densification equations and applications”. In: *Journal of materials science* 34.15 (1999), pp. 3801–3812.

[82] HN Ch?ng and Jingzhe Pan. “Modelling microstructural evolution of porous polycrystalline materials and a numerical study of anisotropic sintering”. In: *Journal of computational physics* 204.2 (2005), pp. 430–461.

[83] Jingzhe Pan, HN Ch?ng, and ACF Cocks. “Sintering kinetics of large pores”. In: *Mechanics of materials* 37.6 (2005), pp. 705–721.

[84] HN Ch’ng and Jingzhe Pan. “Cubic spline elements for modelling microstructural evolution of materials controlled by solid-state diffusion and grain-boundary migration”. In: *Journal of Computational Physics* 196.2 (2004), pp. 724–750.

[85] Yunzhi Wang et al. “Simulating microstructural evolution and electrical transport in ceramic gas sensors”. In: *Journal of the American Ceramic Society* 83.9 (2000), pp. 2219–2226.

[86] Klara Asp and John ?gren. “Phase-field simulation of sintering and related phenomena–A vacancy diffusion approach”. In: *Acta materialia* 54.5 (2006), pp. 1241–1248.

[87] Hans-Joachim Schmid et al. "Monte Carlo simulation of aggregate morphology for simultaneous coagulation and sintering". In: *Journal of Nanoparticle Research* 6.6 (2004), pp. 613–626.

[88] M Kamal Akhtar, G Glenn Lipscomb, and Sotiris E Pratsinis. "Monte Carlo simulation of particle coagulation and sintering". In: *Aerosol Science and Technology* 21.1 (1994), pp. 83–93.

[89] Pushkar Tandon and Daniel E Rosner. "Monte Carlo simulation of particle aggregation and simultaneous restructuring". In: *Journal of Colloid and Interface Science* 213.2 (1999), pp. 273–286.

[90] Veena Tikare, Michael Braginsky, and Eugene A Olevsky. "Numerical Simulation of Solid-State Sintering: I, Sintering of Three Particles". In: *Journal of the American Ceramic Society* 86.1 (2003), pp. 49–53.

[91] Gregory N Hassold, I-Wei Chen, and David J Srolovitz. "Computer Simulation of Final-Stage Sintering: I, Model Kinetics, and Microstructure". In: *Journal of the American Ceramic Society* 73.10 (1990), pp. 2857–2864.

[92] Michael Braginsky, Veena Tikare, and Eugene Olevsky. "Numerical simulation of solid state sintering". In: *International journal of solids and structures* 42.2 (2005), pp. 621–636.

[93] Rasmus Bjørk et al. "The effect of particle size distributions on the microstructural evolution during sintering". In: *Journal of the American Ceramic Society* 96.1 (2013), pp. 103–110.

[94] Veena Tikare et al. "Numerical simulation of microstructural evolution during sintering at the mesoscale in a 3D powder compact". In: *Computational Materials Science* 48.2 (2010), pp. 317–325.

[95] S Bordere. "The impact of fluctuations on the sintering kinetics of two particles demonstrated through Monte Carlo simulation". In: *Scripta materialia* 55.10 (2006), pp. 879–882.

[96] Yanxiang Zhang, Changrong Xia, and Meng Ni. "Simulation of sintering kinetics and microstructure evolution of composite solid oxide fuel cells electrodes". In: *International journal of hydrogen energy* 37.4 (2012), pp. 3392–3402.

[97] Michael Reed Teague. "Image analysis via the general theory of moments". In: *JOSA* 70.8 (1980), pp. 920–930.

[98] Faouzi Ghorbel et al. “Reconstructing with geometric moments”. In: *Proc. Int. Conf. on Machine Intelligence: ACIDCA-ICMI*. Citeseer. 2005, pp. 5–7.

[99] Lutgard C De Jonghe and Mohamed N Rahaman. “Sintering stress of homogeneous and heterogeneous powder compacts”. In: *Acta Metallurgica* 36.1 (1988), pp. 223–229.

[100] Fumihiro Wakai and Yutaka Shinoda. “Anisotropic sintering stress for sintering of particles arranged in orthotropic symmetry”. In: *Acta Materialia* 57.13 (2009), pp. 3955–3964.

[101] F Wakai, Y Shinoda, and T Akatsu. “Methods to calculate sintering stress of porous materials in equilibrium”. In: *Acta materialia* 52.19 (2004), pp. 5621–5631.

[102] HE Exner and P Bross. “Material transport rate and stress distribution during grain boundary diffusion driven by surface tension”. In: *Acta Metallurgica* 27.6 (1979), pp. 1007–1012.

[103] Arthur F Voter. “Introduction to the kinetic Monte Carlo method”. In: *Radiation effects in solids*. Springer, 2007, pp. 1–23.

[104] Nicholas Metropolis et al. “Equation of state calculations by fast computing machines”. In: *The journal of chemical physics* 21.6 (1953), pp. 1087–1092.

[105] William E Frazier. “Metal additive manufacturing: a review”. In: *Journal of Materials Engineering and Performance* 23.6 (2014), pp. 1917–1928.

[106] Sanjay Kumar. “Selective laser sintering: a qualitative and objective approach”. In: *Jom* 55.10 (2003), pp. 43–47.

[107] Lore Thijs et al. “A study of the microstructural evolution during selective laser melting of Ti–6Al–4V”. In: *Acta materialia* 58.9 (2010), pp. 3303–3312.

[108] Chunxiang Cui et al. “Titanium alloy production technology, market prospects and industry development”. In: *Materials & Design* 32.3 (2011), pp. 1684–1691.

[109] Daniel Shiffman. *The Nature of Code: Simulating Natural Systems with Processing*. Daniel Shiffman, 2012.

[110] Dierk Raabe. “Cellular automata in materials science with particular reference to recrystallization simulation”. In: *Annual review of materials research* 32.1 (2002), pp. 53–76.

[111] Dierk Raabe and Luc Hantcherli. "2D cellular automaton simulation of the recrystallization texture of an IF sheet steel under consideration of Zener pinning". In: *Computational Materials Science* 34.4 (2005), pp. 299–313.

[112] Nima Yazdipour, Christopher HJ Davies, and Peter D Hodgson. "Microstructural modeling of dynamic recrystallization using irregular cellular automata". In: *Computational Materials Science* 44.2 (2008), pp. 566–576.

[113] G Kugler and R Turk. "Study of the influence of initial microstructure topology on the kinetics of static recrystallization using a cellular automata model". In: *Computational materials science* 37.3 (2006), pp. 284–291.

[114] Chengwu Zheng et al. "Microstructure prediction of the austenite recrystallization during multi-pass steel strip hot rolling: A cellular automaton modeling". In: *Computational Materials Science* 44.2 (2008), pp. 507–514.

[115] Chengwu Zheng and Dierk Raabe. "Interaction between recrystallization and phase transformation during intercritical annealing in a cold-rolled dual-phase steel: A cellular automaton model". In: *Acta Materialia* 61.14 (2013), pp. 5504–5517.

[116] Frederik Verhaeghe et al. "A pragmatic model for selective laser melting with evaporation". In: *Acta Materialia* 57.20 (2009), pp. 6006–6012.

[117] P Fischer et al. "Sintering of commercially pure titanium powder with a Nd: YAG laser source". In: *Acta Materialia* 51.6 (2003), pp. 1651–1662.

[118] Ibiye Aseibichin Roberts et al. "A three-dimensional finite element analysis of the temperature field during laser melting of metal powders in additive layer manufacturing". In: *International Journal of Machine Tools and Manufacture* 49.12-13 (2009), pp. 916–923.

[119] Kenneth C Mills. *Recommended values of thermophysical properties for selected commercial alloys*. Woodhead Publishing, 2002.

[120] Christoph Leyens and Manfred Peters. *Titanium and titanium alloys: fundamentals and applications*. John Wiley & Sons, 2003.

[121] Nicole Stanford and PS Bate. "Crystallographic variant selection in Ti–6Al–4V". In: *Acta materialia* 52.17 (2004), pp. 5215–5224.

[122] ATW Kempen, F Sommer, and EJ Mittemeijer. "Determination and interpretation of isothermal and non-isothermal transformation kinetics; the effective

activation energies in terms of nucleation and growth". In: *Journal of materials science* 37.7 (2002), pp. 1321–1332.

[123] S Malinov et al. "Differential scanning calorimetry study and computer modeling of β? α phase transformation in a Ti-6Al-4V alloy". In: *Metallurgical and Materials Transactions A* 32.4 (2001), pp. 879–887.

[124] Wei Sha and Savko Malinov. *Titanium alloys: modelling of microstructure, properties and applications*. Elsevier, 2009.

[125] Shaohua Chen, Yaopengxiao Xu, and Yang Jiao. "Modeling morphology evolution and densification during solid-state sintering via kinetic Monte Carlo simulation". In: *Modelling and Simulation in Materials Science and Engineering* 24.8 (2016), p. 085003.

[126] Shaohua Chen, Yaopengxiao Xu, and Yang Jiao. "Modeling solid-state sintering with externally applied pressure&58; a geometric force approach". In: *AIMS Materials Science* 4.1 (2017), pp. 75–88.

[127] Bin Li and James H-C Wang. "Fibroblasts and myofibroblasts in wound healing: force generation and measurement". In: *Journal of tissue viability* 20.4 (2011), pp. 108–120.

[128] Maria L Lombardi et al. "Traction force microscopy in Dictyostelium reveals distinct roles for myosin II motor and actin-crosslinking activity in polarized cell movement". In: *Journal of cell science* 120.9 (2007), pp. 1624–1634.

[129] Risat A Jannat, Micah Dembo, and Daniel A Hammer. "Traction forces of neutrophils migrating on compliant substrates". In: *Biophysical journal* 101.3 (2011), pp. 575–584.

[130] Amani A Alobaidi et al. "Probing cooperative force generation in collective cancer invasion". In: *Physical biology* 14.4 (2017), p. 045005.

[131] Keenan T Bashour et al. "CD28 and CD3 have complementary roles in T-cell traction forces". In: *Proceedings of the National Academy of Sciences* 111.6 (2014), pp. 2241–2246.

[132] Matthew J Paszek et al. "Tensional homeostasis and the malignant phenotype". In: *Cancer cell* 8.3 (2005), pp. 241–254.

[133] H Delanoë-Ayari, JP Rieu, and M Sano. "4D traction force microscopy reveals asymmetric cortical forces in migrating Dictyostelium cells". In: *Physical Review Letters* 105.24 (2010), p. 248103.

[134] Renaud Poincloux et al. "Contractility of the cell rear drives invasion of breast tumor cells in 3D Matrigel". In: *Proceedings of the National Academy of Sciences* 108.5 (2011), pp. 1943–1948.

[135] Christine E Schmidt et al. "Integrin-cytoskeletal interactions in migrating fibroblasts are dynamic, asymmetric, and regulated." In: *The Journal of Cell Biology* 123.4 (1993), pp. 977–991.

[136] Dennis E Discher, Paul Janmey, and Yu-li Wang. "Tissue cells feel and respond to the stiffness of their substrate". In: *Science* 310.5751 (2005), pp. 1139–1143.

[137] Léa Trichet et al. "Evidence of a large-scale mechanosensing mechanism for cellular adaptation to substrate stiffness". In: *Proceedings of the National Academy of Sciences* 109.18 (2012), pp. 6933–6938.

[138] Albert K Harris, Patricia Wild, and David Stopak. "Silicone rubber substrata: a new wrinkle in the study of cell locomotion". In: *Science* 208.4440 (1980), pp. 177–179.

[139] Micah Dembo and Yu-Li Wang. "Stresses at the cell-to-substrate interface during locomotion of fibroblasts". In: *Biophysical journal* 76.4 (1999), pp. 2307–2316.

[140] Farzan Beroz et al. "Physical limits to biomechanical sensing in disordered fibre networks". In: *Nature communications* 8 (2017), p. 16096.

[141] Andrew D Doyle et al. "Local 3D matrix microenvironment regulates cell migration through spatiotemporal dynamics of contractility-dependent adhesions". In: *Nature communications* 6 (2015), p. 8720.

[142] Catherine G Galbraith and Michael P Sheetz. "A micromachined device provides a new bend on fibroblast traction forces". In: *Proceedings of the National Academy of Sciences* 94.17 (1997), pp. 9114–9118.

[143] John L Tan et al. "Cells lying on a bed of microneedles: an approach to isolate mechanical force". In: *Proceedings of the National Academy of Sciences* 100.4 (2003), pp. 1484–1489.

[144] Olivia Du Roure et al. "Force mapping in epithelial cell migration". In: *Proceedings of the National Academy of Sciences of the United States of America* 102.7 (2005), pp. 2390–2395.

[145] Stacey A Maskarinec et al. "Quantifying cellular traction forces in three dimensions". In: *Proceedings of the National Academy of Sciences* 106.52 (2009), pp. 22108–22113.

[146] Wesley R Legant et al. "Multidimensional traction force microscopy reveals out-of-plane rotational moments about focal adhesions". In: *Proceedings of the National Academy of Sciences* 110.3 (2013), pp. 881–886.

[147] Brendon M Baker and Christopher S Chen. "Deconstructing the third dimension–how 3D culture microenvironments alter cellular cues". In: *J Cell Sci* 125.13 (2012), pp. 3015–3024.

[148] Wesley R Legant et al. "Measurement of mechanical tractions exerted by cells in three-dimensional matrices". In: *Nature methods* 7.12 (2010), p. 969.

[149] Jacob Notbohm et al. "Quantifying cell-induced matrix deformation in three dimensions based on imaging matrix fibers". In: *Integrative Biology* 7.10 (2015), pp. 1186–1195.

[150] Julian Steinwachs et al. "Three-dimensional force microscopy of cells in biopolymer networks". In: *Nature methods* 13.2 (2016), p. 171.

[151] Jihan Kim et al. "Three-dimensional reflectance traction microscopy". In: *PloS one* 11.6 (2016), e0156797.

[152] Pierre Ronceray, Chase P Broedersz, and Martin Lenz. "Fiber networks amplify active stress". In: *Proceedings of the national academy of sciences* 113.11 (2016), pp. 2827–2832.

[153] Christopher Allen Rucksack Jones et al. "The spatial-temporal characteristics of type I collagen-based extracellular matrix". In: *Soft Matter* 10.44 (2014), pp. 8855–8863.

[154] Yang Jiao and Salvatore Torquato. "Quantitative characterization of the microstructure and transport properties of biopolymer networks". In: *Physical biology* 9.3 (2012), p. 036009.

[155] Ya-li Yang and Laura J Kaufman. "Rheology and confocal reflectance microscopy as probes of mechanical properties and structure during collagen

and collagen/hyaluronan self-assembly". In: *Biophysical journal* 96.4 (2009), pp. 1566–1585.

[156] Ya-li Yang, Lindsay M Leone, and Laura J Kaufman. "Elastic moduli of collagen gels can be predicted from two-dimensional confocal microscopy". In: *Biophysical journal* 97.7 (2009), pp. 2051–2060.

[157] Christopher AR Jones et al. "Micromechanics of cellularized biopolymer networks". In: *Proceedings of the National Academy of Sciences* 112.37 (2015), E5117–E5122.

[158] Long Liang et al. "Heterogeneous force network in 3D cellularized collagen networks". In: *Physical biology* 13.6 (2016), p. 066001.

[159] Jihan Kim et al. "Stress-induced plasticity of dynamic collagen networks". In: *Nature communications* 8.1 (2017), p. 842.

[160] Brian Burkel and Jacob Notbohm. "Mechanical response of collagen networks to nonuniform microscale loads". In: *Soft matter* 13.34 (2017), pp. 5749–5758.

[161] Peter Grimmer and Jacob Notbohm. "Displacement propagation in fibrous networks due to local contraction". In: *Journal of biomechanical engineering* 140.4 (2018), p. 041011.

[162] Marvin M Doyley and Kevin J Parker. "Elastography: general principles and clincial applications". In: *Ultrasound clinics* 9.1 (2014), p. 1.

[163] MM Doyley. "Model-based elastography: a survey of approaches to the inverse elasticity problem". In: *Physics in Medicine & Biology* 57.3 (2012), R35.

[164] MM Doyley, PM Meaney, and JC Bamber. "Evaluation of an iterative reconstruction method for quantitative elastography". In: *Physics in Medicine & Biology* 45.6 (2000), p. 1521.

[165] AR Skovoroda, SY Emelianov, and M O'donnell. "Tissue elasticity reconstruction based on ultrasonic displacement and strain images". In: *IEEE transactions on ultrasonics, ferroelectrics, and frequency control* 42.4 (1995), pp. 747–765.

[166] Adeline Bouvier et al. "A direct vulnerable atherosclerotic plaque elasticity reconstruction method based on an original material-finite element formulation: theoretical framework". In: *Physics in Medicine & Biology* 58.23 (2013), p. 8457.

[167] Hendrik HG Hansen et al. "Noninvasive vascular displacement estimation for relative elastic modulus reconstruction in transversal imaging planes". In: *Sensors* 13.3 (2013), pp. 3341–3357.

[168] Radj A Baldewsing et al. "Young?s modulus reconstruction of vulnerable atherosclerotic plaque components using deformable curves". In: *Ultrasound in Medicine and Biology* 32.2 (2006), pp. 201–210.

[169] Habib Ammari, Jin Keun Seo, and Liangdong Zhou. "Viscoelastic modulus reconstruction using time harmonic vibrations". In: *Mathematical Modelling and Analysis* 20.6 (2015), pp. 836–851.

[170] Eunyoung Park and Antoinette M Maniatty. "Shear modulus reconstruction in dynamic elastography: time harmonic case". In: *Physics in Medicine & Biology* 51.15 (2006), p. 3697.

[171] Jonathan Ophir et al. "Elastography: a quantitative method for imaging the elasticity of biological tissues". In: *Ultrasonic imaging* 13.2 (1991), pp. 111–134.

[172] Yanning Zhu, Timothy J Hall, and Jingfeng Jiang. "A finite-element approach for Young's modulus reconstruction". In: *IEEE transactions on medical imaging* 22.7 (2003), pp. 890–901.

[173] Faouzi Kallel and Michel Bertrand. "Tissue elasticity reconstruction using linear perturbation method". In: *IEEE Transactions on Medical Imaging* 15.3 (1996), pp. 299–313.

[174] KR Raghavan and Andrew E Yagle. "Forward and inverse problems in elasticity imaging of soft tissues". In: *IEEE Transactions on nuclear science* 41.4 (1994), pp. 1639–1648.

[175] Anthony J Romano, Joseph J Shirron, and Joseph A Bucaro. "On the non-invasive determination of material parameters from a knowledge of elastic displacements theory and numerical simulation". In: *IEEE transactions on ultrasonics, ferroelectrics, and frequency control* 45.3 (1998), pp. 751–759.

[176] Mohit Tyagi et al. "Algorithms for quantitative quasi-static elasticity imaging using force data". In: *International journal for numerical methods in biomedical engineering* 30.12 (2014), pp. 1421–1436.

[177] Paul E Barbone and Jeffrey C Bamber. "Quantitative elasticity imaging: what can and cannot be inferred from strain images". In: *Physics in Medicine & Biology* 47.12 (2002), p. 2147.

[178] Xiaochang Pan et al. “A regularization-free elasticity reconstruction method for ultrasound elastography with freehand scan”. In: *Biomedical engineering online* 13.1 (2014), p. 132.

[179] Faouzi Kallel et al. “Elastographic imaging of low-contrast elastic modulus distributions in tissue”. In: *Ultrasound in Medicine and Biology* 24.3 (1998), pp. 409–425.

[180] S Yoneyama. “Smoothing measured displacements and computing strains utilising finite element method”. In: *Strain* 47.s2 (2011), pp. 258–266.

[181] Jacob Fish and Ted Belytschko. “A first course in finite elements”. In: (2007).

[182] Jorge J Moré and Danny C Sorensen. “Computing a trust region step”. In: *SIAM Journal on Scientific and Statistical Computing* 4.3 (1983), pp. 553–572.

[183] Thomas F Coleman and Yuying Li. “A reflective Newton method for minimizing a quadratic function subject to bounds on some of the variables”. In: *SIAM Journal on Optimization* 6.4 (1996), pp. 1040–1058.

[184] Yu Long Han et al. “Cell contraction induces long-ranged stress stiffening in the extracellular matrix”. In: *arXiv preprint arXiv:1709.00793* (2017).

APPENDIX A

MODIFICATIONS IN MFIX-DEM FOR POLYDISPERSITY IMPLEMENTATION

We now describe our implementation for polydispersity. In the recent *2016-1* release version of MFIX-DEM, each distinct solid phase is only allowed to possess a unique particle size, which is saved in the array **D_P0**, whose size is the number of solid phases in the system. Each solid particle is assigned a unique phase index based on its diameter, based on which the phase-specific physical properties of the particles (e.g., material density, Young's modulus, coefficient of friction, coefficient of restitution, etc.) can be retrieved and employed in the subsequent computation of particle contact forces.

As has been discussed, our implementation of poly-dispersity allows the users to specify the particle size distribution for both the initial condition (IC) and mass-inflow boundary conditions (MIC). This is achieved by introducing two sets of new key words, respectively, for ICs and MICs, which are summarized below:

- *DISCRETELEMENT_MOD.F* is modified to add five global arrays that specify the particle size distributions for different solid phases, including **DISTRI_TYPE**(Phase) (type of the distribution), **DISTRI_MEAN**(Phase) (mean of the distribution), **DISTRI_STANDARD_DEVIATION**(Phase) (standard deviation of the distribution), (DISTRI_LOWER_BOUND)(Phase) (smallest cut-off diameter), **DISTRI_UPPER_BOUND**(Phase) (largest cut-off diameter). The size of the arrays is the total number of solid phases in the system. And the cut-off values are required to truncate the continuous distribution function for efficient numerical simulation.
- *GENERATE_PARTICLES_MOD.F* is modified to generate particles with the diameter according to the specified particle size distribution (i.e., the distribution parameters in *DISCREMENT_MOD.F*), instead of assigning particles with the same phase with the same diameter for that phase.
- *SET_PHASE_INDEX.F* is modified to assign a unique phase index to each particle according to the associated physical properties, e.g., material density, instead of basing on particle size.

Newly introduced key words:

1. **IC_PSD_TYPE**(ICV, Phase): The type of particle size distribution function (e.g., normal, log-normal, uniform or user-specified) in region ICV in the initial configuration for solid phase-m.
2. **IC_PSD_MEAN_DP**(ICV, Phase): The mean of the particle size distribution function (i.e., the mean particle size) in region ICV in the initial configuration for solid phase-m.
3. **IC_PSD_STDEV**(ICV, Phase): The standard deviation of the particle size distribution function in region ICV in the initial configuration for solid phase-m.
4. **IC_PSD_MAX_DP**(ICV, Phase): The largest cut-off diameter for particles of solid phase-m in region ICV in the initial configuration.

5. **IC_PSD_MAX_DP**(ICV, Phase): The largest cut-off diameter for particles of solid phase-m in region ICV in the initial configuration. The new key words for the mass-in-flow boundary conditions are summarized below:
6. **BC_PSD_TYPE**(BCV, Phase): The type of particle size distribution function (e.g., normal, log-normal, uniform or user-specified) in boundary region BCV for the mass-in-flow boundary condition for solid phase-m.
7. **BC_PSD_MEAN_DP**(BCV, Phase): The mean of the particle size distribution function (i.e., the mean particle size) in boundary region BCV for the mass-in-flow boundary condition for solid phase-m.
8. **BC_PSD_STDEV**(BCV, Phase): The standard deviation of the particle size distribution function in boundary region BCV for the mass-in-flow boundary condition for solid phase-m.
9. **BC_PSD_MAX_DP**(BCV, Phase): The largest cut-off diameter for particles of solid phase-m in boundary region BCV for the mass-in-flow boundary condition.
10. **BC_PSD_MAX_DP**(BCV, Phase): The largest cut-off diameter for particles of solid phase-m in boundary region BCV for the mass-in-flow boundary condition. Again, we note that the cut-off values (upper and lower bounds) for particle diameter are required to truncate the continuous distribution function for efficient numerical simulation.